THE UNIVERSITY OF CHICAGO

COMPUTATIONAL PREDICTIONS OF THE THERMAL CONDUCTIVITY OF
SOLIDS AND LIQUIDS

A DISSERTATION SUBMITTED TO
THE FACULTY OF THE PRITZKER SCHOOL OF MOLECULAR ENGINEERING
IN CANDIDACY FOR THE DEGREE OF
DOCTOR OF PHILOSOPHY

BY
MARCELLO PULIGHEDDU

CHICAGO, ILLINOIS
AUGUST 2020

TABLE OF CONTENTS

LIST OF FIGURES

v

viii

LIST OF TABLES

ACKNOWLEDGMENTS

CHAPTER 1

INTRODUCTION

The study of thermal transport in materials is of interest to a variety of disciplines, including material science, aerospace engineering, geoscience, physics and chemistry[3–5]. Indeed, thermal performance is an important metric for batteries[6], thermoelectric materials[7–9], solar and photoelectrochemical cells[10–12], thermal barrier coatings in turbines[13], safe storage of nuclear fuels and microelectronics devices[14].

The thermal conductivity is a transport coefficient related to the ability of a material to transport heat in the presence of a temperature gradient. Some applications require materials with low thermal conductivity. For example in the case of thermoelectric materials, in order to maximize their figure of merit it is desirable to achieve low thermal conductivity and high electrical conductivity and a high Seebeck coefficient at the same time[15–17]. A thermoelectric material is used to convert a temperature gradient into an electric potential, thus directly converting a temperature difference to electrical power. A promising path explored in the literature to design materials with the desired, low thermal conductivity is the creation of nanostructured systems.

Some technological applications benefit instead from materials with a large thermal conductivity, for example the cooling of electronic devices[18,19]. Thermal transport plays a crucial role in the performance and reliability of semiconductor electronic devices. A large share of all integrated circuit failures is related to thermal issues. The continuing decrease in the characteristic lengths of the structures of electronic devices and the ever more aggressive thermal conditions imposed upon them requires sophisticated understanding and control of thermal transport at the nanoscale. The ever increasing miniaturization of electronic devices has led to mean-free paths of heat carriers approaching few nanometers. Additionally, the high density of interfaces impedes thermal transport and contributes significantly to the

overall thermal resistance. Highly localized power densities, associated to large bottlenecks to heat transport, ultimately dictate device operating frequencies, functionality, reliability, and failure thresholds.

To improve our fundamental understanding of thermal transport and in general materials design, the accurate prediction of thermal transport coefficients is critical[20,21]. Thermal transport may have conduction, convection and radiation components. Conduction is the transport of energy due to atomic and electronic motion across a temperature gradient, and in solids it can be described by measuring the thermal conductivity of the system, namely the ratio between the heat current and the temperature gradient. Convection is the heat transfer due to the motion of particles inside a fluid, a liquid or gas. Convection is absent in solids, due the absence of diffusion. Radiation is the transport of heat from the surface of a material by photons. In this thesis we focus on thermal transport by conduction, and in particular on the calculation of the thermal conductivity.

To date, most calculations of the thermal conductivity at the atomistic level, especially those requiring the use of large samples, have been carried out using empirical interatomic potentials (EIP), that are available only for some classes of materials and often have limited predictive power. Only recently accurate ab initio predictions of the thermal conductivity of simple crystals and fluids have been made possible due to advances in theory and increase in computational power[22]. Nonetheless, these ab initio calculations are still limited to systems with tens of atoms, at most several hundreds.

Neural networks (NN) trained on ab initio data[23] offer a promising avenue to bridge the gap between empirical potentials and straightforward ab initio simulations, and may allow for the calculation of the thermal conductivity of complex materials with the accuracy of first principle calculations.

On the experimental side, progress has been made in the measurement of the thermal conductivity thank to the development of the 3ω method[24], and of time or frequency domain thermo-reflectance (TDTR and FDTR) methods[25,26].

In this thesis we discuss methods to compute the thermal conductivity of solids and liquids and in particular we present an approach developed to address the need for an efficient and general quantum simulation framework for thermal properties of materials[27,28]. The method developed here can be used to efficiently compute the thermal conductivity using either classical, first principle or neural-network molecular dynamics (MD), and using only atomic trajectories and forces as input. We show applications of the approach to the calculations of the thermal conductivity of crystalline and nanocrystalline MgO and liquid water. We used first principles simulations and deep MD for MgO and water, respectively, and empirical potentials for large samples of nanocrystalline MgO. In addition, we compared MD based approaches to compute thermal conductivity of solids with techniques based on the Boltzmann Transport Equation.

The thesis is organized as follows: in chapter 2 we define the thermal conductivity and describe two of the methods commonly used for its computation. In chapter 3 we present a detailed comparison of the two methods. In chapter 4 we report our study of thermal transport in nano-porous silicon, highlighting the role of nanostructuring and morphology on the thermal conductivity of the system. In chapter 5 we describe a method for the efficient calculation of the thermal conductivity of solid and fluids that only requires atomic trajectories and forces as input. In chapter 6 and 7 we show the application of this approach to the thermal conductivity of crystalline and nanostructured MgO, including *ab initio* results, and of liquid water, including our neural-network based calculations.

Parts of Chapter 3, 5, 6 and 7 were adapted from the following papers:

- Computational prediction of lattice thermal conductivity: A comparison of molecular

dynamics and Boltzmann transport approaches. M. Puligheddu, Y. Xia, M. Chan, G. Galli Physical Review Materials 3, 085401

- First-principles simulations of heat transport. M. Puligheddu, F. Gygi, G. Galli Physical Review Materials 1 (6), 060802

- Atomistic simulations of the thermal conductivity of liquids. M. Puligheddu, G. Galli Physical Review Materials 4 (5), 053801

CHAPTER 2

THEORETICAL BACKGROUND ON THE CALCULATION OF THE THERMAL CONDUCTIVITY

2.1 Introduction

The thermal conductivity (κ) is the capacity of a material to transport energy in the form of heat in the presence of a temperature difference. The thermal conductivity tensor ($\kappa_{\alpha\beta}$) is defined by the Fourier Equation: $J_\alpha = -\kappa_{\alpha\beta}\nabla_\beta T$, where J_α is the heat flux in the α direction, $\nabla_\beta T$ is the gradient of the temperature in the β direction. In simpler terms, the thermal conductivity describes the ratio between the response of the system (the heat flux) and the perturbation which caused the response (the temperature gradient). The full tensor description of the thermal conductivity is only necessary in anisotropic media, in isotropic material the thermal conductivity is a scalar, measured in $W/(m\ K)$ (Watt over meter Kelvin).

The combination of two processes contributes to the thermal conductivity: heat transported by electrons and heat transported by to the motions of atoms. The first process yields the electronic thermal conductivity, it is dominant in metals and absent in insulating solid and liquids. The second process yields the so-called lattice thermal conductivity. In this thesis we only study dielectric solids and insulating liquids, where the contribution of the electronic thermal conductivity is negligible, thus unless otherwise stated, we use the term thermal conductivity to indicate the second process.

Thermal conductivity values may be very different, depending on the material and on allotropes of the same element: diamond for example has a thermal conductivity of 2200W/mK, graphite of 25 W/mK in the cross-plane direction and 470 W/mK in the in-plane directions, at ambient conditions.

A multitude of methodologies have been introduced to calculate the thermal conductivity. Of particular significance are two categories of methods, based either on considering atomic mo-

tion (Molecular Dynamics, MD) or collective vibrational excitations, i.e. phonons in solids (Anharmonic Lattice Dynamics, ALD). In this chapter we briefly describe Molecular Dynamics (MD), introduce the Green-Kubo formalism, one of the methods we used to compute the thermal conductivity using MD, and discuss anharmonic lattice dynamics, an alternative method used to compute the thermal conductivity. Finally, we discuss the relative merits and weakness of each method.

2.2 Calculation of Thermal Conductivity using Molecular Dynamics

Une intelligence qui, pour un instant donné, connaîtrait toutes les forces dont la nature est animée et la situation respective des êtres qui la composent, si d'ailleurs elle était assez vaste pour soumeitre ces données â l'Analyse, embrasserait dans la même formule les mouvements des plus grands corps de l'univers et ceux du plus léger atome: rien ne serait incertain pour elle, et l'avenir, comme le passé, serait présent â ses yeux.

An overconfident Pierre-Simon Laplace, Essai philosophiques sur les probabilités, Courcier, 1814

2.2.1 Molecular Dynamics

Molecular Dynamics (MD)[29,30] is a computational technique to obtain trajectories of a solid or a liquid obeying classical dynamics. In Fig. 2.1 we show the basic steps of a MD simulation: from given initial positions r_i of the atoms, we can compute the total force F_i acting on each atom as the negative gradient of the potential energy with respect to its position $F_i = -\nabla_{r_i} E$. From the forces we compute the accelerations $a_i = F_i/m_i$ of each atom and update the velocity v_i of the atoms. Finally, we update the positions of all atoms and restart the cycle by computing the new forces from the updated positions.

The initial positions are chosen based on the knowledge of the system, including available

experimental data and previous studies. The initial velocities may be randomly sampled from a normal distribution. They then may be rescaled so that the total momentum of the system is zero and the temperature, computed as $T = \frac{1}{3k_B N}\sum_i m_i|v_i|^2$ is equal to the desired one. In the previous equation k_B is the Boltzmann constant, N is the number of atoms and m_i is the mass of the i-th atom.

A derivation of the previous equation is available in any book about thermodynamics[31], however, we would like to note how we already made a connection between a macroscopic property (the temperature) and a microscopic one (the velocities of the atoms). The fundamental tenet of MD is that macroscopic and measurable properties of a material e.g. transport, mechanical and optical properties, can be understood and predicted, sometimes accurately, by studying the motion of its components.

Going back to the MD cycle, the update of the velocities and positions cannot be done analytically, due to the complicated dependence of the total energy on the position of the atoms. The simulation is carried out by integrating numerically the Newton equations of motion, using a discreet time interval, called the timestep (dt). The choice of timestep is an important decision in any MD simulation: a dt too large may results in unacceptable numerical errors and incorrect results, while a dt too small results in increased computational cost for no additional results; for simulations of atoms, the timestep is usually in the order of magnitude of femtoseconds (10^{-15} seconds).

A direct integration scheme:

$$\text{compute a(t) from r(t)}$$
$$r_i(t + dt) = r_i(t) + v_i(t)dt + \frac{1}{2}a_i(t)dt^2$$
$$v_i(t + dt) = v_i(t) + a_i(t)dt$$

while correct, suffers from large numerical errors for a given timestep when compared to Velocity Verlet (vV), the commonly used integration method. The vV method include a

7

predictor and a corrector stage, leading to a half-timestep update for the velocities:

$$\text{compute a(t) from r(t)}$$

$$r_i(t + dt) = r_i(t) + v_i(t)dt + \frac{1}{2}a_i(t)dt^2$$

$$v_i(t + dt/2) = v_i(t) + a_i(t)dt/2$$

$$\text{compute a(t+dt) from r(t+dt)}$$

$$v_i(t + dt) = v_i(t + dt/2) + a_i(t + dt)dt/2$$

The vV method achieves a greater accuracy than the direct method, for a negligible increase in computational cost. There are more elaborate (and costly) integration schemes, such as Runge-Kutta[32], Beeman[33], Respa[34], but they are seldom worth the trade-off. All our simulations used the velocity Verlet integrator.

2.2.2 Empirical Interatomic Potentials

The forces needed in MD to evolve the simulations are computed from the gradient of the potential energy. The potential energy is a complicated function of the position of all atoms in the system, and the evaluation of its gradient with respect to the position of each atom is the dominant computational cost in the vast majority of cases. To limit this computational cost, various choices need to be made, balancing accuracy and efficiency.

The various methods used to approximate the potential energy function range from simple *ansatz* about the shape and parameter of this function (Empirical Interatomic Potentials EIP), to complicated functions with hundreds of parameters, and finally to calculations with no empirical parameters, but explicitly solving the Schrödinger equation for the electrons and including the wavefunctions of the electrons. For a simulation with the same number of atoms, carried out for the same number of steps, the difference in computational cost between
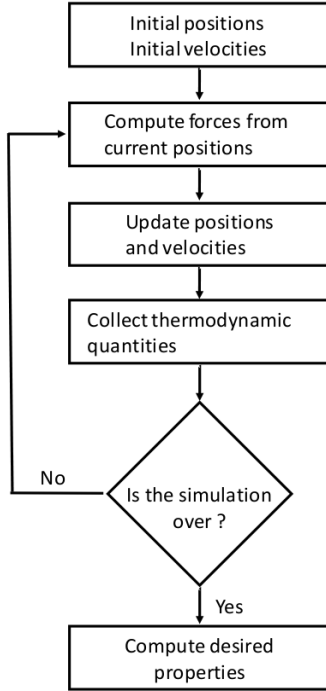
Figure 2.1: A schematic representation of the MD cycle

.

different choices for the potential energy can easily span several orders of magnitude. The increase in computational cost with respect to the number of atoms depends on the potential chosen, varying from a linear increase in the simpler cases to a cubic dependence on the number of atoms in the case of Density Functional Theory (DFT) derived forces. Needless to say, these latter simulations are less widespread and only include a limited number of atoms.

The simplest practical EIP is the Lennard-Jones (LJ) potential. This potential is very limited in the type of atoms it can simulate with any accuracy, although it is often a good approximation for noble gases. The potential energy is the sum of pairwise interactions between atoms, and the potential energy of a pair of atoms is a function of their distance, repulsive for close atoms and attractive between distant atoms:

$$E_P = \frac{1}{2} \sum_i \sum_{j \neq i} E_P(r_{ij}) = \frac{1}{2} \sum_i \sum_{j \neq i} \frac{A}{r_{ij}^{12}} - \frac{B}{r_{ij}^6} \tag{2.1}$$

9

The r^6 term represents an approximation of the van der Waals forces between neutral atoms. The short-distance repulsive r^{12} term is used to approximate the Pauli repulsion between electron shells, although its analytical dependence is not fully justified, but was instead chosen because of computational simplicity. This potential has two parameters, A and B, whose value depends on the elements one wish to simulate. More generally, the parameters for an EIP are usually obtained by adjusting their value until the results of a simulation is as close as possible to a limited set of experimental outcomes, such as a certain phase diagram, the density or some vibrational frequencies of a material. This procedure of finding the most accurate value for a given potential is called fitting, in analogy with the least-square minimization used in regression analysis for fitting a function to a set of values.

There are classes of potentials specialize for a given system. For example, in the case of water, a commonly used potential is TIP4P[35], a potential specialized for liquid water at standard conditions (300K, 1 atm). The potential is composed of two parts: a LJ term describing the repulsion between molecules and a Coulomb term describing the interaction between the partially charged O and H atoms. In the original formulation of the potential the water molecule is rigid: the relative positions of the atoms in a molecule cannot change. The LJ term is centered on the oxygen atom of each molecule, the charge terms are centered on the two hydrogen atoms and in a charge center localized roughly in the middle of the molecule. The total energy is again the sum of pairwise interaction between water molecules:

$$E_P = \frac{1}{2} \sum_i \sum_{j \neq i} \frac{A}{r_{OO}^{12}} - \frac{B}{r_{OO}^6} + \sum_a \sum_b \frac{q_a q_b}{r_{ab}} \tag{2.2}$$

where r_{OO} is the distance between the oxygen atoms and $a(b)$ indicates the charge centers in molecule i (j). The A and B parameters, the value of the charges q and the exact position of the charge center are all fitting parameters. There are several sets of parameters available for TIP4P, including one specifically made for ice simulations, and many variations in the form of the potential, for example releasing the rigidity constrain on the molecule, thus making it

10

flexible, or adding a 4th and 5th charge center to better approximate the charge distribution of the real water molecule[36].

EIP potentials are a powerful tool for computational physics. Despite their advantages, they face serious limitations. For examples, in TIP4P the charges are static parameters independent of the presence or orientation of nearby water molecules, and therefore electronic polarization effects are not included. In addition, EIP generally assume that the type of bonds among the atoms are fixed and, therefore, cannot describe chemical reactions or changes in the intramolecular bonds. Finally, EIP are usually limited in the portion of the phase diagram they can accurately simulate.

2.2.3   Ab Initio Molecular Dynamics

When more flexibility and precision is needed or an EIP cannot be built, the forces can be obtained from first principle, without any assumption regarding the form of the potential energy function nor the value of the parameters in this function. The potential energy, and the forces, can be obtained by using a quantum mechanical method, such as density functional theory[37,38]. This method is called *Ab Initio* Molecular Dynamics (AIMD) or alternatively First Principle Molecular Dynamics (FPMD).

Consider a system of N nuclei and N_e electrons. The nuclei have charge Z_I and mass M_I. The Hamiltonian is a function of the nuclear coordinates R_I and of the electronic coordinates r_i. Ignoring spin, the non-relativistic Hamiltonian is:

$$-\sum_I \frac{\nabla_{R_I}^2}{2M_I} - \sum_i \frac{\nabla_{r_i}^2}{2m_e} + \frac{1}{2}\sum_I \sum_{J\neq I} \frac{Z_I Z_J e^2}{\|R_I - R_J\|} + \frac{1}{2}\sum_i \sum_{j\neq i} \frac{e^2}{\|r_i - r_j\|} - \frac{1}{2}\sum_i \sum_I \frac{Z_I e^2}{\|r_i - r_I\|}$$

$$(2.3)$$

The many body wavefunction Ψ describing the system is given by the solution of the time-independent Schrödinger equation:

$$H\left|\Psi\right\rangle = \epsilon(R)\left|\Psi\right\rangle \tag{2.4}$$

An exact solution of this problem is not feasible, and approximations need to be made. The first one is the Born–Oppenheimer approximation: since the electrons are lighter than the nuclei by approximately three orders of magnitude, it is possible to separate the timescales of the electronic and nuclear motion. Under the Born-Oppenheimer approximation, the atomic nuclei and electrons in a molecule can be treated separately. The wavefunction is separated in an electronic and nuclear part, then the nuclei are treated classically. The electronic Hamiltonian is a function of the electronic coordinates r and depends parametrically on the position of the nuclei R. The Schrödinger equation for the electronic wavefunction $\Phi(r;R)$ reads

$$[-\sum_i \frac{\nabla_{r_i}^2}{2m_e} + \frac{1}{2}\sum_i\sum_{j\neq i}\frac{e^2}{\|r_i-r_j\|} - \frac{1}{2}\sum_i\sum_I\frac{Z_I e^2}{\|r_i-r_I\|}]\left|\Phi(r;R)\right\rangle = H_e\left|\Phi(r;R)\right\rangle = \epsilon(R)\left|\Phi(r;R)\right\rangle \tag{2.5}$$

where the energy ϵ is a function of the position of the nuclei

$$\epsilon(R) = E - \sum_I \frac{P_I}{2M_I} - \frac{1}{2}\sum_I\sum_{J\neq I}\frac{Z_I Z_J e^2}{\|R_I-R_J\|} \tag{2.6}$$

where P_I is the momentum of the I-th nucleus. Equation 2.5 is an eigenvalue problem. Its solutions are a set of wavefunctions $\Phi_n(r;R)$ and energies $\epsilon_n(R)$; Since H_e is Hermitian its eigenvalues are all real. The lowest eigenvalue is called the ground state energy, while the others describe excited states of the system. We neglect non-adiabatic effects, and only

consider the electronic ground state Φ_0 of the system:

$$[-\sum_i \frac{\nabla_{r_i}^2}{2m_e} + \frac{1}{2}\sum_i\sum_{j\neq i}\frac{e^2}{\|r_i - r_j\|} - \frac{1}{2}\sum_i\sum_I\frac{Z_Ie^2}{\|r_i - r_I\|}]\,|\Phi_0(r;R)\rangle = \epsilon_0(R)\,|\Phi_0(r;R)\rangle \quad (2.7)$$

To compute the classical trajectories of the nuclei we solve the Newton equations:

$$\dot{R}_I = V_I = \frac{P_I}{M_I} \tag{2.8}$$

$$\dot{V}_I = \frac{F_I}{M_I} = -\nabla_{R_I}E_0 \tag{2.9}$$

$$\tag{2.10}$$

where V and F are velocities and forces. The gradient of the potential energy is:

$$\nabla_{R_I}E_0 = \nabla_{R_I}\epsilon_0(R) - \nabla_{R_I}\sum_{J\neq I}\frac{Z_IZ_Je^2}{\|R_I - R_J\|} \tag{2.11}$$

The first term in the force is the gradient of the ground state eigenvalue of the electronic eigenvalue problem 2.7. Using the Hellman–Feynman theorem[39], it can be calculated as

$$\nabla_{R_I}\epsilon_0(R) = \langle\Phi_0|\,|\nabla_{R_I}H(R)|\,|\Phi_0\rangle \tag{2.12}$$

The problem described in equation 2.7 is still too complicated to be solved numerically for a practical number of atoms. The problem of finding the minimum energy ϵ_0 and its associated wavefunction Φ_0 grows exponentially with the number of electrons, seriously reducing the size of the systems that can be practically solved.

2.2.4   Density Functional Theory

Density Functional Theory (DFT) is a way to significantly reduce the computational cost of AIMD, at the cost of introducing approximations. First, let us introduce the electronic

density for the ground state:

$$n(r) = \int |\Phi(r, r_2, r_2, ..., r_{N_e})|^2 dr_2 dr_3 ... dr_{N_e} \qquad (2.13)$$

We note that while the wavefunction is a function of $3N$ variables, the density is a function of the 3 spatial variables. As proven by the Hohenberg–Kohn[37] theorems, the energy E_0, in principle a function of the full electronic wavefunction Φ, is completely determined by the electronic density, and so is the energy of the ground state. In mathematical term, the ground state energy is a functional of the electronic density:

$$E_0 = E[n_0(r)] \qquad (2.14)$$

As proved by Hohenberg and Kohn the functional E is unique and universal for a given number of electrons. Unfortunately, it is also unknown, and the HK theorems by themselves are of little practical use. A common way to transform the HK problem, and by far the most popular, is due to Kohn and Sham[40]. The fundamental ansatz leading to the Kohn-Sham (KS) equations is that the true electronic density can be written as the electronic density of as auxiliary system composed of N_e single electron wavefunctions $\phi_i(r)$. Equation 2.7 can then be rewritten in terms of the $\phi_i(r)$ and of the electronic density. Computationally, the advantage of KS equations comes from the fact that the solution of the N_e Schrödinger equations recast in term of the single electron wavefunctions is much less expensive than the solution of a single problem with the many body wavefunction Φ.

Following Kohn and Sham, the energy functional in equation 2.14 can be rewritten in a series of know terms, such as the kinetic and potential energies of the single electron wavefunctions, and an additional term called the exchange-correlation functional. The latter, like the energy functional, it is a functional of the density, it is unique and universal, and also unknown. However, it can be approximated more easily than the energy functional. The number and complexity of exchange-correlation functionals is staggering and continuously

growing[41]. In an interesting parallel with EIP, some functionals are known to describe some materials better than others, or better describe the same material in a given region of the phase diagram, or better describe some properties of a material at a given condition.

2.2.5   Neural Network Potential

An alternative approach to solving the Kohn=Sham equations at each MD step consists in using a Deep Neural Network (DNN) to compute the potential energy. This approach was only recently made practical by advances in the theory and computational tools of machine learning[42,43]. It promises to combine the best of EIP and AIMD, leading to the development of an expression for the potential energy with the accuracy and generality of AIMD at a computational cost comparable to EIP.

The field of Deep Neural Network is continuously growing, and we do not intend to provide a general or through description, limiting ourselves to its application to MD, in particular we briefly describe the flavor of deep learning (DeepMD[44]) that we used in our simulations. As in the case of EIP and AIMD, when using a DNN one computes the potential energy E, the forces F_i and the virial V from the position of the atoms. In the DeepMD method the energy is decomposed as the sum of the potential energy of each atom E_i, with:

$$E = \sum_i E_i \tag{2.15}$$

Each atomic energy E_i is a function of the position and type of the i-th atom and of its neighbors:

$$E_i = E(R_i, t_i, \{R_j\}_i, \{s_j\}_i) \tag{2.16}$$

where R_i is the position of the i-th atom, of type s_i and the curly brackets indicate the list of neighbors of the i-th atom. Two atoms are neighbors if they are closer than a cutoff distance R_c, so that $|R_i - R_j| < R_c$. The atomic potential energy E_i is symmetric with

respect to rigid translations, rotations and permutations of atoms of the same type. In DeepMD this symmetry is achieved by first subtracting the position of atom i from the positions of the neighbors, then building a local frame of reference for the shifted positions, to guarantee rotational invariance, and finally sorting the neighboring atoms first by type and then by distance. This final step guarantees permutation invariance. The final result of this transformation is a vector D_i containing information about atom i and its neighbors, which like the potential energy is invariant under rigid translations, rotations and permutations of atoms of the same type. These transformations from real space coordinates to the D vectors are not strictly necessary, but they significantly increase the performance of the model.

The atomic potential energy E_i is a function of this vector D_i. In the DeepMD framework, this function is the composition of a series of N_h transformations L connecting $N_h + 1$ layers D_i^h, with the first layer D_i^0 being the input data, and the last one $D_i^{N_h}$ being the output layer:

$$D_i^{N_h} = L_{s_i}^{N_h}(L_{s_i}^{N_h-1}(...L_{s_i}^1(D_i^0)...)), \tag{2.17}$$

where we use the superscript to indicate the depth of the layer, while the subscript $s(i)$ used for the transformations L indicates that they depend on the type $s(i)$ of the i-th atom. The transformation $L_{s_i}^h$ connecting the layers D_i^h and D_i^{h-1} is:

$$L_{s_i}^h(D_i^{h-1}) = \tanh\left(W_{s_i}^h \cdot D_i^{h-1} + b_{s_i}^h\right) \tag{2.18}$$

where L is the composition of two functions: the first one is a general linear function composed of the product with the weight matrix W followed by a sum with the bias vector b, and the second one is a non linear element-wise hyperbolic tangent, called the activation function. The final transformation $L_{s_i}^{N_h}$ constitutes an exception, where the activation function is omitted. The weight matrices $W_{s_i}^h$ and bias vectors $b_{s_i}^h$ are unknown. They are *learned* by the neural network in the training process.

The objective of the training process is to build a network capable of performing accurately

on new, unseen atomic configurations after having been trained on a learning data set. The data set consist of a large number of atomic configurations, spanning a large region of the phase diagram, and the associated total energy, forces and virial. In the case of water, the model used here and developed by Linfeng Zhang, Jiequn Han, Han Wang, Roberto Car, and Weinan E[44] was trained on ab initio simulations spanning from 0 to 2500K and from 0 to 100 GPa, thus including most of the solid and liquid phase region of water. The energy, forces and virial were calculated using DFT, with the SCAN[45] exchange-correlation functional. During the learning process, the coefficients of the weight matrices W and of the bias vectors b are iteratively evolved to minimize the loss function L, defined as the sum of the mean square errors of the DNN predictions against the known values for the same configurations:

$$L(p_\epsilon, p_f, p_v) = p_\epsilon \frac{\|\Delta E\|}{N} + p_f \frac{\|\Delta F\|}{3N} + p_v \frac{\|\Delta V\|}{9N} \tag{2.19}$$

where N is the number of atoms. The errors in the DNN predictions are large at the start and decrease during the learning process, as the DNN is trained on more and more configurations. The prefactors p_ϵ, p_f, p_v, which roughly describe the learning rate of the DNN, also decrease during the learning process.

In the simulations reported in this thesis we used all classes of potentials described in this chapter: in the case of ionic crystals, we used an EIP and, at a later stage, DFT calculations. For water, we started with TIP4P-2005/f and SPCE-f, then we used a Neural Network (DeepMD) potential, trained on DFT calculations.

2.2.6   Green-Kubo relations

Over the years, several MD-based approaches have been developed to compute the thermal conductivity of bulk crystalline and amorphous materials, nanostructures, and fluids. Using the Green-Kubo (GK) relations, based on the fluctuation-dissipation theorem, the thermal

conductivity is calculated from the fluctuations of the heat correlation function during an equilibrium MD simulation, in the NVE ensemble. The so called Green-Kubo method is built on the theory of linear response[46–49], applied to the Navier-Stokes equations for the densities of conserved extensive variables[50,51] such as energy, momentum and the number of molecules.

In what follows we provide a summary of the GK method to compute thermal conductivity; a more detailed discussion can be found in Ref.[52].

When an extensive quantity a, such as the total energy, is locally conserved, it is possible to write a continuity equation:

$$\frac{\partial a(r,t)}{\partial t} = -\nabla \cdot \vec{j}(\vec{r},t) \tag{2.20}$$

where $\vec{j}$ is the associated current density. Consider a system with a non constant temperature $T(r) = T + \Delta T(r)$, with $\Delta T(r) << T$. The probability P of the system to be in the microstate Γ is:

$$P(\Gamma) = e^{-\frac{E_0(\Gamma)+V'(\Gamma)}{k_B T}}/Z \tag{2.21}$$

where E_0 is the energy of the unperturbed system and V' the change in energy due to the perturbation $\Delta T(r)$. Let us suppose V' is such that:

$$V'(\Gamma) = -\frac{1}{T}\int \Delta T(r)e(r;\Gamma)dr + \mathcal{O}(\Delta T^2) \tag{2.22}$$

where $e(r;\Gamma)$ is an energy density such that $\int e(r;\Gamma)dr = E_0(\Gamma)$, and the $\mathcal{O}(\Delta T^2)$ symbol indicates a contribution proportional to the square of the perturbation, which is ignored. The definition of the energy density is not unique, although it must obey the constrains of extensivity and conservation of the total energy E_0. As showed in a seminal study by Marcolongo *et al.*[22] this non-uniqueness has significant consequences in the *ab initio* calculation of the thermal conductivity. The linear response of the current j^i, associated to the i-th conserved quantity can be expressed as a sum over all correlations with all currents j^l associated with conserved quantities (including j^i itself) and the gradient of the density v^l

18

of the associated perturbation V^{l} [47,49]:

$$j_{\alpha}^{i} = \frac{1}{k_B T} \sum_{l} \int_{\infty}^{t} dt' \int dr' \langle j_{\alpha}^{i}(r, \Gamma_t) j_{\beta}^{l}(r', \Gamma_{t'}) \rangle \frac{\partial}{\partial r'_{\beta}} v^{l}(r', t')$$

(2.23)

Where α and β are the cartesian directions. Limiting ourselves to the case of thermal transport, by integrating the previous equation over all space and using the Fourier law:

$$J = -\kappa \nabla T$$

(2.24)

one can recover a general expression for the thermal conductivity κ, reading:

$$\kappa_{\alpha\beta} = \frac{1}{V T^2 k_B} \int_0^{\infty} \langle J_{\alpha}(t) J_{\beta}(0) \rangle dt$$

(2.25)

where the heat flux J_{α} is:

$$J_{\alpha}(t) = \int \dot{e}(r, t) r \, dr$$

(2.26)

In MD simulations, the application of the GK relations can be separated in two problems: (1) the calculation of the integral with respect to time of the autocorrelation of $J_{\alpha}(t)$ and (2) the calculation of $J_{\alpha}(t)$ itself. The former problem requires the use of long uninterrupted simulations, much longer than the autocorrelation time of the heat current, although recent developments [53,54] promise a significant reduction in the simulation time needed. The latter problem, i.e. the calculation of the heat flux, in principle requires a definition for the energy density and of its derivatives. This is trivial in EIP, but it is significantly more complicated in AIMD. Until recently, it was indeed thought to be impossible; a derivation of the heat current in Kohn-Sham DFT can be found in [22].

In Classical Molecular Dynamics, the heat flux in equation 2.26 can be rewritten as:

$$J_\alpha(t) = \int \dot{e}(r,t)r \ dr \tag{2.27}$$

$$= \int \Big[\sum_m \Big(\frac{\partial e(r,t)}{\partial R_m} \cdot V_m + \frac{\partial e(r,t)}{\partial P_m} \cdot F_m \Big) \Big] r \ dr \tag{2.28}$$

where R_m, V_m, P_m, F_m are respectively the position, velocity, momentum, and force of the atom n. In the case of classical EIPs the energy density can be separated into atomic contributions:

$$e(r,t) = \sum_n \delta(r - R_n)e_n(t) \tag{2.29}$$

$$e_n(t) = \frac{P_n^2}{2M_n} + v_n(\{R\}) \tag{2.30}$$

where we used δ for the Dirac delta function and the curly brackets $\{R\}$ indicate the set of all atomic positions. The total potential energy is partitioned into single atom atomic energies $v_n(\{R\})$. By substituting equation 2.30 in equation 2.26 the heat flux can also be decomposed into single atom contributions:

$$J(t) = \int \sum_m \frac{\partial \sum_n \delta(r - R_n)(\frac{P_n^2}{2M_n} + v_n(\{R\}))}{\partial R_m} \cdot V_m +$$

$$\frac{\partial \sum_n \delta(r - R_n)(\frac{P_n^2}{2M_n} + v_n(\{R\}))}{\partial P_m} \cdot F_m \ dr$$

$$= \sum_n e_n V_n + R_n(V_n \cdot F_n) + R_n \sum_m (\frac{\partial v_n}{\partial R_m} \cdot V_m)$$

In the case of a two body potential, where the potential energy is the sum of pairwise contributions between pairs of atoms, the energy can be decomposed by assigning to each atom in a pair half of the potential energy. A similar, but more complicated, partition can

be made for potentials which also include contributions from triplets of atoms (three body potentials) and for general many body potentials[55].

2.3 Anharmonic Lattice Dynamics and Boltzmann Transport Equation

2.3.1 Boltzmann Transport Equation

The Boltzmann transport equation (BTE) can be used to describe the time evolution of the positions and momenta of a system of (quasi)-particles, e.g. phonons. According to the BTE, at equilibrium the evolution of the occupation probability n_λ of a specific phonon mode λ due to diffusion, scattering, and the presence of an external heat current must balance:

$$\frac{\partial n_\lambda}{\partial t}(\mathbf{r}) = \frac{\partial n_\lambda}{\partial t}(\mathbf{r})_{\text{diff}} + \frac{\partial n_\lambda}{\partial t}(\mathbf{r})_{\text{scatt}} + \frac{\partial n_\lambda}{\partial t}(\mathbf{r})_{\text{ext}} = 0. \tag{2.31}$$

Under the relaxation time approximation (RTA), the scattering term can be expressed as

$$-\frac{\partial n_\lambda}{\partial t}(\mathbf{r})_{\text{scatt}} = \frac{n_\lambda - n_\lambda^0}{\tau_\lambda}, \tag{2.32}$$

where n_λ^0 and τ_λ denote the equilibrium occupation probability and relaxation time, respectively. Under an external temperature gradient ΔT, the deviation of the occupation number from its equilibrium value λ is given by

$$n_\lambda - n_\lambda^0 = \mathbf{v}_\lambda \frac{\partial n_\lambda}{\partial T} \nabla T \tau_\lambda, \tag{2.33}$$

where $\mathbf{v}_\lambda$ is the phonon group velocity vector. In the linear regime, the lattice thermal conductivity tensor is defined by

$$J^\alpha = -\sum_\beta \kappa_l^{\alpha\beta} (\nabla T)^\beta, \tag{2.34}$$

where J^α is the heat current along α direction and can be obtained as

$$J^\alpha = \sum_\lambda \int n_\lambda \hbar \omega_\lambda \mathbf{v}_\lambda^\alpha \frac{d\mathbf{k}}{(2\pi)^3}, \tag{2.35}$$

where $\mathbf{k}$ denotes the phonon wave vector. The resulting lattice thermal conductivity tensor within the RTA is

$$\kappa_l^{\alpha\beta} = \frac{1}{NVk_\mathrm{B}T^2} \sum_\lambda n_\lambda^0 (n_\lambda^0 + 1)(\hbar\omega_\lambda)^2 v_\lambda^\alpha v_\lambda^\beta \tau_\lambda, \tag{2.36}$$

where k_B is the Boltzmann constant, V is the volume of unit cell, N is the total number of phonon wave vectors included in the summation, ω_λ and v_λ are the frequency and group velocity of phonon mode λ, with Cartesian coordinates indexed by α and β. Typically, ω_λ and v_λ are extracted from phonon dispersion relations in the harmonic approximation, assuming small atomic displacements, by computing second-derivatives of the potential energy with respect to atomic displacements. Within the framework of anharmonic lattice dynamics, τ_λ is assumed to arise primarily from intrinsic phonon-phonon scattering events[56], with the lowest-order contribution being three-phonon processes.

Anharmonic Lattice Dynamics
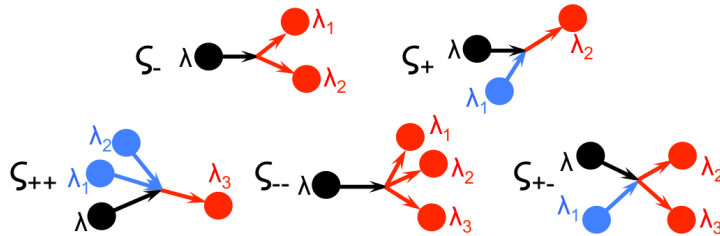
Figure 2.2: A schematic representation of three-phonon processes: (top) the splitting process ($\zeta_- : \lambda \to \lambda_1 + \lambda_2$) and the combination process ($\zeta_+ : \lambda + \lambda_1 \to \lambda_2$); and (bottom) four-phonon processes: combination ($\zeta_{++} : \lambda + \lambda_1 + \lambda_2 \to \lambda_3$), redistribution ($\zeta_{+-}\lambda + \lambda_1 \to \lambda_2 + \lambda_3$), and splitting ($\zeta_{--} : \lambda \to \lambda_1 + \lambda_2 + \lambda_3$).

.

Recently, Feng and Ruan[57–59] performed rigorous calculations of four-phonon scattering rates in the Anharmonic Lattice Dynamics (ALD-BTE) framework including fourth order Interatomic Force Constants (IFC) by extending the derivation of Maradudin *et al.*[60]. Their studies reveal that even for diamond, silicon, and germanium, which are generally considered low-anharmonicity materials, the contribution of four-phonon scattering rates is comparable to that of three-phonon scattering rates near/above the Debye temperature. Following their derivation based on Fermi's golden rule (FGR)[57], the scattering rates ($\tau_{3,\lambda}^{-1}$ and $\tau_{4,\lambda}^{-1}$) associated with three- and four-phonon processes (see Fig. 2.2) in the single mode relaxation time approximation (SMRTA) are given by

$$\tau_{3,\lambda}^{-1} = \sum_{\lambda_1 \lambda_2} \left\{ \frac{1}{2} \left(1 + n_{\lambda_1}^0 + n_{\lambda_2}^0 \right) \zeta_- + \left(n_{\lambda_1}^0 - n_{\lambda_2}^0 \right) \zeta_+ \right\}, \qquad (2.37)$$

$$\tau_{4,\lambda}^{-1} = \sum_{\lambda_1 \lambda_2 \lambda_3} \left\{ \frac{1}{6} \frac{n_{\lambda_1}^0 n_{\lambda_2}^0 n_{\lambda_3}^0}{n_\lambda^0} \zeta_{--} + \frac{1}{2} \frac{\left(1 + n_{\lambda_1}^0 \right) n_{\lambda_2}^0 n_{\lambda_3}^0}{n_\lambda^0} \zeta_{+-} + \frac{1}{2} \frac{\left(1 + n_{\lambda_1}^0 \right) \left(1 + n_{\lambda_2}^0 \right) n_{\lambda_3}^0}{n_\lambda^0} \zeta_{++} \right\}, $$
$$(2.38)$$

with

$$\zeta_\pm = \frac{\pi \hbar}{4N} |V_\pm^{(3)}|^2 \Delta_\pm \frac{\delta(\omega_\lambda \pm \omega_{\lambda_1} - \omega_{\lambda_2})}{\omega_\lambda \omega_{\lambda_1} \omega_{\lambda_2}}, \qquad (2.39)$$

$$\zeta_{\pm\pm} = \frac{\pi \hbar^2}{8N^2} |V_{\pm\pm}^{(4)}|^2 \Delta_{\pm\pm} \frac{\delta(\omega_\lambda \pm \omega_{\lambda_1} \pm \omega_{\lambda_2} - \omega_{\lambda_3})}{\omega_\lambda \omega_{\lambda_1} \omega_{\lambda_2} \omega_{\lambda_3}}, \qquad (2.40)$$

where $V_{\pm}^{(3)}$ and $V_{\pm\pm}^{(4)}$ are in turn given by

$$V_{\pm}^{(3)} = \sum_{b,l_1b_1,l_2b_2} \sum_{\alpha\alpha_1\alpha_2} \Phi_{0b,l_1b_1,l_2b_2}^{\alpha\alpha_1\alpha_2} \frac{e_{\alpha b}^{\lambda} e_{\alpha_1 b_1}^{\pm\lambda_1} e_{\alpha_2 b_2}^{-\lambda_2}}{\sqrt{m_b m_{b_1} m_{b_2}}} e^{\pm i\mathbf{k}_1 \cdot \mathbf{r}_{l_1}} e^{-i\mathbf{k}_2 \cdot \mathbf{r}_{l_2}}, \qquad (2.41)$$

$$V_{\pm\pm}^{(4)} = \sum_{b,l_1b_1,l_2b_2,l_3b_3} \sum_{\alpha\alpha_1\alpha_2\alpha_3} \Phi_{0b,l_1b_1,l_2b_2,l_3b_3}^{\alpha\alpha_1\alpha_2\alpha_3} \frac{e_{\alpha b}^{\lambda} e_{\alpha_1 b_1}^{\pm\lambda_1} e_{\alpha_2 b_2}^{\pm\lambda_2} e_{\alpha_3 b_3}^{-\lambda_3}}{\sqrt{m_b m_{b_1} m_{b_2} m_{b_3}}} e^{\pm i\mathbf{k}_1 \cdot \mathbf{r}_{l_1}} e^{\pm i\mathbf{k}_2 \cdot \mathbf{r}_{l_2}} e^{-i\mathbf{k}_3 \cdot \mathbf{r}_{l_3}}.$$

$$(2.42)$$

In the above equations, l, b, and α are indexes of primitive cells, basis atoms, and cartesian coordinates, respectively; m is the atomic mass, and $\mathbf{r}$ is the lattice vector of the primitive cell; $\mathbf{k}$, n_{λ}^0, ω_{λ}, and e^{λ} are phonon wave vector, equilibrium occupation number, frequency, and eigenvector, respectively; $\Phi_{0b,l_1b_1,l_2b_2}^{\alpha\alpha_1\alpha_2}$ and $\Phi_{0b,l_1b_1,l_2b_2,l_3b_3}^{\alpha\alpha_1\alpha_2\alpha_3}$ are the third and fourth order IFCs, respectively. In the three-phonon processes, ζ_- represents the splitting process ($\lambda \to \lambda_1 + \lambda_2$) and ζ_+ indicates the combination process ($\lambda + \lambda_1 \to \lambda_2$). Similarly, ζ_{--}, ζ_{+-} and ζ_{++} represent the splitting ($\lambda \to \lambda_1 + \lambda_2 + \lambda_3$), redistribution ($\lambda + \lambda_1 \to \lambda_2 + \lambda_3$), and combination ($\lambda + \lambda_1 + \lambda_2 \to \lambda_3$) in the four-phonon processes[57]. In both three- and four-phonon processes, momentum conservation is strictly enforced as indicated by $\Delta_{\pm}$ and $\Delta_{\pm\pm}$, and energy conservation is enforced by δ functions, which are approximated by adaptive and regular Gaussian smearing[61,62] in computing $\tau_{3,\lambda}^{-1}$ and $\tau_{4,\lambda}^{-1}$, respectively.

Iterative and non-iterative solutions of BTE

Phonon BTE under RTA can be linearized; when solved non-self-consistently, their solutions are within the single mode relaxation approximation (SMRTA) and when solved iteratively, they are within the relaxation time approximation, respectively. Within the SMRTA, scattering rates arise from both normal (N) and Umklapp (U) processes, which lead to underestimation of κ_l since N processes do not introduce thermal resistance directly. For systems

24

with significant N processes, an iterative solution to the linearized BTE should be pursued by accounting for non-equilibrium phonon distribution through iteratively refining phonon populations[63–65]. In chapter 3, we calculate three-phonon scattering rates by solving the phonon BTE in an iterative manner. Considering the extremely high computational cost of including additional four-phonon scattering in the iterative solver, we treat four-phonon scattering non-iteratively, and combine them with three-phonon scattering rates based on Matthiessen's rule to give the total scattering rates. We found that this strategy leads to reasonably accurate lattice thermal conductivity for compounds which are dominated by U processes, such as PbTe, as discussed in detail in an earlier study[66].

2.3.2   Temperature-dependent Frequencies: Anharmonic Phonon Renormalization

Several first-principles phonon renormalization (PRN) schemes based either on real or reciprocal space formalism have been introduced to treat strong anharmonicity effects on phonon frequencies[67–71]. In chapter 3, we utilized the real space based PRN scheme introduced in Ref.[72] to compute temperature-dependent phonon frequencies and eigenvectors[66]. The temperature effects are taken into account by constructing temperature-dependent effective harmonic potential coefficients[73] which include the temperature-dependent corrections from higher-order IFCs on top of harmonic IFCs[66]. We refer the reader to Refs.[66,74] for detailed discussions.

Assuming that a crystal structure stays in a local equilibrium position, the force $F_{\mathbf{a}}$ experienced by atom a can be expressed as a Taylor expansion in terms of atomic displacements and IFCs

$$F_{\mathbf{a}} = -\Phi_{\mathbf{ab}}^{(2)} u_{\mathbf{b}} - \frac{1}{2!}\Phi_{\mathbf{abc}}^{(3)} u_{\mathbf{b}} u_{\mathbf{c}} - \frac{1}{3!}\Phi_{\mathbf{abcd}}^{(4)} u_{\mathbf{b}} u_{\mathbf{c}} u_{\mathbf{d}}, \qquad (2.43)$$

where $u_{\mathbf{a}} \equiv u_{a,\alpha}$ is the displacement of atom a in the Cartesian direction α, and $\Phi^{(n)}$ is the

nth-order IFCs. One can further write it in a compact form

$$\mathbf{F} = \begin{bmatrix} \mathbb{A}^{(2)} & \mathbb{A}^{(3)} & \mathbb{A}^{(4)} \end{bmatrix} \begin{bmatrix} \mathbf{\Phi}^{(2)} & \mathbf{\Phi}^{(3)} & \mathbf{\Phi}^{(4)} \end{bmatrix}^{\top}, \tag{2.44}$$

where $\mathbb{A}^{(n)}$ is a matrix formed by the products of the atomic displacements, and for example,

$$\mathbb{A}^{(4)} = -\frac{1}{3!} \begin{bmatrix} u_{\mathbf{b}}^1 u_{\mathbf{c}}^1 u_{\mathbf{d}}^1 & \cdots \\ \cdots & \\ u_{\mathbf{b}}^L u_{\mathbf{c}}^L u_{\mathbf{d}}^L & \cdots \end{bmatrix}, \tag{2.45}$$

where the superscripts represent different atomic configurations for a given supercell. If one assumes that there is a set of effective harmonic IFCs $\mathbf{\Phi}^{(2)\prime}$ that best represent the forces experienced by atoms, i.e.,

$$\mathbf{F} = \mathbb{A}^{(2)} \mathbf{\Phi}^{(2)\prime}, \tag{2.46}$$

$\mathbf{\Phi}^{(2)\prime}$ can be obtained by adding corrections from higher-order IFCs to $\mathbf{\Phi}^{(2)}$

$$\mathbf{\Phi}^{(2)\prime} = \mathbf{\Phi}^{(2)} + \mathbb{A}^{(2)-1} \mathbb{A}^{(3)} \mathbf{\Phi}^{(3)} + \mathbb{A}^{(2)-1} \mathbb{A}^{(4)} \mathbf{\Phi}^{(4)}. \tag{2.47}$$

To solve Eq. (2.47), one needs to extract accurate high-order IFCs from first-principles calculations, which in Chapter 3 are obtained using the recently developed compressive sensing lattice dynamics (CSLD).[75] To compute $\mathbb{A}^{(n)}$, we generate temperature-dependent atomic displacements according to a quantum covariance matrix $\Sigma_{u_{\mathbf{a}}, u_{\mathbf{b}}}$[68,71] for atoms in a given supercell

$$\Sigma_{u_{\mathbf{a}}, u_{\mathbf{b}}} = \frac{\hbar}{2\sqrt{m_a m_b}} \sum_{\lambda} \frac{(1 + 2n_{\lambda}^0)}{\omega_{\lambda}} e_{\mathbf{a}}^{\lambda} e_{\mathbf{b}}^{\lambda *}, \tag{2.48}$$

where n_{λ}^0 and ω_{λ} are Bose-Einstein distribution function and vibrational frequency of phonon mode λ. m_a and $e_{\mathbf{a}}^{\lambda}$ are atomic mass and phonon eigenvector projected on atom a, respectively. For a given temperature, Eq. (2.47) and (2.48) can be iterated to refine $\mathbf{\Phi}^{(2)\prime}$, the convergence of which can be controlled by monitoring phonon frequency and vibrational free

energy. To speed up the calculation, we further explore the linear constraint from space group symmetry and translational symmetry on $\Phi^{(n)}$ to reduce its dimension. Numerical benchmarks on strongly anharmonic systems including PbTe and $SrTiO_3$ showed good agreement with other PRN schemes and experimental results[70]

2.3.3   Statistics
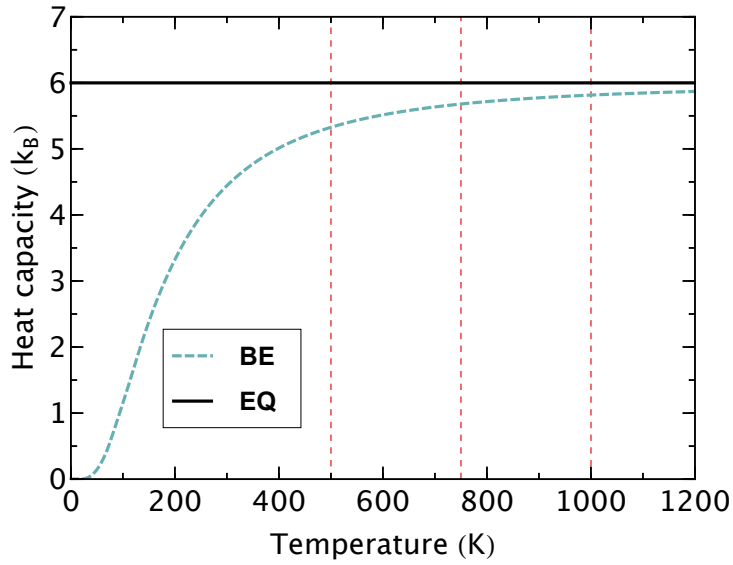
Figure 2.3: Constant volume heat capacity as a function of temperature for MgO. Blue dashed lines display the results computed using Bose-Einstein (BE) statistics and black solid lines denote equipartition (EQ) as demonstrated in MD simulations. The dashed red lines indicate 500 K, 750 K and 1000 K.

.

In the expression of the thermal conductivity obtained from the BTE (Eq. 2.36), the phonon statistics enter both the definition of the heat capacity and that of the scattering rates (inverse of relaxation time). According to Bose-Einstein (BE) statistics, the phonon population of mode λ in equilibrium is

$$n_\lambda^0 = \frac{1}{e^{\hbar\omega_\lambda/k_BT} - 1},$$
(2.49)

which leads to a mode heat capacity of

$$C_\lambda = k_{\mathrm{B}} \left(\frac{\hbar \omega_\lambda}{k_{\mathrm{B}} T} \right)^2 \frac{e^{\hbar \omega_\lambda / k_{\mathrm{B}} T}}{\left(e^{\hbar \omega_\lambda / k_{\mathrm{B}} T} - 1 \right)^2}. \tag{2.50}$$

In the classical (equipartition) limit, each phonon mode has an energy of $k_{\mathrm{B}} T$ and population of $k_{\mathrm{B}} T / \hbar \omega_\lambda$, thus giving rise to a temperature-independent mode heat capacity of k_{B}. The classical limit always overestimates the heat capacity (see Fig. 2.3), particularly at low temperatures. Specifically in the case of MgO, the classical limit leads to overestimates in the heat capacity of 11.2%, 5.3% and 3.1% at 500 K, 750 K and 1000 K, respectively.

As rigorously derived by Feng and Ruan[57], phonon population in the classical limit (equipartition) cannot be directly used to compute three- and four-phonon scattering rates in Eq. 2.37 and 2.38, since the resulting relaxation time is not properly defined from the linearized BTE. However, since classical limit and BE statistics do converge to the same limit at high temperature, in Chapter 3 we utilized the equipartition phonon occupation in Eq. 2.37 and 2.38 to compute scattering rates in order to compare with molecular dynamics simulations performed at high T.

Calculation of Phonon Lifetimes using MD

An alternative way to compute phonon lifetime, occupation and frequency shift consists in combining the phonon properties computed using ALD and MD. Before starting our simulations, one can compute the phonon frequencies and eigenvectors for the target temperature using the phonon renormalization (PRN) scheme described in Ref.[66]. Once the phonon frequencies ω_λ and eigenvectors e_λ are known, the energy of each phonon mode can be computed during a MD simulation as a function of time. The energy of a phonon mode λ is calculated as

$$E_\lambda(t) = K_\lambda(t) + U_\lambda(t) \tag{2.51}$$

where K and V are, respectively, the kinetic and potential components of the energy of the phonon mode. The kinetic component is calculated from the projection $\dot{q}$ of the phonon mode on the velocities v of the atoms. The potential component is calculated by projecting onto the displacement u of the atoms from their equilibrium positions r_0, i.e.

$$K_\lambda(t) = \frac{1}{2N}\|\dot{q}_\lambda\|^2 \qquad U_\lambda(t) = \frac{1}{2N}\omega_\lambda^2\|q_\lambda\|^2 \tag{2.52}$$

$$\dot{q}_\lambda = \sum_{l,b} \sqrt{\frac{m_b}{N}} e^{i\vec{k}\vec{r}_0(l,b)} \vec{e}_{b,\lambda}^{\,*} \cdot v(l,b,t) \tag{2.53}$$

$$q_\lambda = \sum_{l,b} \sqrt{\frac{m_b}{N}} e^{i\vec{k}\vec{r}_0(l,b)} \vec{e}_{b,\lambda}^{\,*} \cdot u(l,b,t) \tag{2.54}$$

Here, l and b are indices over the primitive cells and the atoms inside a primitive cell, respectively. N is the number of atoms in the system, m_b is the mass of atom b, and ω_λ is the frequency of the phonon mode λ. The displacement u is given by $u(t) = r(t) - r_0(t)$. The vector $\vec{e}_{b,\lambda}$ describes the direction and phase of the displacement of atom b due to the phonon with wavevector $\vec{k}$ and polarization λ.

The lifetime of each phonon mode is then calculated from the normalized autocorrelation of the energy:

$$\tau_\lambda = \int_0^\infty \frac{\langle E_\lambda(0)E_\lambda(t)\rangle}{\langle E_\lambda(0)E_\lambda(0)\rangle} \mathrm{d}t \tag{2.55}$$

In order to reduce the noise due to the tail of the autocorrelation, the lifetime can be computed from a fit to the equation

$$\frac{\langle E_\lambda(0)E_\lambda(t)\rangle}{\langle E_\lambda(0)E_\lambda(0)\rangle} = e^{-t/\tau_\lambda} \tag{2.56}$$

with the lifetime τ_λ as a single fitting parameter. In Chapter 3 lifetimes are computed as described above during an NVE simulation, once the system is prepared at the target temperature using a Nose-Hoover[76] thermostat.

The lifetimes from MD were computed using a parallel python code, called pyTauMD, which

we developed and will be described in an upcoming publication. Briefly, the main steps of the workflow are the following: (i) Calculation of the dynamical matrix from the second derivative of the potential energy E. (ii) Diagonalization of the latter to compute phonon eigenvectors and frequency. If those are already available, it is possible to skip steps one and two. (iii) Evaluation of the energy per mode as a function of time, using the scalar product of the phonon eigenvector on the velocities and displacement of the atoms following equations 2.52-2.54. (iv) The average number of phonons is obtained from the average energy of a phonon mode as computed during MD, divided by the energy of a single phonon $\hbar\omega$. (v) The lifetime τ of a phonon mode is then computed using the autocorrelation of the energy as described in Eq. 2.56.

Average Phonon Occupation

The classical Hamiltonian of a system of vibrating atoms can be written, in the harmonic approximation, as a sum of kinetic and potential energy over phonon modes:

$$H_{harm}(\{q, \dot{q}\}) = \sum_{\lambda} \left[\frac{1}{2N}\|\dot{q}_\lambda\|^2 + \frac{1}{2N}\omega_\lambda^2\|q_\lambda\|^2 \right] \tag{2.57}$$

As a consequence of the equipartition theorem, the average kinetic and potential energy for each phonon mode is equal to $k_B T/2$. Each phonon mode has an average energy and phonon number given by:

$$\langle E_\lambda \rangle = k_B T \qquad \langle n_\lambda \rangle = \frac{k_B T}{\hbar\omega_\lambda} \tag{2.58}$$

From the procedure used to calculate the phonon lifetimes, described above, one can obtain the phonon energy averaged over time

$$\langle E_\lambda \rangle = \frac{1}{\Gamma} \int_0^\Gamma E_\lambda(t)\mathrm{d}t \tag{2.59}$$

where here Γ is the total simulation time, and the mode-by-mode average phonon occupation number $\langle n_\lambda \rangle$ is

$$\langle n_\lambda \rangle = \frac{\langle E_\lambda \rangle}{\hbar \omega_\lambda} \tag{2.60}$$

Frequency Shifts

Phonon frequencies are dependent on temperature due to different degrees of atomic displacements from their equilibrium positions as a function of T, amounting to sampling different portions of the anharmonic potential energy surfaces. This change in phonon frequencies as a function of T (which we call shift in phonon frequencies relative to their T=0 value, or phonon renormalization) naturally manifests itself in MD simulations. In our analysis in Chapter 3, we compute the frequency shift from the kinetic part $K_\lambda(t)$ of the phonon mode energy. We fit its normalized time autocorrelation function to the equation

$$\frac{\langle K_\lambda(0) K_\lambda(t) \rangle}{\langle K_\lambda(0) K_\lambda(0) \rangle} = e^{-t/\tau_\lambda} \cos^2 \omega_\lambda(T) \tag{2.61}$$

where we added the dependence (T) to the frequency ω_λ. The frequency shift is then defined as the difference between the frequency obtained during MD simulations and that obtained from diagonalizing the dynamical matrix at T=0. Note that this procedure does not include effects arising from the temperature-dependent change in lattice constant, as we compute both frequencies at the same lattice constant.

2.4 Comparison of Green-Kubo and Boltzmann Transport Equation based methods

While MD and ALD are fundamentally distinct and practically disparate approaches, they have nonetheless both been shown to give reasonably accurate predictions for similar systems[57,77,78]. Typically, GK calculations are performed using classical MD where the potential energy is given by an interatomic potential as a function of the positions of the atoms.

Recently, Marcolongo et. al.[22] and Carbogno et al.[79] showed that the Green-Kubo formalism can be applied to ab initio MD, although the method of Ref.[79] is limited to solids and contains approximations on the partition of slow and fast vibrational modes.

We note that the Green-Kubo formalism does not rely on the definition of phonons and is generally applicable: it can describe conductive heat transport in crystalline or amorphous materials, materials with defects, nanostructures, and fluids. The GK method implicitly accounts for all anharmonic terms in the potential energy. In BTE language, this would translate to including all phonons processes in the perturbative expansion (instead of only up to the third or fourth order), thus allowing for greater accuracy at high temperatures.

Nonetheless, the GK method suffers from three deficiencies: (i) being based on classical MD, it is not known how to include quantum effects such as zero point energy or quantization of the phonon energy levels, leading to lower accuracy at low temperatures. This problem is of a theoretical nature and, to our knowledge, has not been solved, although semi-empirical corrections have been proposed[80,81]; (ii) long simulation times (order of ns) are needed for convergence, especially for systems with high values of thermal conductivity, mostly due to noise in the long time tail of the heat flux autocorrelation function. Acceleration is possible based on the methods proposed in Ref.[54] or[79], although the latter one is limited to crystals and based on phonon theory; and (iii) the value of the thermal conductivity calculated in a GK simulation is a function of the number of atoms included in the MD cell, converging in the infinite limit to the bulk value. Currently, no theory or model exists to predict or extrapolate to the thermodynamic limit, leading to the necessity of simulating at various cell sizes with increasing numbers of atoms until satisfactory convergence is obtained. We refer to[78] for a detailed study.

Meanwhile, phonon-based ALD approaches for calculating lattice thermal conductivity, applicable to crystalline systems, have been developed based on the Boltzmann transport equation (BTE), with the central assumption that collective vibrations can be thought of as quasi-particles termed phonons which have explicit group velocities and scatter with each

other[82–84]. Within these approaches, the lattice thermal conductivity is calculated by solving the BTE, under the relaxation time approximation, with relaxation times obtained using perturbation theory and considering anharmonic phonon-phonon interactions, such as three- and four-phonon scattering processes[57,60,65,85,86].

The BTE-ALD approach is more advantageous compared with MD-based method in the following respect: (i) the quantum (Bose-Einstein) statistics is utilized, thus (presumably) attaining better accuracy at low temperatures; (ii) first-principles calculations may be used to obtain third and fourth order force constants in a relatively straightforward manner for a variety of systems, to accurately model heat transport in bulk crystals with relatively low computational costs, and computation for larger systems in some cases can be parallelized[62,75,85,87]; and (iii) convergence issues with respect to system size and sampling are less severe than in MD.

However, BTE-ALD suffers from several deficiencies: (i) the approach depends on the assumption that lattice vibrations can be treated as quasiparticles, i.e., both the anharmonic frequency shift and broadening (real and imaginary part of the phonon self-energy) are relatively small compared to the phonon frequency, and fails when quasiparticles are not well-defined, such as in the localization limit in systems with strong intrinsic disorder[88,89]; An alternative approach was recently developed[90], based on the definition of a new class of collective excitation, called relaxons, as linear combinations of phonons; (ii) the approach is based on perturbation theory, which is accurate only in the perturbative limit and may fail in severely anharmonic systems or at high temperatures since the scattering processes are limited to third or at most fourth order; and (iii) it is difficult to use the phonon BTE method to model heat transport in non-crystalline systems including defects and nanostructures, and the approach cannot be applied to fluids or even solids when diffusion occurs.

CHAPTER 3

A COMPARISON OF MOLECULAR DYNAMICS AND BOLTZMANN TRANSPORT APPROACHES

3.1   Introduction

As described in the previous chapter, two major approaches, namely molecular dynamics (MD) simulations and calculations solving approximately the Boltzmann transport equation (BTE), have been developed to compute the lattice thermal conductivity. In this chapter we present a detailed direct comparison of these two approaches, using as prototypical cases MgO and PbTe. The comparison, carried out using empirical potentials, takes into account the effects of fourth order phonon scattering, temperature-dependent phonon frequencies (phonon renormalization), and investigates the effects of quantum vs. classical statistics. We clarify that equipartition, as opposed to Maxwell Boltzmann, govern the statistics of phonons in MD simulations. We find that lattice thermal conductivity values from MD and BTE show an apparent, satisfactory agreement; however such an agreement is the result of error cancellations. We also show that the primary effect of statistics on thermal conductivity is via the scattering rate dependence on phonon populations. We aim to provide a controlled, comprehensive, and systematic comparison of MD vs. ALD-BTE based approaches for the prediction of lattice thermal conductivity.

In an earlier study[77], Turney *et al.* presented and compared methods in several categories: (1) quasi-harmonic and anharmonic lattice dynamics calculations, (2) a combination of quasi-harmonic lattice dynamics calculations and molecular dynamics simulations, and (3) Green-Kubo and direct molecular dynamics, to assess their validity. They pointed out that the lattice dynamics calculations tend to underestimate lattice thermal conductivity at above half of the Debye temperature. However, their lattice dynamics calculations excluded higher-than-third-order anharmonic phonon-phonon interactions. In addition, the impact of different statistics (quantum vs. classical) on calculated thermal conductivity was not clarified.

In a follow-on study, the same authors[91] assessed different corrections to MD simulations to account for quantum statistics, using silicon and the Stillinger Weber potential. They found that these corrections failed at low temperatures due to the classical distribution of phonon modes. He *et al.*[78] compared the GK-MD and BTE approaches for the computation of thermal conductivity of Si, Ge, and Si-Ge alloys, and found that the results are consistent for the pure compounds, though alloy systems prove to be problematic for BTE. In this study, some investigations into the effects of quantum statistics were carried out via the use of classical statistics in BTE. In addition, the effects of temperature-induced anharmonic phonon renormalization or higher-than-third-order interactions were again not considered. Since several of the previous studies were carried out on Si or related systems, it is of interest to test the results on more diverse types of systems.

In order to accomplish a meaningful comparison, we select two representative systems: a small-gap semiconductor with low lattice thermal conductivity (PbTe), and an insulator with higher lattice thermal conductivity (MgO). These two materials have the further advantage of having simple structures. For each material, we use MD and BTE-ALD, with the same interatomic potential, to evaluate the temperature-dependent values of the lattice thermal conductivity well below, near, and well above their respective Debye temperatures. We further investigate the source of the differences between the two approaches by deriving lifetimes from MD simulations, considering heat capacities and phonon occupancies under different treatment of statistics, and using these quantities in the BTE expression. The goal is to determine the underlying physical reasons for divergences and convergences between the two approaches.

3.2   Model Systems and Interatomic Potentials

To ensure that any differences in computed thermal conductivity arise solely from the treatment of heat transport (i.e. atoms vs. phonons), we used the same interatomic potential for both MD and BTE calculations. For MgO, we used the potential described in Ref.[92]; for

PbTe, we used the potential from Ref.[93]. Both potentials are of the Buckingham-Coulomb type. The MgO potential was shown[92] to predict experimental lattice constant, thermal expansion and thermal conductivity reasonably well in the 300K-1500K range. The PbTe potential developed by Qiu *et al.*[93] was shown to reasonably reproduce the mechanical and vibrational properties of PbTe bulk crystal, as well as lattice thermal conductivity. We studied MgO at 500K, 750K, and 1000K and PbTe at 100K, 150K, and 300K. The experimental Debye temperatures of MgO and PbTe are 743K[94] and 177K[95], respectively. To account for thermal expansion, the lattice parameters computed from NPT MD simulations at each temperature were used.

3.2.1 Molecular Dynamics: computational details

All classical simulations were performed using LAMMPS[96]. The MgO samples contain 32768 (500-750K) or 4096 (1000K) atoms, with the smaller number of atoms for higher temperature due to the shorter mean free path at higher temperature. The PbTe samples contain 8192 atoms. For all systems, Nose-Hoover NVT equilibration runs of 20 ps for MgO and 100 ps for PbTe were followed by NVE simulations of 3 ns to obtain the lattice thermal conductivity (κ). For each temperature and material, 4-9 GK MD runs were performed, to give a total of 12-27 ns of statistics. The time step used for MgO is 1 fs whereas that for PbTe is 0.5 fs. The MgO 500K and 1000K data are from the Supporting Information in Ref.[27].

3.2.2 Boltzmann Transport Equation: computational details

In the BTE-ALD calculations, for both MgO and PbTe, we used 6×6×6 supercells to extract harmonic and anharmonic interatomic force constants (IFCs) up to the fourth order using compressive sensing lattice dynamics[75]. There is no explicit cutoff distance enforced on the harmonic IFCs[97]. To further verify the extracted harmonic IFCs, we compare the calculated phonon dispersions with those independently obtained by Phonopy[98]. The cutoff distance of the third order IFCs is limited to the seventh nearest neighbor shell, which leads to

converged lattice thermal conductivity when only three-phonon interactions are accounted for. Considering the short-range nature of 4th-order anharmonicity[75] and the associated combinatorial growth in the number of parameters, the 4th-order IFCs are limited to the second nearest neighbor shell.

We also verified that the additional inclusion of the third nearest neighbor shell in the fourth order IFCs leads to negligible changes in both frequency shifts and lattice thermal conductivity. The phonon BTE with renormalized harmonic IFCs and anharmonic IFCs as input were solved using $\mathbf{q}$-point mesh of $16\times16\times16$ and $12\times12\times12$, respectively, which are deliberately chosen to be equivalent to the supercell structures used in MD simulations. All anharmonic lattice dynamics calculations were performed using an in-house customized ShengBTE package which further includes four-phonon scatterings for phonon lifetimes[62].
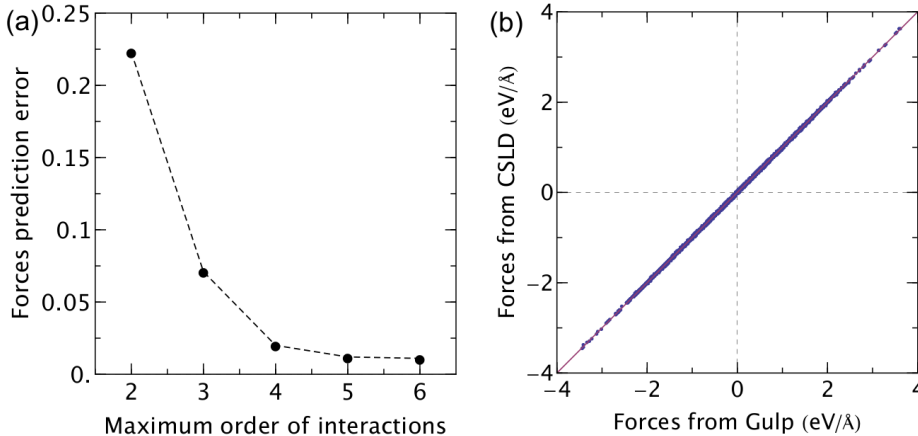
Figure 3.1: (a) Relative force prediction error by compressive sensing lattice dynamics as a function of included maximum order of interactions. (b) Comparison between predicted and Gulp-computed forces when interatomic force constants up to 6th-order are included.
.

The essential ingredients for the calculation of τ_λ^{-1} are harmonic and anharmonic interatomic force constants (IFCs). We utilized our recently-developed compressive sensing lattice dynamics (CSLD)[75] approach to extract both harmonic and anharmonic IFCs, which are obtained from a convex optimization problem that minimizes a weighted sum of the ℓ_1

norm of the IFCs $\mathbf{\Phi}$ and the root-mean-square fitting error

$$\mathbf{\Phi}^{\mathrm{CS}} = \arg\min_{\mathbf{\Phi}} \|\mathbf{\Phi}\|_1 + \frac{\mu}{2}\|\mathbf{F} - \mathbb{A}\mathbf{\Phi}\|_2^2, \tag{3.1}$$

where $\mathbf{F}$ is a vector composed of atomic forces calculated by DFT, and $\mathbb{A}$ is a matrix formed by the products the atomic displacements. The parameter μ is a tuning parameter used to control the relative weights of the force fitting error versus the sparsity of $\mathbf{\Phi}$ components. Since (1) small μ leads to sparse solution of $\mathbf{\Phi}$ at the expense of the accuracy of the fitted $\mathbf{\Phi}$ ("underfitting") and (2) large μ give a dense solution of $\mathbf{\Phi}$ but with poor predictive power ("overfitting"), an optimal μ is determined by monitoring the predictive relative error for a leave-out subset of the training data not used in fitting. To reduce the parameter space of $\mathbf{\Phi}$, linear constraints from crystal symmetry and translational symmetry are explored and strictly enforced by finding the null space representation of $\mathbf{\Phi}$. More details on numerical issues and the symmetrization of IFCs can be found in Ref.[70,75,99,100]. The dependence of force prediction error on the order of included interactions is given in 3.1

3.3   Results and Discussions

Phonon Dispersion Average Phonon Occupation

Our results for phonon numbers for MgO and PbTe at various temperatures are shown in Figure 3.4, where we compare the distributions obtained in our calculations against those predicted by equipartition, as well as the Maxwell-Boltzmann (MB) and Bose-Einstein (BE) statistics. The computed distributions deviate significantly from those of the MB distribution, illustrating that classical phonons in MD are distributed not via MB but equipartition (EQ). The computed distributions deviate also from BE statistics but the agreement improves with increasing temperature, as expected.
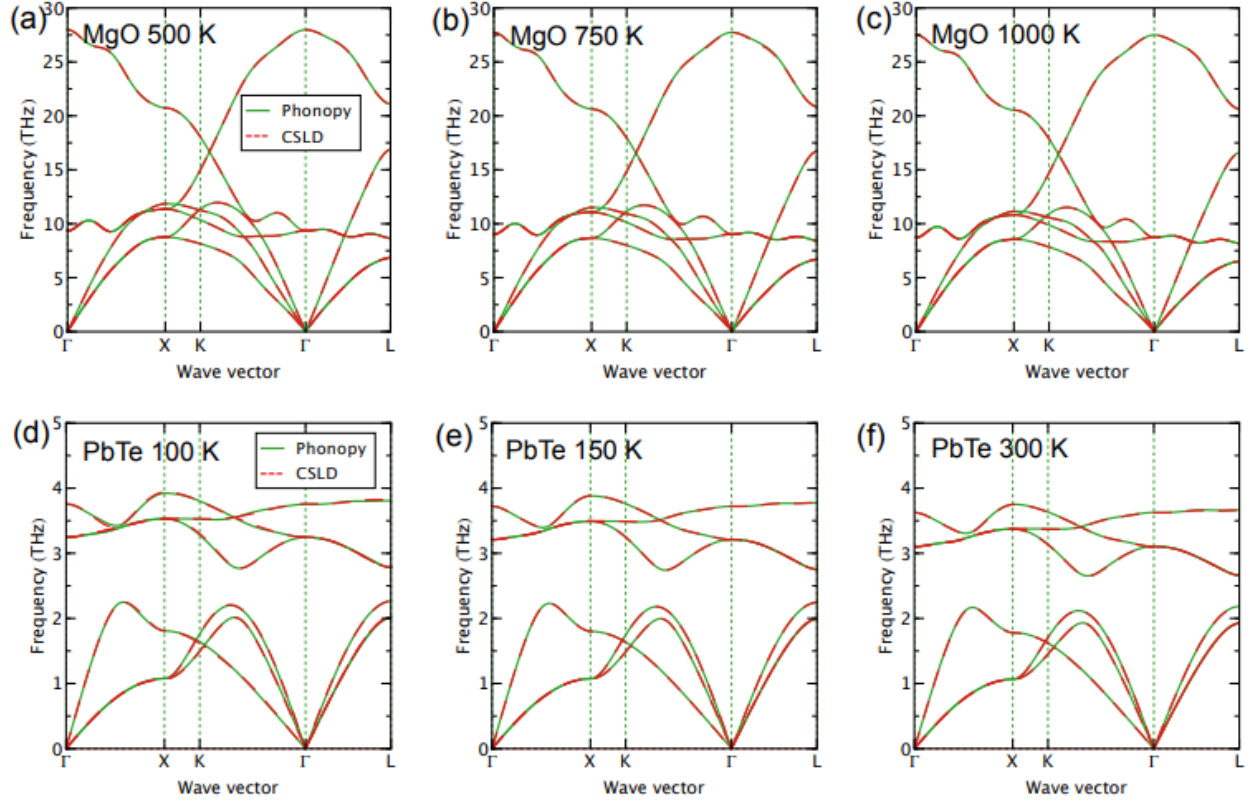
Figure 3.2: Comparison of phonon dispersions for MgO and PbTe calculated using Phonopy and compressive sensing lattice dynamics (CSLD). Temperature-dependent lattice parameters were determined by MD simulations.
.

3.3.1 Temperature-dependent phonon frequencies

It is instructive to compare the phonon frequencies and their changes as a function of temperature obtained using the two different approaches. Fig. 3.2 in the Supplemental Materials (SM) shows comparisons of phonon dispersions, showing that the fitted potential using CSLD gives similar dispersions to those obtained using finite displacements with the original interatomic potential. In Fig. 3.5, we show the mode-resolved frequency shifts as calculated in ALD and in MD, relative to the frequencies obtained from direct diagonalization. Fig. 3.3 displays the phonon density of states for these three cases. As expected, the frequency shifts increase with temperature. With the exception of high frequency MgO modes, the frequency shifts in MD are found to be smaller than the ones in ALD. The difference in frequency shifts

39
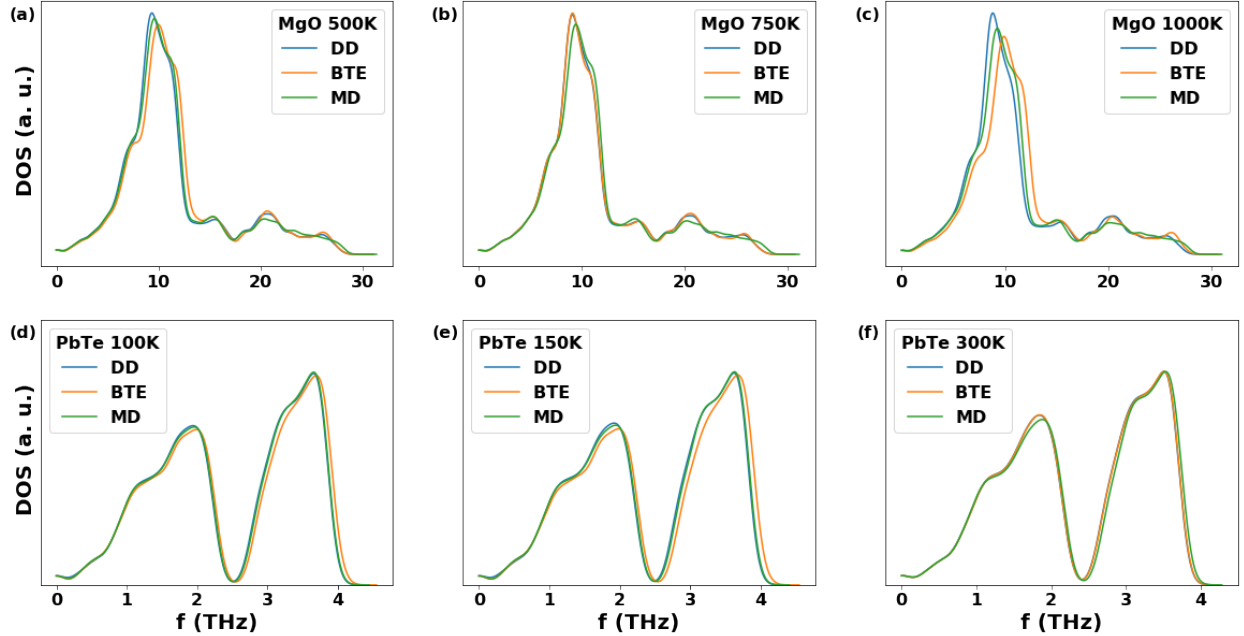
Figure 3.3: Phonon density of states plots for MgO at 500K (a), 750K (b), 1000K (c) and for PbTe at 100K (d), 150K (e) and 300K (f). DD (blue line) indicates the density of state calculated from the direct diagonalization of the dynamical matrix; BTE (orange) is the result of anharmonic lattice dynamics calculations and MD (green) is the result of molecular dynamics simulations.

between MD and ALD increases at high frequency, likely because of the different phonon distributions. This difference persists at high temperatures, despite an expected decrease in the difference between the two phonon distributions with increasing temperatures. Moreover, we note that the agreement between ALD and MD approaches is better in MgO, where frequency shifts are large ($\sim$1 THz), than in PbTe, where frequency shifts are on average 10 times smaller ($\sim$0.1 THz). To further confirm the ALD results, we performed additional self-consistent phonon (SCPH) calculations of frequency shifts in reciprocal space, as derived from many-body Green-function theory[56,70,101]; the results are found to agree with those obtained by the real space-based PRN scheme. This indicates that part of the discrepancies between MD and ALD may be numerical in nature.
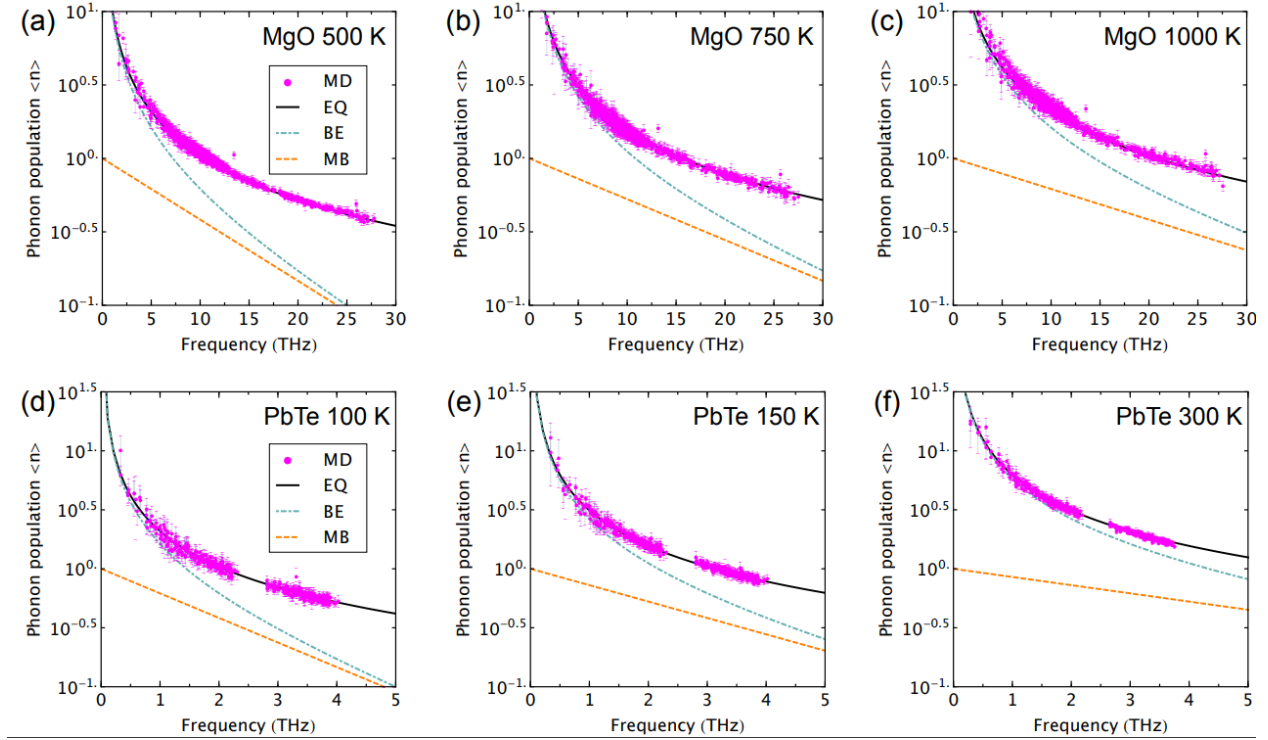
Figure 3.4: Phonon occupation per mode as a function of frequency for MgO at 500K (a), 750K (b) and 1000K (c) and PbTe at 100K (d), 150K (e) and 300K (f). For all materials and temperature, we compare the energy distribution calculated in our molecular dynamics (MD) simulations against three possible statistics: Bose-Einstein (BE) (blue dot-dashed lines), equipartition (EQ) (solid black lines) and Maxwell-Boltzmann (MB) (orange dashed lines).
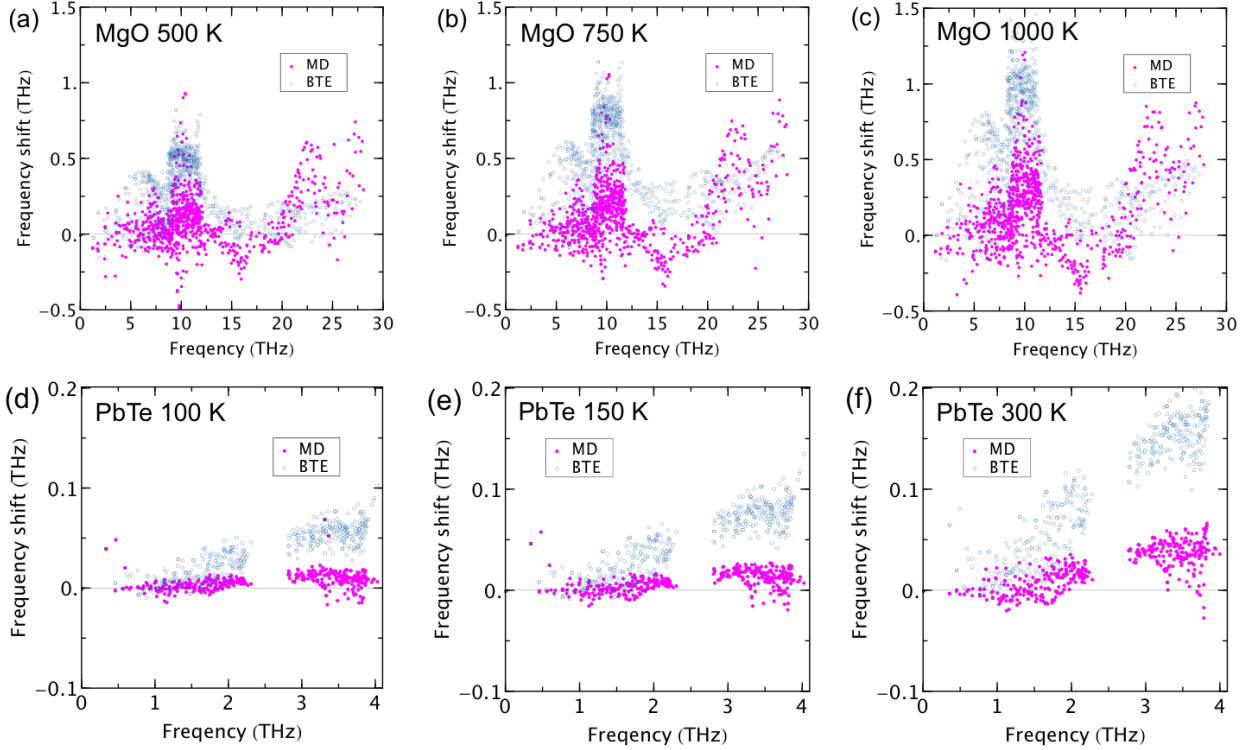
Figure 3.5: Mode-resolved frequency shift of MgO at finite temperatures [(a): 500 K; (b): 750 K; (c): 1000K] relative to the 0 K. Mode-resolved frequency shift of PbTe at finite temperatures [(d): 100 K; (e): 150 K; (f): 300K] relative to the 0 K. The solid magenta disks and empty blue circles denote results from molecular dynamics simulations and anharmonic phonon renormalization, respectively. The frequency shift from anharmonic phonon renormalization is computed using Bose-Einstein statistics. We also find that replacing Bose-Einstein with classical statistics leads to only very small changes in computed frequency shift (e.g, a relatively change of 8% and 2% for MgO at 500 K and 1000 K, respectively).

3.3.2 Phonon lifetimes

We compare the phonon mode-resolved scattering rates of MgO and PbTe obtained from MD and ALD at various temperatures in Fig. 3.7. To perform a valid comparison, we enforce equipartition for phonon population in ALD calculations, thus following the same statistics as in MD simulations. Overall, good agreement is found between MD and ALD results, despite the rather different formalisms based on atomic motion or phonon quasiparticles. In general, acoustic modes show much smaller scattering rates than those of optical modes, primarily due to the limited scattering phase space of low-frequency phonon modes. Scattering rates
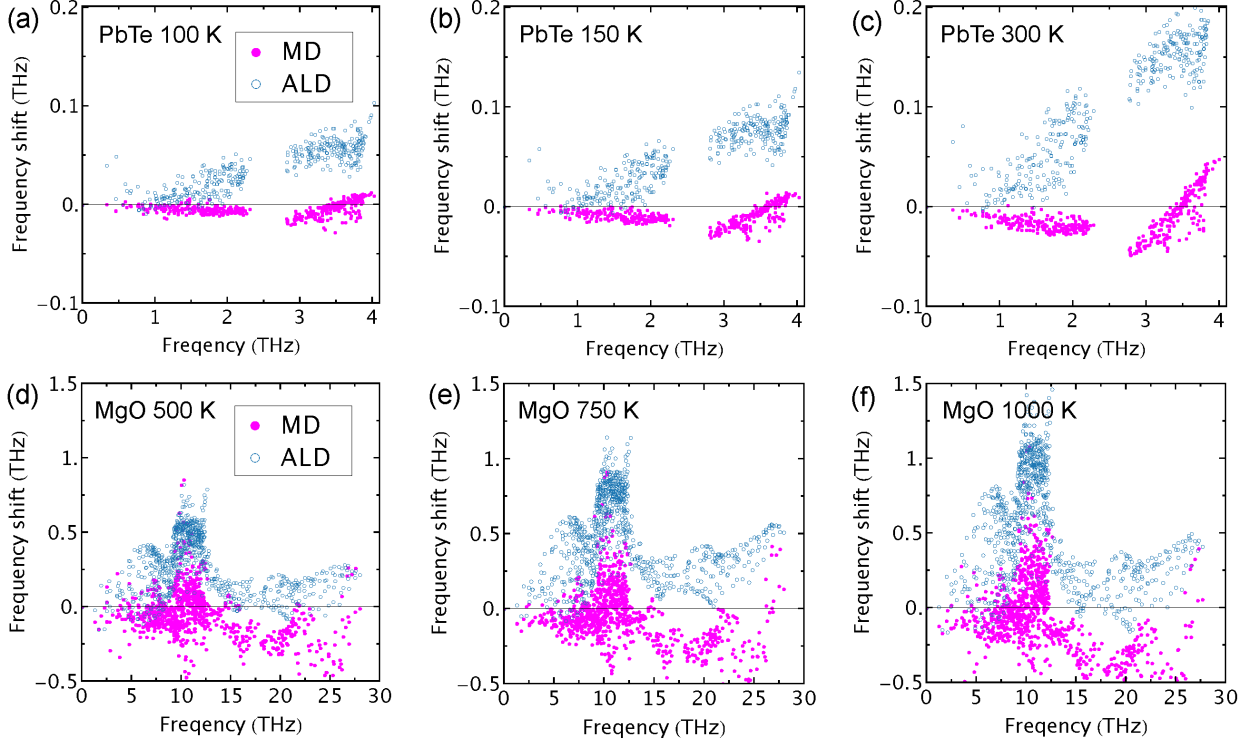
Figure 3.6: Mode-resolved frequency shift of MgO at finite temperatures [(a): 500 K; (b): 750 K; (c): 1000K] relative to the 0 K. Mode-resolved frequency shift of PbTe at finite temperatures [(d): 100 K; (e): 150 K; (f): 300K] relative to the 0 K. The solid magenta disks and empty blue circles denote results from molecular dynamics simulations and anharmonic phonon renormalization, respectively. Different from Fig.3.5, here the phonon frequency from molecular dynamics is obtained combining Eq 2.52 and equipartition by taking the ratio $\|q_\lambda\|^2/\|\dot{q}_\lambda\|^2$.

of both acoustic and optical modes increase with enhanced phonon populations at higher temperatures. We notice that, for both MgO and PbTe, scattering rates of acoustic modes obtained from the two methods agree well with each other, while those of optical modes are found to be smaller from MD simulations, but with decreased discrepancy between MD and ALD at high temperatures. We note that the larger discrepancy associated with the high-lying optical modes at relatively low temperatures might be due to the breakdown of the relaxation time approximation when equipartition is assumed for phonon population in the linearized BTE, while high temperature tends to reduce such discrepancy, as pointed out by Feng and Ruan[57]. To shed light on the impact of statistics on lifetimes in ALD calculations,
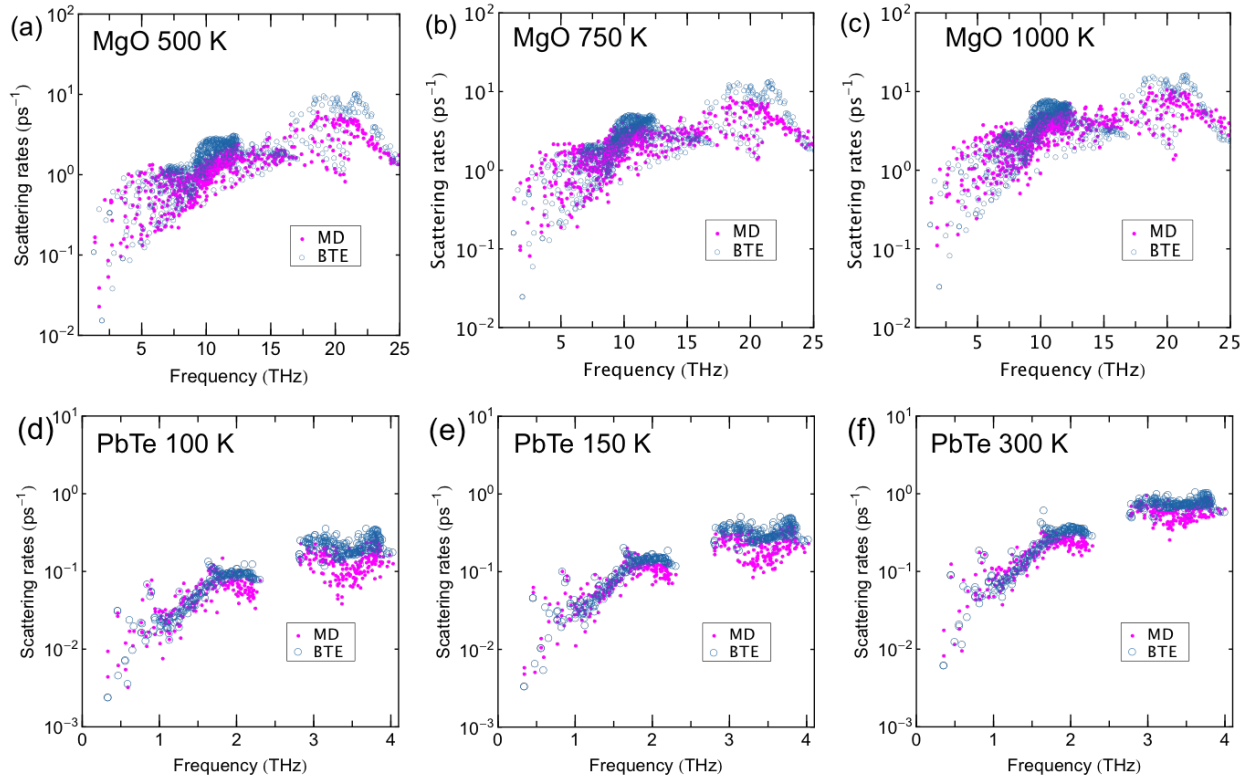
Figure 3.7: Comparison of mode-resolved scattering rates of MgO between molecular dynamics (MD) simulations and anharmonic lattice dynamics (ALD) calculations at (a) 500 K, (b) 750 K and (c) 1000 K. (d)-(f) the same as (a)-(c) but for PbTe at 100 K, 150 K and 300 K, respectively. Phonon populations were assumed to follow equipartition in ALD calculations.
.
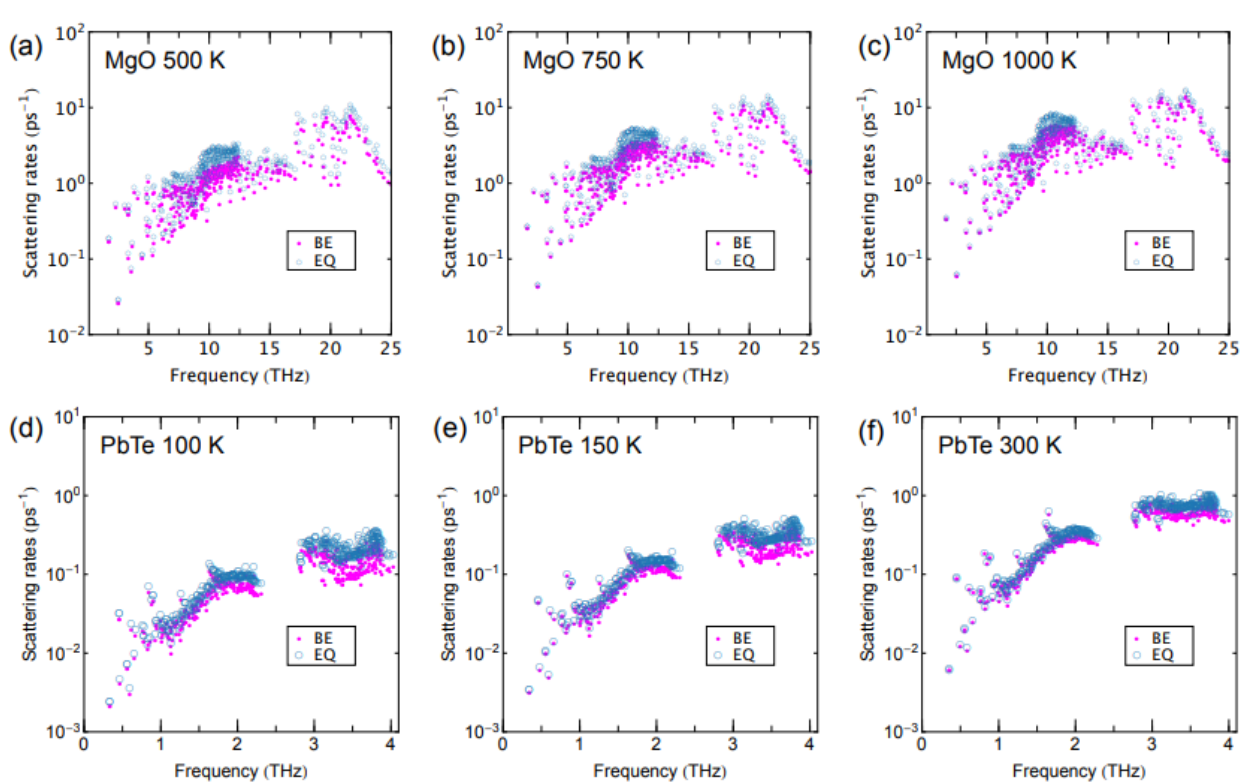
Figure 3.8: Comparison of mode-resolved scattering rates of MgO obtained by assuming Bose-Einstein statistic (BE) and classical equipartition (EQ) in anharmonic lattice dynamics (ALD) calculations at (a) 500 K, (b) 750 K and (c) 1000 K. (d)-(f) the same as (a)-(c) but for PbTe at 100 K, 150 K and 300 K, respectively.
.

we also compare the scattering rates calculated using phonon populations obeying Bose-Einstein statistics and equipartition, respectively, in Fig. S5 (see Supplementary Materials). Consistently, we find that equipartition leads to higher phonon scattering rates, and again, with decreased difference from those obtained by assuming Bose-Einstein statistics at higher temperatures. This discrepancy is deeply rooted in the fact that phonon populations from Bose-Einstein statistics and equipartition are different, particularly for the high-frequency optical phonons. It is the overall increased phonon populations in the case of equipartition that leads to higher phonon scattering rates. Our results suggest that phonon scattering rates calculated using Bose-Einstein statistics compare better with MD simulations than those from equipartition, particularly for the high-lying optical phonon modes. This agreement, however, may be accidental or suggest error cancellations.

45
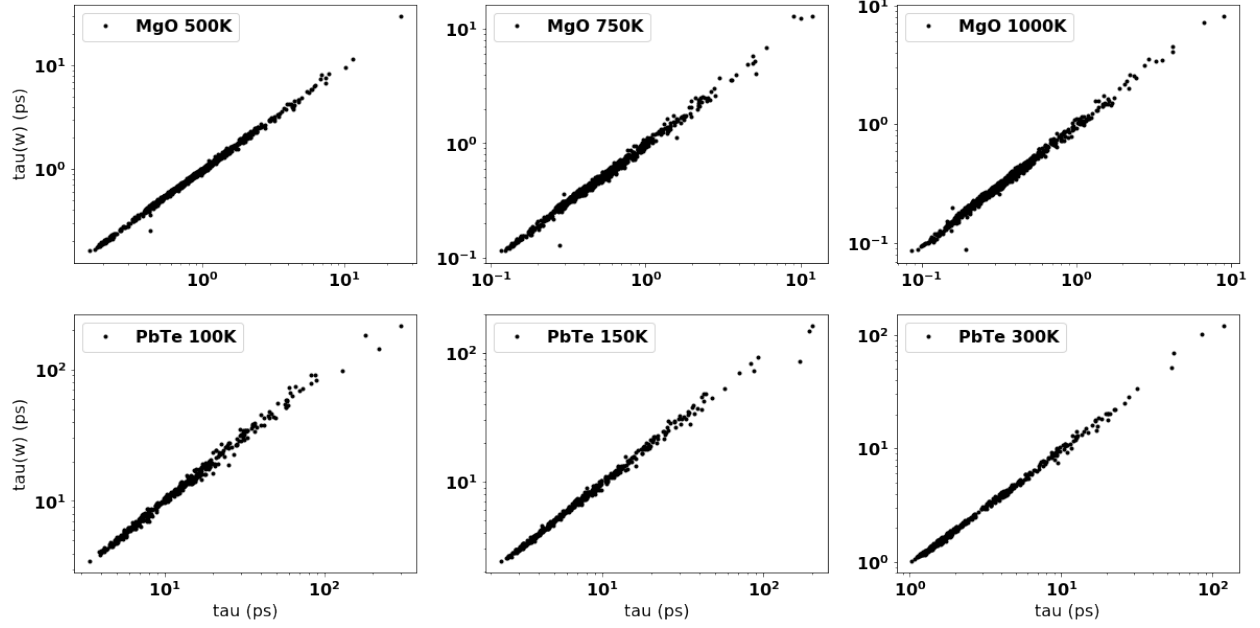
Figure 3.9: Lifetimes computed from Molecular Dynamics using two different expressions. The lifetimes calculated from Eq. 2.61 are plotted vs. those from Eq. 2.55.

To reveal the role of the higher-than-third-order phonon scattering processes in determining overall phonon scattering rates, we show the decomposed total scattering rates by separating them into contributions from three- and four-phonon processes for MgO and PbTe in Fig. 3.10. The MgO results reveal that the contribution of four-phonon scattering is comparable to that of three-phonon scattering at all temperatures studied here. Particularly, four-phonon scattering rates of optical modes with frequency of about 10 THz are even higher than those of three-phonon processes, highlighting the importance of including four-phonon scattering processes to accurately predict the thermal conductivity. It is also evident from the PbTe results that four-phonon scattering rates have a stronger temperature-dependence than three-phonon scattering rates, with increasing relative contributions to total scattering rates at higher temperatures.
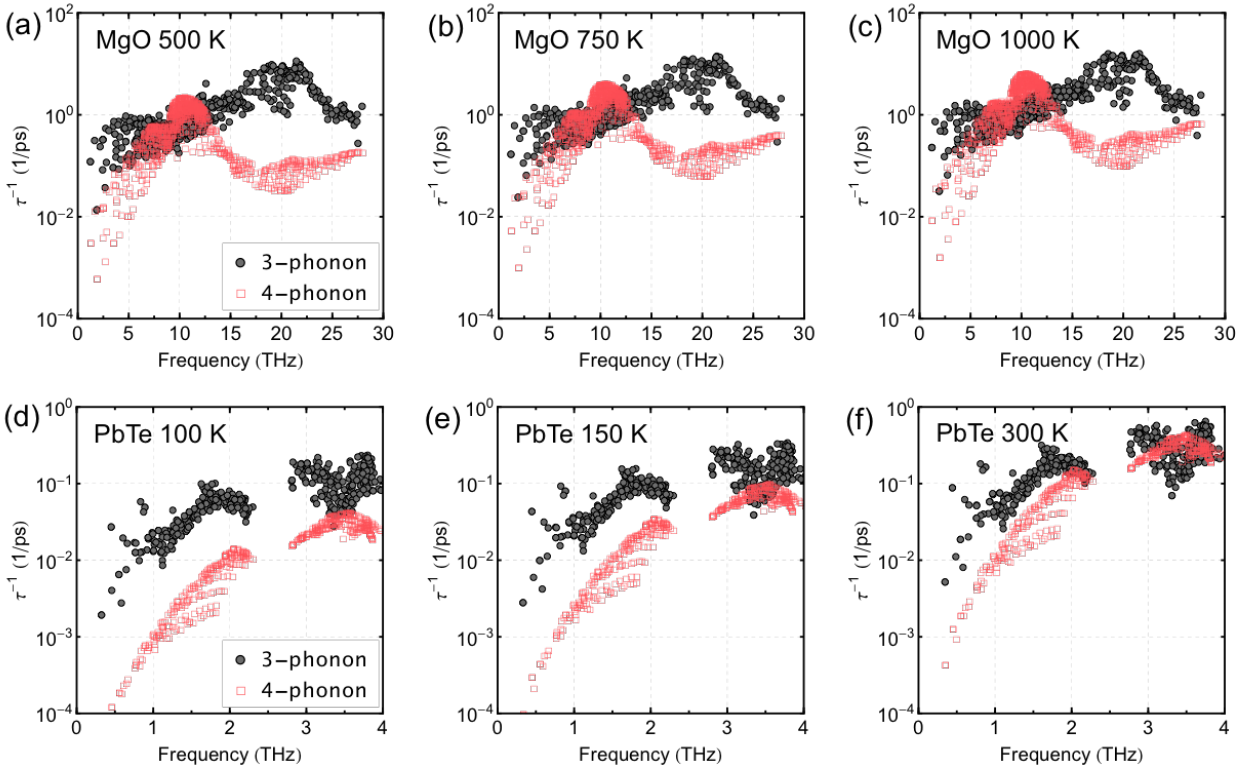
Figure 3.10: Decomposed three- and four-phonon scattering rates for MgO at (a) 500 K, (b) 750 K and (c) 1000 K, and PbTe at (d) 100 K, (e) 150 K and (f) 300 K.
.

3.3.3   Calculations of the Thermal Conductivity

Here we discuss our finding, summarized in Table 3.1, in which we use lifetimes obtained from MD simulations (τ_{MD}), as well as from three- and four-phonon scattering (τ_{BE}, in the BTE expression for thermal conductivity (Eq. 2.36). We also use the classical equipartition (C_{EQ}) and Bose-Einstein (C_{BE}) expressions for heat capacity in Eq. 2.36. All the above results are listed in comparison to the Green-Kubo (GK) thermal conductivity, and labeled approximations 1-7 or A1-A7 in Table 3.1. For MgO, the thermal conductivity values obtained from BTE using three- and four-phonon scattering processes, and Bose-Einstein statistics (A4 in Table 3.1), agrees strikingly well (to within 3%) with the Green-Kubo results (A7). For PbTe, however, the agreement is only satisfactory (within 16%). This agreement is better than previous comparisons (e.g. Ref.[77]), likely due to the inclusion of fourth-order phonon scattering in the BTE-ALD treatment. The agreement, however, may be due to a number of error cancellations, as explained below.

One significant difference between the MD and BTE approaches is the inclusion of phonon scattering processes to all orders in MD, as opposed to the order-by-order expansion in BTE. Because the rate of scattering processes at different orders are summed, i.e. via Matthiessen's rule, the inclusion of higher order should reduce the lifetimes and therefore the thermal conductivity. Indeed, substituting lifetimes from MD into the BTE expression with the BE expression for heat capacity (A2) results in lower thermal conductivity values compared to using BTE lifetimes (A4), due to the inclusion of higher-order scattering processes in MD. Because of the computation of the lifetimes using energy autocorrelation functions, the dissipative vs non-dissipative effects of Umklapp vs normal processes, respectively, are also preserved.

The effects of statistics on the heat capacity and the corresponding effects on thermal conductivity can be made apparent by considering the changes in predicted values as the heat capacity is evaluated using equipartition (A1, A3, A5) or Bose-Einstein statistics (A2, A4,

Compound	Temperature	A1 $\tau_{MD}\ C_{EQ}$	A2 $\tau_{MD}\ C_{BE}$	A3 $\tau_{BE}\ C_{EQ}$	A4 $\tau_{BE}\ C_{BE}$
MgO	500K	29.4	27.0	35.5	32.8
MgO	750K	16.3	15.6	20.9	20.2
MgO	1000K	10.4	10.2	14.7	14.4
PbTe	100K	11.2	10.7	13.0	12.4
PbTe	150K	7.0	6.8	7.9	7.7
PbTe	300K	3.1	3.1	3.4	3.4

Compound	Temperature	A5 $\tau_{EQ}\ C_{EQ}$	A6 $\tau_{EQ}\ C_{BE}$	A7 GK
MgO	500K	27.1	25.2	32.6 (2.1)
MgO	750K	17.4	16.8	19.6 (0.5)
MgO	1000K	12.6	12.4	14.1 (0.7)
PbTe	100K	10.2	9.8	10.4 (0.8)
PbTe	150K	6.6	6.5	6.5 (0.6)
PbTe	300K	3.0	3.0	3.2 (0.2)

Table 3.1: Computed thermal conductivity of MgO and PbTe using different expressions for lifetimes (τ) and heat capacities (C). All thermal conductivity values are in W/mK. The lifetimes τ_{MD}'s are obtained from MD simulations according to Equation 2.55, τ_{BE}'s are obtained from BTE according to phonons in a Bose Einstein distribution, whereas τ_{EQ}'s are obtained from BTE according to phonon population obeying equipartition. All BTE calculations include three- and four-phonon processes. The heat capacities C_{EQ} and C_{BE} correspond to those obtained from equipartition and Bose-Einstein statistics, respectively, as shown in Fig. 2.3. Finally, the thermal conductivity obtained from Green-Kubo (GK) is listed. The different approximations are labeled A1 to A7 in the first row.

A6), when the treatment of the lifetimes is held constant. Since classical heat capacities are consistently higher, and especially so at low temperatures, than Bose-Einstein heat capacities, the thermal conductivity values are also higher in A1, A3, and A5 than in A2, A4, and A6, respectively. The difference decreases with increasing temperature as expected. Moreover, we find that using BE heat capacities with MD lifetimes (A2) worsens rather than improves the agreement with the BTE-ALD results (A4). In agreement with Ref.[91], BE treatment of heat capacities together with MD lifetimes is ruled out as a possible quantum correction for classical MD simulations of thermal conductivity.

As mentioned above, phonon occupations also directly affect scattering rates calculated from three- and four-phonon scattering processes. This effect is apparent from a comparison between A4 and A6. It is seen that changing the occupation numbers to those corresponding

to equipartition (A6) rather than the Bose-Einstein distribution (A4), without changing the heat capacity, changes the thermal conductivity significantly (up to 24%). Note also, that the effect of statistics on scattering rates is significantly larger than the effects of statistics on heat capacities. For example, the differences between A5 and A6 is smaller than those between A4 and A6.

Attempting to remove the effects of statistics, a comparison can be made between BTE and MD approaches by comparing the results of BTE with equipartition (A5) to the Green-Kubo values (A7). Here, one finds that the agreement is reasonable with MgO and excellent with PbTe. We note, however, that the relaxation time approximation in BTE is not strictly valid when equipartition is enforced in phonon populations.

Interestingly, substituting MD lifetimes as well as heat capacities evaluated with equipartition into the BTE expression (A1) results in thermal conductivity values which are significantly different from those obtained from the Green Kubo expression (A7). The difference is likely due to the single-mode approximation used in the BTE approach. This highlights the fact that apart from treatments of lifetimes and heat capacities, the summation according to phonon modes in and of itself introduces a difference between BTE and MD methods for computing thermal conductivity.

3.4 Conclusions

In conclusion, in this chapter we have presented a detailed comparison between molecular dynamics (MD) and Boltzmann Transport Equation using anharmonic lattice dynamics (BTE-ALD) approaches for the computation of thermal conductivity. Improvements in BTE-ALD such as the inclusion of fourth-order phonon scattering processes, and treatment of temperature-dependent phonon frequency shifts (phonon renormalization) were included. Issues regarding the proper treatment of statistics in MD simulations, namely classical equipartition rather than Maxwell Boltzmann, were addressed. Thermal conductivity values were found to agree well between BTE-ALD and Green-Kubo (GK) MD, but a detailed anal-

ysis showed that such agreements are introduced by cancellations of different errors. By substituting lifetimes derived from energy-energy autocorrelation function from MD simulations into the BTE expression, we determined the effects of higher-than-4th-order phonon processes, the effects of statistics via the lifetimes and heat capacities, and the effects of single-mode relaxation time approximation itself, to the calculation of thermal conductivity. Significantly, we find that the effects of statistics on thermal conductivity is primarily due to effects on scattering rates. We also find that a full substitution of MD lifetimes and heat capacities in the BTE expression fails to reproduce GK results, indicating a significant effect of single-mode relaxation time treatment on thermal conductivity. One significant lesson from this comparison is that for integrated properties such as transport coefficients, apparent agreement may mask fundamental physical differences, thus caution is advised in the interpretation of the results.

CHAPTER 4

THERMAL TRANSPORT IN NANO-POROUS SILICON BRIDGES

4.1 Thermal Transport in Nano-porous Silicon Bridges

We now turn to the discussion of the thermal conductivity of a nanostructured material: nanoporous Si. Controlling nanoscale thermal transport via phonon engineering is a promising path for novel thermal management in electronic devices and high performance thermoelectrics[102]. The conversion efficiency of a thermoelectric device is controlled by the figure of merit of the material, $zT = \sigma S^2 T/\kappa$, where T is the temperature, σ the electrical conductivity, S the Seebeck coefficient and κ the thermal conductivity. The thermal conductivity is the sum of the electronic thermal conductivity and of the lattice thermal conductivity. An efficient thermoelectric material possesses a large Seebeck coefficient and electrical conductivity, while having a low thermal conductivity.

Usually, materials with nanometer feature sizes show unique thermal transport properties compared to the original bulk material. Nanostructured materials can in principle be designed to have significantly reduced thermal conductivity, at the price of a slightly reduced electrical conductivity. This has been demonstrated both experimentally and theoretically in various nanomaterials such as superlattices[103,104] and nanowires[105–107]. An alternative path to reduce thermal conductivity is the use of ultrathin silicon containing periodic arrangement of nanopores in a two-dimensional lattice of pores with a sub-100 nm period[108–113].

In recent years, nanoporous thin films have attracted great interest due to their potential applications not only in thermoelectric devices[114], but also as sensors and for nanoscale thermal insulation. The creation of reproducible samples with a defect free lattice of nanopores and a feature size of a few tens of nanometers has been made possible by recent progress in nanoscale manufacturing, lithography and block copolymer directed self-assembly.[115]

The mechanism for unusually low κ of nanoporous thin films is still under debate and it

remains an open question. Here we report calculations of the thermal conductivity of Si bridges of up to 37.5 nm, using the GK method and empirical potentials. Previous theoretical work[116,117] suggests that disorder at the surfaces of the pores may play an important role in reducing the group velocity, the mean free paths and the lifetimes of phonons, thus reducing the thermal conductivity, similar to what happens in silicon nanowires with disordered surfaces[105].

Previous computational works could only study samples with a feature size in the range of a few nm. In these nanostructures, phonons frequently interact with the boundaries, i.e. the surface of the pores, and phonon-surface scattering processes strongly reduce heat conduction. Generally speaking, when the wavelength of a phonon is shorter than the surface roughness, the phonon loses coherence and scatter diffusely. When this is the dominant scattering process, the thermal conductivity can be shown to be inversely proportional to the surface-to-volume ratio of the structure and approximately proportional to the limiting dimension of the structure[118].

On the experimental side, there are data available for porous silicon bridges with a regular lattice of pore with various porosity and a periodic length ranging from approx 1000 to 60 nm[113,119–121] and one study of a sample with a period of 34 nm[109]. Those length-scale are much higher than the one studied computationally using MD thus far.

Here, we have studied the room temperature thermal conductivity of Silicon thin films with two-dimensional hexagonal lattice of pores with periods between 7.5 and 37.5 nm and porosity between 20% and 40%. The porosity is in the range that is typical for the block copolymer directed self-assembly fabrication process, and the range of periods nicely bridge the gap between previously available MD results and available experimental studies.

4.2   Sample creation

The physical samples were created by our collaborators in Prof. Nealey's group at the University of Chicago. A detailed description of the fabrication process will be found in an

upcoming publication; here we summarize the main steps, shown schematically in fig. 4.2. A block copolymer film[122] is deposited and annealed on a pre-patterned single crystal wafer containing an intermediate layer of SiO_2 and a top layer of Silicon. During annealing, the block copolymer will self-assemble in a regular pattern[115]. A sequence of photo-lithographic and chemical techniques are then used to etch the holes in the Silicon layer and to remove a portion of the SiO_2 layer, leaving a porous silicon bridge of a height of 100 nm suspended in air, with a lattice period (called pitch) of 37.5 nm and a porosity of approximately 33%. During this sequence of processes, three pads of Aluminum are deposed at the center of the bridge and near the start and end of the bridge. These Aluminum pads are necessary for the measurement of the thermal conductivity using either Time-domain[25] or Frequency-domain[26] thermo-reflectance.
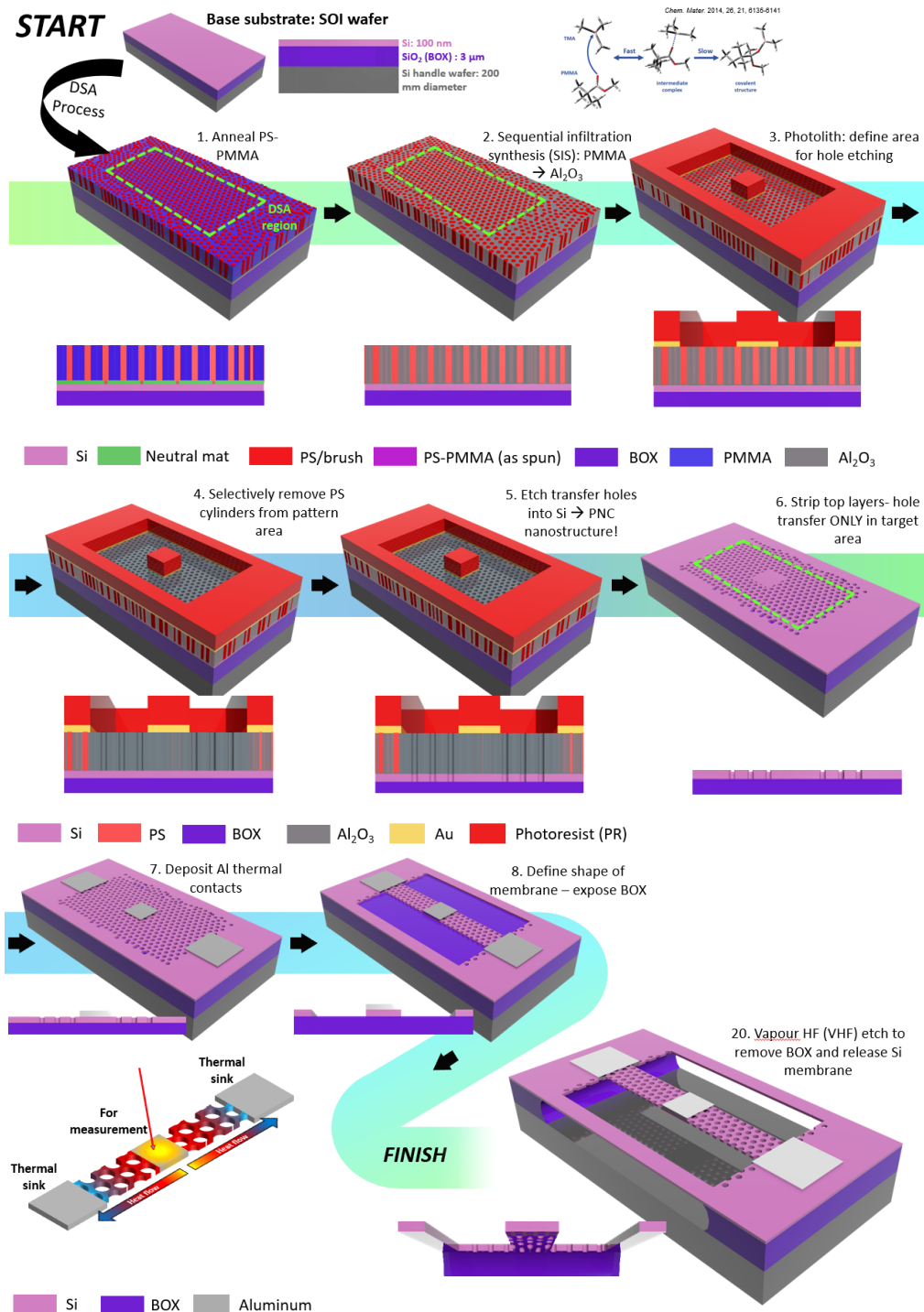
Figure 4.1: Fabrication steps of the porous silicon bridges. See text for description. Image courtesy of Elizabeth Michiko Ashley.

4.3   Method

All simulations were performed using LAMMPS[123] and the Tersoff potential[124,125], previously used to study thermal properties of nanowires[78] in the presence of oxidation. To understand the effect of oxidation on the thermal conductivity of porous Si bridges we compared systems containing only Silicon and samples in which the surface of the pores was oxidized.

The non-oxidized samples were prepared by carving the pores from a crystalline sample of pure Si to obtain the desired pitch and pore diameter, followed by a coordinate minimization and a short equilibration to let the Si surface reconstruct. The samples with oxidized pore surfaces were created by removing a Si annulus with a width of 0.5 nm of Silicon from the interior surface of the pore and substituting it with a layer of amorphous SiO_2 of the same volume, in order to keep the porosity and the pitch of the system unchanged. The amorphous layer was obtained from a bulk amorphous SiO_2 prepared by melting crystalline SiO_2 at 5300K, followed by annealing at a cooling rate of 1.6 K/ps. The sample was kept at a pressure of 1 atm during the annealing, resulting in a final density of 2.25 g/cm^3, close to the experimental density of amorphous silica. After the addition of the amorphous layer to the pure Silicon matrix, the whole system was kept at 900K for 1 ns and slowly cooled to 300K to let the exposed surface of the amorphous layer relax and the amorphous SiO_2 layer adhere to the Silicon lattice.

The thermal conductivity was calculated using the Green-Kubo method. Since it is not possible to simulate bridges of 100nm thickness, we used periodic boundary conditions and normalized the thermal conductivity by the ratio of the bulk thermal conductivity and the thermal conductivity of a non-porous silicon bridge 100 nm thick. In the case of pristine porous silicon bridges, we calculated the heat current autocorrelation function with a timestep of 1 fs, a sampling rate of 2 fs for 10 n using 8 replicas, for a total of 80 ns at each combination of pitch and porosity.
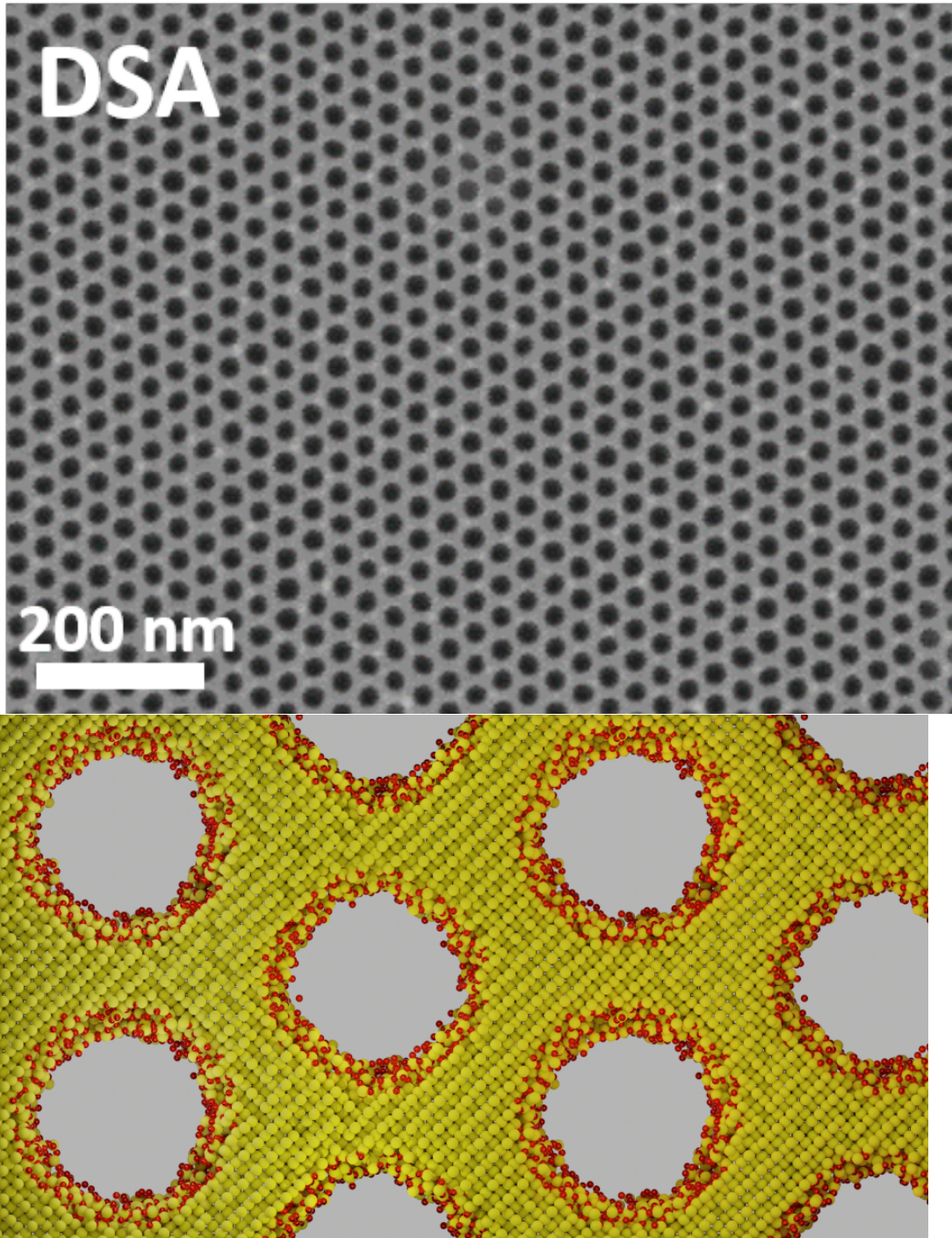
Figure 4.2: SEM image of a real sample and of a snapshot from our simulations. Silicon atoms are in yellow, Oxygen atoms in red. Top image courtesy of Elizabeth M. Ashley.

4.4   Molecular Dynamics Results

In figure 4.5 we present our results for the in-plane thermal conductivity of porous Silicon bridges in the absence of oxidation as a function of pitch and porosity. This material is anisotropic, and we can expect the thermal conductivity in the cross-plane direction to be different from that in the in-plane direction. Indeed, we found that in our simulations the cross-plane thermal conductivity is around twice as large as the one in-plane.. To our knowledge, only the in-plane thermal conductivity has been measured, so in what follows we limit our discussion to this component. We explored three porosities (20%, 33% and 40%) and three pitch sizes (7.5, 22.5 and 37.5 nm) for a total of nine combinations, to capture the range of experimentally feasible porosities and pitches. For a 40% porosity and a 37.5 nm pitch, we observe a thermal conductivity of 3.3 ± 0.3 W/mK, compared to the experimental thermal conductivity of $4.8 - 5.3$ W/mK at the same pitch and 42% porosity[126].

Our results are summarized in Table 4.5. As expected, the thermal conductivity increases with increasing pitch and with decreasing porosity. In Fig. 4.5 we present the same data, as a function of the diameter of the pores and of the porosity. The pore diameter d_p is:

$$d_p = \frac{\sqrt{2}\sqrt[4]{3}}{\sqrt{\pi}} \, p\sqrt{\phi} \tag{4.1}$$

Here d_p is the pore diameter, p is the pitch and ϕ is the porosity. We find that the Prasher model properly fits our data, with the exception of the higher porosity samples, where the thermal conductivity is underestimated at low pitch and overestimated when the pitch is longer than approximately 30 nm. In Figure 4.6 we show our data as a function of the neck size, defined as:

$$n = p - d_p \tag{4.2}$$

The neck size is the minimum length of solid material between pores. Previous works[112,113,118,120] have showed that the thermal conductivity presents a clear trend as a function of the neck size, with a less pronounced dependence on the other parameters, such as pitch or porosity.

This trend has been demonstrated experimentally for $n >\approx 15$, and our results extend this trend down to 2.5 nm. Some authors[118] claimed that the thermal conductivity should be only a function of neck size when it is smaller than 100 nm, a distance comparable to the mean free path of phonons in bulk silicon. However our simulations and model show that the thermal conductivity is not completely determined by the neck size. Another apparent trend, often discussed in the literature[112,113,116] is the dependence of the thermal conductivity on the surface-to-volume ratio. We show our results in Fig. 4.7. As already noted in experiments[118,127] and in simulations[128,129], we find that the thermal conductivity sharply decreases as a function of the surface-to-volume ratio, due to the increased phonon scattering at the surface of the pores.

We also computed the thermal conductivity of the porous silicon bridge in the presence of surface oxidation. In this case we only studied samples with a 33% porosity so far. We observe a large, approximately 4 fold reduction in the thermal conductivity of the sample with the 7.5 nm pitch, but little to no change in the sample with a 37.5 nm pitch. The large decrease we observed can be justified by observing that (1) the sample with the smaller pitch contains a larger percentage of amorphous silica , compared to Si; (2) the layer of amorphous silica reduces the fraction of the neck composed of pure silicon by approx. 40% in the smallest sample, but only by approx. 7% in the 37.5-nm-pitch sample.

Amorphous SiO_2 has a much lower thermal conductivity than Silicon (2.7 and 146 W/mK, respectively), which partly explain the reduction in thermal conductivity after oxidation. Moreover, the addition of the amorphous silica layer increases the amount of phonon scattering at the pore surface, because of the different material and because of the increase in the surface area available for surface-phonon scattering.

Finally, we suspect the addition of the amorphous silica layer reduces the group velocity of long-wavelength acoustic phonons, due to the different elastic properties of silica and silicon. Since long-wavelength phonons are important contributors to the overall thermal conductivity, a reduction in their group velocity would greatly reduce the thermal conductivity. It is

reasonable to assume that the reduction in group velocity following oxidation would be more pronounced in the sample with the smaller pitch.

4.5 Models

When the mean free path of phonons is comparable to the pore size and the pitch, effective-medium models fail in their prediction of the thermal conductivity of nanoporous materials. In theory, the Boltzmann transport equation, complemented by the Allen-Feldman theory of thermal transport, could be used instead. However, solving the BTE in such a complex network of pores, with such a large elementary cell, is impractical. Monte Carlo ray tracing transmission models[130], based on an approximate solution of the BTE, overestimate the thermal conductivity of porous Silicon bridges once the pitch is smaller than 500 nanometers[131]. As an alternative, Prasher[132] proposed an approximate model for predicting the thermal conductivity of phonons in two-dimensional nanoporous materials made from aligned cylindrical pores, which turns out to agree rather well with the results of our MD simulations. The model captures the size effects due to the interplay between phonon mean path, pore diameter and the pitch and reduces to the effective-medium models for macroporous materials. The full derivation of the model can be found in[132]. The final equation expresses the thermal conductivity of the nanoporous material as a function of two transport properties of the bulk material and two geometric properties of the nanoporous sample: the thermal conductivity κ_0 and the mean free path l of the phonons in the original bulk material; the porosity ϕ and the diameter of the pores d_p in the porous sample.

$$\kappa(\phi, d_p, l) = \frac{\kappa_0}{\frac{(1+\phi)}{(1-\phi)} + \frac{1}{q(d_p, \phi, l)\, F(\phi, d_p)}} \tag{4.3}$$

The so called view factor F is given by:

$$F(\phi, d_p) = 1 - \frac{d_p}{L}\left(\frac{\pi}{2} - \left(\sin^{-1}(d_p/L) + \sqrt{(L/d_p)^2 - 1} - L/d_p\right)\right)$$

And the rescaled lengths d and L are:

$$q = \frac{3d_p}{8l}\sqrt{\frac{\pi}{\phi}} \qquad L = d_p\sqrt{\frac{\pi}{4\phi}}$$

The Prasher model does not take into account the reduction in thermal conductivity due to the finite thickness of the silicon bridge. Other models, e.g.[133] incorporate this effect, but we found they overestimated the thermal conductivity for large pore diameters and in the limit of zero porosity. Therefore, we used the simpler Prasher model, with the thermal conductivity of a suspended silicon bridge with zero porosity (72 W/mK) in place of the bulk thermal conductivity. Finally, the Prasher model contains the parameter l, the bulk phonon mean free path. We used our data to fit l, finding $l = 67$ nm ± 1.
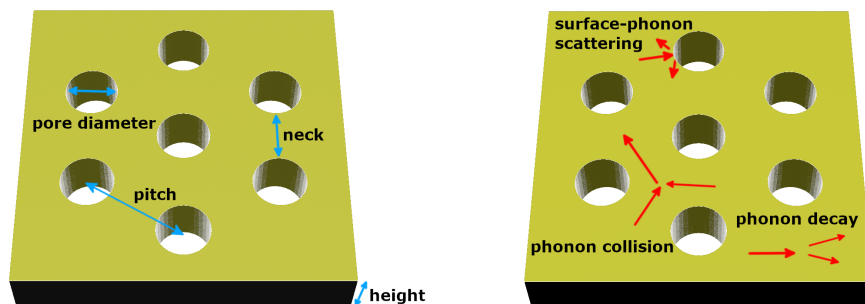
Figure 4.3: **Left**: nomenclature used to describe the geometrical properties of the sample. Not to scale. **Right**: schematic representation of the main phonon scattering processes in a nanoporous silicon bridge.
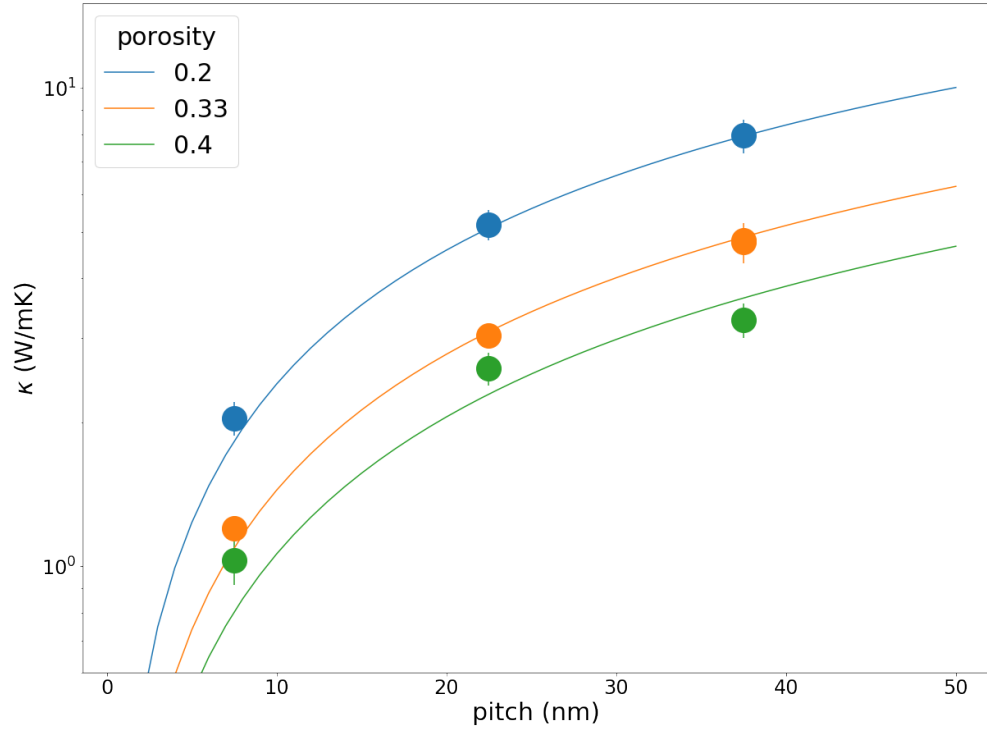
Figure 4.4: Thermal conductivity of nanoporous silicon bridge as a function of pitch and porosity. When not visible, the error bars are occluded by the markers. Porosity is calculated as a fraction of the total volume. Solid lines are calculated from a single fit of Eq. 4.3 using all data.

Porosity (%)	Pitch (nm)	κ (W/mK)	$\delta\kappa$ (W/mK)
20	7.5	2.0	0.2
20	22.5	5.2	0.4
20	37.5	7.9	0.6
33	7.5	1.20	0.05
33	22.5	3.0	0.1
33	37.5	4.8	0.5
40	7.5	1.0	0.1
40	22.5	2.6	0.2
40	37.5	3.3	0.3

Table 4.1: Thermal conductivity of porous silicon bridges, 100 nm thick, as a function of porosity and pitch.
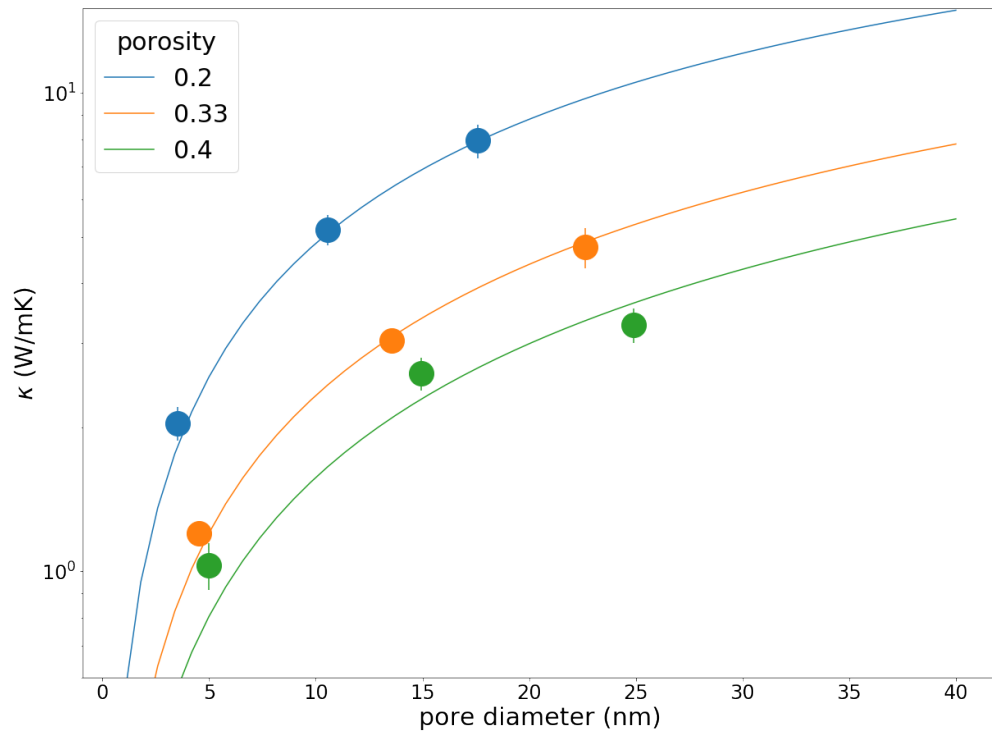
Figure 4.5: Thermal conductivity of nanoporous silicon bridge as a function of the diameter of the pores and porosity. The pore diameter is calculated using Eq. 4.1. Solid lines are calculated from a single fit of Eq. 4.3 using all data.
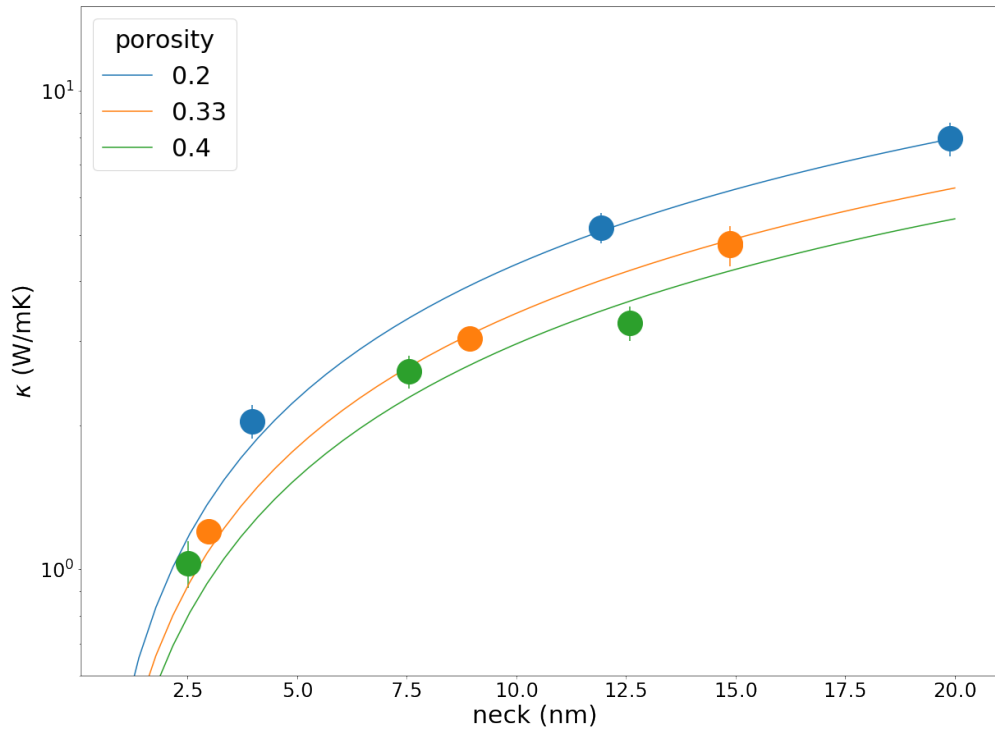
Figure 4.6: Thermal conductivity of nanoporous silicon bridge as a function of neck length and porosity. The neck length is calculated using Eq. 4.2. Solid lines are calculated from a single fit of Eq. 4.3 using all data.
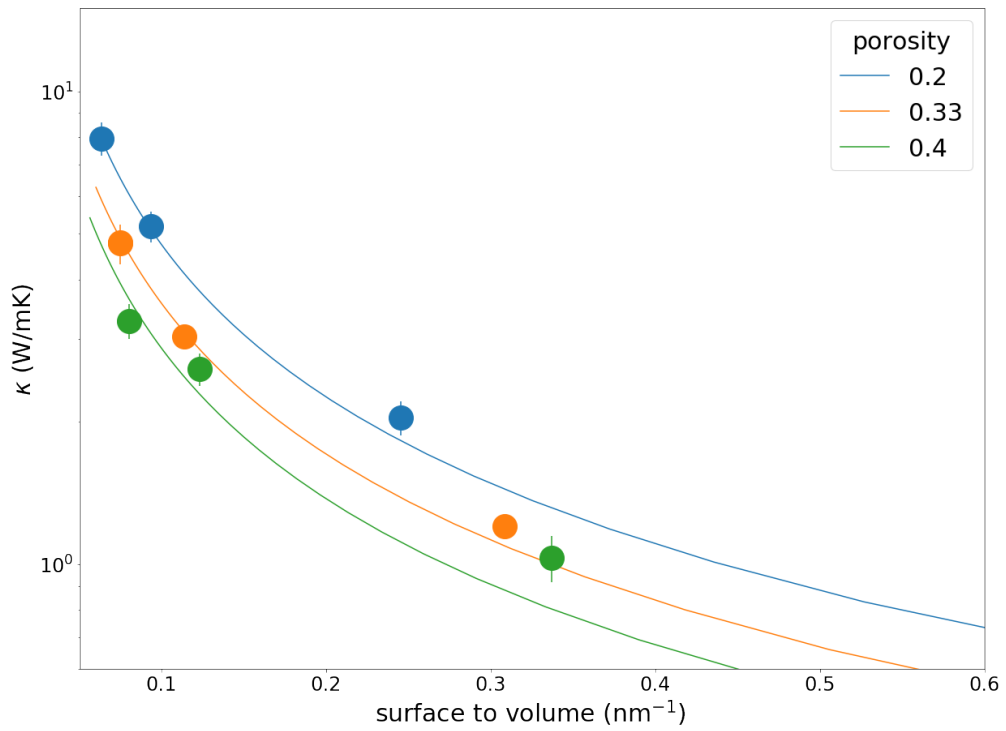
Figure 4.7: Thermal conductivity of nanoporous silicon bridge as a function of the surface-to-volume and porosity. Solid lines are calculated from a single fit of Eq. 4.3 using all data.

4.6   Conclusions

Thermal management in modern electronic devices and high performance thermoelectrics increasingly require a more sophisticated control of thermal transport at the nanoscale. Understanding thermal transport at the nanoscale is a necessary step in gaining this control.

Porous silicon bridges with a regular lattice of pores promise immediate interesting applications as sensors, thermal barrier and potentially thermoelectric devices. However, they also represent an ideal test-bed for different theories and models for heat transport. They combine a relatively simple and highly regular geometrical pattern with complex thermal transport properties. These transport properties derive from the interplay between intrinsic phonons-phonon scattering, phonon-surface scattering and change in phonon properties due to porosity and to the reduced length scale. Recent advancement in manufacture makes it possible to build these devices with a pitch in the same length-scale of the phonon mean path in the bulk.

In our study, we investigated the thermal conductivity of nanoporous silicon bridges with a pitch in the 7.5 to 37.5 nm range, and with porosity in the 20% - 40% range. These simulations bridged the gap between previous simulations and available experiments, and provide results in the range where the interplay previously described is most complex. We found good agreement with experiments at 37.5 nm, 40% porosity and we found that the oxidation of pores (addition of a SiO_2 layer at the surfaces of pores) does not change the conductivity within our error bars for systems at a 37.5 nm pitch, while it substantially reduces the thermal conductivity of systems at smaller pitches.

While more work is needed, and it is in progress, our simulations provided a microscopic understanding of thermal transport in these materials, the relation between morphology and thermal conductivity, including the effect of porous oxidation at smaller pitch. We found that our simulation results are correctly fitted by the Prasher model, which we hope will assist in engineering of the thermal conductivity of these and similar devices.

CHAPTER 5

APPROACH TO EQUILIBRIUM METHOD

5.1   Introduction

In previous chapters we have described BTE based methods to obtain the thermal conductivity and also methods based on Equilibrium MD. In addition to equilibrium methods, non equilibrium ones have also been developed. Non Equilibrium (NEMD) methods compute the thermal conductivity in the steady state from the response of the system to a perturbation. They can be classified according to the nature of the perturbation: in the so called direct method[134] it is a temperature gradient causing a heat flux[135]; in reverse NEMD, also known as the Muller-Plathe approach, the constant heat flux acts as the perturbation[136]. The "approach to equilibrium" methods compose the third class of MD based methods. In these approaches, the thermal conductivity is computed from the time response of the system to an instantaneous perturbation. This perturbation can be in the form of a square[137,138] or sinusoidal temperature profile[27]. Ab initio non equilibrium MD calculations have been reported, using homogeneous NEMD[72] and hence involving the explicit calculations of heat currents or using the method of Ref.[139,140], which faces serious convergence challenges as a function of simulation time.

5.2   Sinusoidal Approach to Equilibrium for Solids

Addressing the need for an efficient and general quantum simulation framework for thermal properties of materials, we developed a method to simulate heat transport from first principles, which can be employed for predictive calculations of complex, homogeneous and heterogeneous solids. We generalized the approach to equilibrium molecular dynamics[137,138] (AEMD) method by implementing sinusoidal temperature gradients, thus avoiding temperature discontinuities. We call this approach sinusoidal AEMD (SAEMD). We show below that

SAEMD can be applied in a straightforward manner to the calculation of thermal conductivity using density functional theory (DFT). This approach only requires the computation of MD trajectories and atomic forces, with no additional calculation of energy derivatives, e.g. force constants, energy densities or direct calculations of currents. The precision of the method can be systematically increased by parallel computations on multiple replicas, thus requiring much shorter sequential simulation times than ordinary non equilibrium techniques. Below we briefly describe our formulation and we discuss results obtained with classical potentials and first principles molecular dynamics. We then compare our findings to experimental data, previous simulations and our own calculations using the GK method.

Within the AEMD approach the average temperature of a solid is arbitrarily changed by a discontinuous temperature profile; subsequently the way equilibrium is approached after applying the perturbation is monitored, by carrying out an NVE (constant number of particles N, volume V and energy E) simulation. In particular the temporal decay of T towards an equilibrium value is used to calculate the thermal conductivity. AEMD has been successfully applied to crystalline and amorphous solids and alloys[138], as well as to 2D and nanostructured materials such as nanocrystalline silicon[138], Si-Ge alloy nanocomposites[141], graphene[142,143], graphane,[144] and porous Si nanowires[145]. In the absence of net convective transport, and assuming that $\alpha = \kappa/\rho c_v$ is a constant, the heat equation is given by:

$$\frac{\partial T}{\partial t} = \alpha \frac{\partial^2 T}{\partial t^2} \tag{5.1}$$

The SAEMD method is based on the comparison of the solution of the heat equation obtained analytically and that computed by using molecular dynamics simulations. For a periodic system represented by a given slab, the analytical solution of the heat equation:

$$T(z,t) = A_0 + \sum_n [A_n \cos(\gamma_n z) + B_n \sin(\gamma_n z)] \, e^{-\gamma_n^2 \alpha t} \tag{5.2}$$

where $T(z, t=0)$ is the initial condition; $\gamma = \frac{2\pi n}{L_z}$ and the A_n and B_n coefficients are:

$$A_n = \frac{2}{L_z} \int_0^{L_z} \cos(\gamma_n z) T(z,0) \mathrm{d}z \tag{5.3}$$

$$B_n = \frac{2}{L_z} \int_0^{L_z} \sin(\gamma_n z) T(z,0) \mathrm{d}z \tag{5.4}$$

In our calculations we used local Nose-Hoover thermostats to impose the initial sinusoidal, and hence continuous, temperature profile T(z,0), which is position dependent:

$$T(z,0) = T_0 + \frac{\Delta T_0}{2} \sin\left(\frac{2\pi z}{L_z}\right) \tag{5.5}$$

where z is the direction of heat propagation, T_0 is the average temperature and ΔT_0 is the peak to peak difference in the temperature applied to a slab chosen to represent the system of interest, and periodically repeated in x,y,z. The solution of the heat equation can be expressed as:

$$T(z,t) = A_0 + \sum_n B_n \sin(\gamma_n z) e^{\gamma_n^2 \alpha t} \tag{5.6}$$

where the A_n and B_n coefficients are all zero but

$$A_0 = T_0 \tag{5.7}$$

$$B_1 = \frac{\Delta T_0}{2} \tag{5.8}$$

$$T(z,t) = T_0 + \frac{\Delta T_0}{2} \sin\left(\frac{2\pi z}{L_z}\right) e^{-\gamma_1^2 \alpha t} \tag{5.9}$$

where $\gamma_1 = 2\pi/L_z$ and the thermal diffusivity $\alpha = \kappa/\rho c_v$, where ρ is the density and c_v is the volumetric heat capacity. The difference between the average temperature of the left and right side of the slab representing the periodic system is given by:

69

$$\Delta T(t) = T_1(t) - T_2(t) \tag{5.10}$$

$$T_1(t) = \frac{2}{L_z} \int_0^{\frac{L_z}{2}} T(z,t)\mathrm{d}z \tag{5.11}$$

$$T_2(t) = \frac{2}{L_z} \int_{\frac{L_z}{2}}^{L_z} T(z,t)\mathrm{d}z \tag{5.12}$$

The difference between the average temperature of the two sides of the system subject to the sinusoidal T profile is

$$\Delta T(t) = \frac{2}{L_z} \int_0^{\frac{L_z}{2}} T(z,t)\,\mathrm{d}z - \frac{2}{L_z} \int_{\frac{L_z}{2}}^{L_z} T(z,t)\,\mathrm{d}z \tag{5.13}$$

$$= \frac{2\Delta T_0}{\pi} e^{-\gamma_1^2 \alpha t} \tag{5.14}$$

In order to solve the same equation numerically, by using molecular dynamics, we proceed in three steps:

1. We start with atoms in crystalline positions, and carry out an NVT simulation, with a thermostat (Nose-Hoover) set at the target temperature.

2. We then subdivide the simulation cell representing the systems into slabs and assign a different T to each slab, determined by the position dependent temperature profile (perturbation) we wish to impose on the sample.

3. We monitor the evolution of the system under the imposed perturbation toward equilibrium, by carrying out an NVE simulation.

During step (3) the instantaneous average temperatures T_1 and T_2 of the two halves of the simulation cell are computed from the kinetic energy of the atoms. The difference $\Delta T(t)$ is then computed as $T_1(t) - T_2(t)$. Finally, the known analytical solution of the heat equation is used to fit the solution obtained via MD, i.e. t $\Delta T(t)$ is fitted using equation
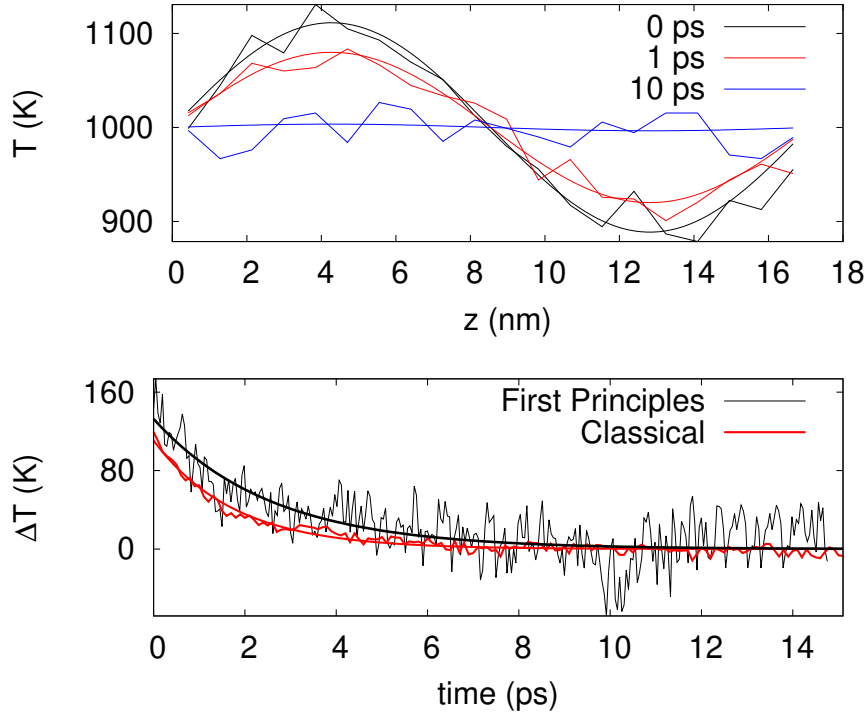
Figure 5.1: Top: Temperature profile along the heat transport direction z, averaged over 30 samples, for a classical molecular dynamics run performed at 1000K for MgO. Smooth, continuous solid lines represent analytical solutions of the heat equation. Note the rapid decay of the sinusoidal profile to zero over 10 ps (blue line). Bottom: Difference in the average temperature ($\Delta T(t)$) between the hot and cold side of a periodic slab representing MgO, as a function of time, during a molecular dynamics run at constant volume and energy, carried out after the application of a sinusoidal temperature profile (Eq.1). We show first principles results (black line) obtained for a slab with 960 atoms at 500K, and classical result (red line) for the same size slab, but averaged over 30 samples. Solid lines are the results of a fit to Eq. 5.14. The rate of decay of ΔT is proportional to the thermal conductivity.

(5.14). From this fit the best estimate of the thermal diffusion α is obtained and then the thermal conductivity is computed.

At variance with the original AEMD approach, only the fundamental mode is present when using sinusoidal gradients, and thus no higher harmonics in the Fourier expansion of the temperature profile need be considered. The thermal diffusivity α is obtained by fitting the expression of ΔT in Eq. 5.14, as obtained during an NVE run. As an example, in Fig. 5.1 (top panel) we show the instantaneous temperature averaged over 30 samples of crystalline MgO (1280 atom samples) at the beginning and during the NVE simulation, along with the

analytical solution of the heat equation (continuous lines). In the lower panel of Fig 5.1 we show the difference in temperature as a function of time and the fitted function (Eq. 5.14) used to calculate the thermal diffusivity. In addition, separate calculations to compute the heat capacity as a function of T were carried out and the thermal conductivity is readily obtained from $\kappa = \alpha \rho c_v$, where ρ is the known density of the system (set by choosing the volume V).

We note that within the SAEMD approach, typical simulation times to reach equilibrium are shorter by about 2 order of magnitude, compared to those required by the NEMD method, thus making the technique presented here amenable to use with first principles approaches, i.e. density functional theory (see SI for a detailed comparison between techniques). Simulations times are also one order of magnitude shorter than in the GK approach. When using a GK formulation, the simulation time scale is determined by the time required to reduce the noise in the tail of the heat current autocorrelation function; in NEMD it is the time needed to reach a stationary state between the cold and hot ends of the system, plus the additional time required to obtain an accurate temperature gradient that determine the length of thermal conductivity simulations. These simulation times are of course system dependent, but they can be estimated to be, in general,[78,146] two order of magnitude longer than the time required to reach equilibrium within SAEMD.

The efficiency of the SAEMD method relies on the ability to reduce statistical errors in the determination of the thermal conductivity, which arise due to the intrinsic noise in the temperature profile of a finite system. Given the transient nature of our MD simulations, statistical errors may not be improved by increasing the simulation time once the temperature difference (Eq. 5.14) vanishes. Instead, one may carry out multiple, parallel runs and then average the results obtained for the various replicas. However, care must be exercised in the way averages are performed and direct averaging over values of α from different replicas may lead to inaccurate or even wrong results. In the absence of noise, the difference in temperature $\Delta T(t)$ decays to zero at a rate proportional to the thermal diffusivity α. In the presence of

72

noise this rate is modified: the probability distribution of α is an asymmetrical function (we report an example in the SI) and its average value increases as a function of increasing noise. The value of α obtained by averaging over different replicas may thus result to be greatly overestimated. In our calculations we averaged over instantaneous temperature differences $\Delta T(t)$ obtained for several replicas, and then we performed a single fit to the average value to compute the diffusivity.

5.3   Finite Size Effects

A well known challenge in realistic predictions of thermal conductivity of solids is posed by finite size effects. Within the AEMD approach, check of convergence is required with respect to the lateral section of the sample used, as well as the length of the system in the direction of heat transport, so as to ensure that all relevant phonon mean free paths are correctly taken into account. In our calculations, finite size scaling was performed by computing κ for several samples of length L, as illustrated in Fig. 6.1 and Fig. 6.2. The extrapolation implicitly assumes that there exists a certain sample length after which only one dominant phonon mean free path is present. Under the additional assumption of validity of the Matthiessen's rule one obtains[147]

$$\kappa(L) = \kappa_\infty / (1 + \frac{\lambda}{L}) \tag{5.15}$$

This equation appears to properly fit results obtained at finite sizes within both NEMD, for which it was developed, and AEMD, although it is not fully justified for the latter (in particular the assumption of an additional scattering term due to the thermostat, valid within NEMD, is not justified). Very recently a new fitting equation for the AEMD method has been proposed[148], not based on the Matthiessen's rule, where it is assumed that acoustic phonons, whose lifetime is proportional to $1/\omega^2$, are the major contributors to heat transport.

$$\kappa(L) = \kappa_\infty (1 - \sqrt{\Lambda/L}) \tag{5.16}$$

We show in Fig. 6.1 that eq. 5.15 and 5.16 yield nearly the same results for the case of MgO, for large sizes, in spite of having been derived under different assumptions.

5.4   Use of independent replicas

Here we discuss the averaging technique used in our work by presenting one case in details. We calculated the thermal conductivity of MgO at 500K with a cell of length of 6 nm, using two different lateral sections of 0.5 and 2.5 nm. We calculated the thermal conductivity using 100 simulations for each lateral section and we performed averages in two different ways: (i) we computed the thermal conductivity for each of the 100 simulations from the temperature difference, and we then calculated the average value of the thermal conductivity. (ii) We first averaged the temperature profile, as a function of time, over all the simulations. We then used this average to compute the average conductivity. We show in Fig.5.2 and in Table 5.4 how the use of method (i) may result in a serious overestimation of the computed value in the case of simulations with strong noise.

In order to further illustrate our point about averaging noisy data, we report in table 5.4 the results for a simple model where the temperature decay is given by exp(-t/κ), with κ chosen equal to 4 (a.u.), plus a white Gaussian noise. We studied two cases of low and high noise. By using this simple model we are able to show that the procedure suggested by the reviewer would result in an overestimate of κ in the case of high noise, while our procedure gives the correct results in both case of low and high noise.

Method	Low noise Fig 5.3 (right panel)	High noise Fig 5.3 (right panel)
(i) Fit each $\Delta T(t)$; find average κ	Computed $\kappa = 4.0009$	Computed $\kappa = 4.889$
(ii) Average $\Delta T(t)$; find κ from $\langle \Delta T \rangle$	Computed $\kappa = 3.997$	Computed $\kappa = 3.939$

Table 5.1: Results for a simple model where the temperature decay is given by $e^{-t/\kappa}$, with κ chosen equal to 4 (a.u.), plus a white gaussian noise. We studied two cases of low and high noise. By using this model, we show that method (i) would overestimate κ in the case of high noise, while method (ii) gives the correct result in both low and high noise.
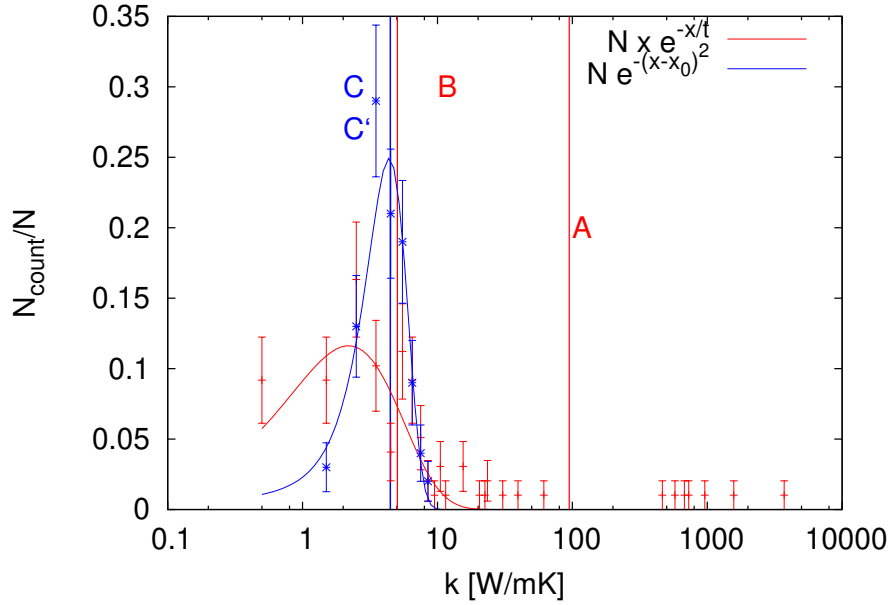
Figure 5.2: Probability distribution and average value of the thermal conductivity calculated over 100 replicas for two systems of the same length but containing 96 (red) or 2400 (blue) atoms. Solid lines are drawn as a guide to the eye; N,x_0 and t are fitting parameters. Solid vertical lines are: (A) the thermal conductivity calculated as the average of the thermal conductivity obtained from each simulation, for the system with 96 atoms; (B) the thermal conductivity calculated from the average of the temperature difference for the system with 96 atoms. Note the difference with the A value; (C) and (C') thermal conductivity calculated as the average of the thermal conductivity obtained from each simulation and from the average of the temperature difference. Note the similarity between the values of C and C'. The simulations for the system with 2400 atoms exhibit clearly much less noise than those for the 96 atom system.
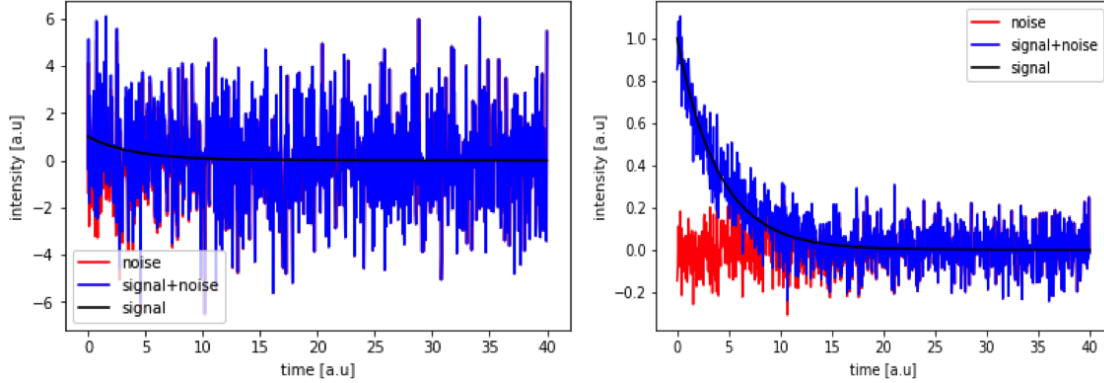
Figure 5.3: Low (right) and high (left) noise applied to the signal $e^{-t/\kappa}$. The results for the computed decay are show in Table 5.4.

Type of simulation and lateral cross section	κ [W/mK]	$\Delta\kappa$ [W/mK]
NEMD 2X2	39.7	2.7
NEMD 3X3	34.7	1.1
NEMD 4X4	30.9	1.3
AEMD 2X2	40	0.4
SAEMD 2X2	43	1
SAEMD 4X4	32	1.6

Table 5.2: Extrapolated values of the thermal conductivity (second column) and their statistical error (third column) obtained using non-equilibrium MD (NEMD), approach to equilibrium MD (AEMD) and Sinusoidal approach to equilibrium MD (SAEMD), with lateral sections of 2x2, 3x3 and 4x4 MgO unit cells.

5.5   Sinusoidal Approach to Equilibrium for Fluids

In its original formulation presented in the previous section, the SAEMD approach cannot be applied to liquids[27]. Below we present a method based on approach to equilibrium MD simulations, which retains all the advantages of SAEMD, and can straightforwardly be applied to liquids.

5.6   Method

The general equation of heat transport is:

$$\rho c_p \Big(\frac{\partial T}{\partial t} + (\vec{v} \cdot \nabla T) \Big) = \kappa \nabla^2 T + \dot{q}$$

where v is the net mass velocity of atoms and molecules in the material, κ is the thermal conductivity; q is the external heat flux, T is the temperature, c_p is the heat capacity at constant pressure (P) and ρ is the density of the system. We compute the thermal conductivity of a condensed system (either fluid or solid) from its response to a perturbation. The latter is expressed as a non-homogeneous constant temperature profile, which is maintained by a thermostat during a MD simulation. The response of the system results into a non-homogeneous constant energy flux proportional to the Laplacian of the temperature and to the thermal conductivity. The temperature profile is defined as:

$$T(x,y,z) = T_0 + \frac{\Delta T}{8} \Big(\Big(1 - \cos\Big(\frac{2\pi x}{L}\Big) \Big) \Big(1 - \cos\Big(\frac{2\pi y}{L}\Big) \Big) \Big(1 - \cos\Big(\frac{2\pi z}{L}\Big) \Big) - \frac{1}{2} \Big) \quad (5.17)$$

where L is the length of the simulation cell chosen to represent the system, and ΔT is the difference between the maximum and the minimum temperature within the MD cell. When the thermal conductivity is computed using the approach to equilibrium method in a

transient regime (SAEMD method), $q = 0$ and the velocity term v is set to zero, to obtain:

$$\frac{\partial T}{\partial t} = \frac{\kappa}{\rho c_p} \nabla^2 T$$

In the case of solids, setting $v=0$ is justified, since the atoms are not free to move. However, in the case of liquids, atoms or molecules diffuse and the velocity term cannot be set to zero. Hence to generalize the SAEMD method to liquids, here we solve the heat equation in the presence of a perturbation *in the steady state*, where:

$$0 = \kappa \nabla^2 T + \dot{q}$$

We partition the MD cell into two regions, an interior one defined as the sphere centered in the middle of the cell and containing half of its volume; the second region (exterior) contains the remaining half of the cell. This partition is not unique, and the system may be divided into more than two regions, if needed. Our choice is motivated by the simplicity of the configuration.

After the perturbation is applied, we monitor how much energy the thermostat is providing to the interior region, and how much energy the thermostat removes from the exterior one. This continuous energy exchange is necessary to maintain the temperature difference between the two regions in the steady state and the sum of the energy provided and removed must be zero when a steady state is reached. The time derivative of the difference of the energy exchanged ($\dot{q}$) is the key quantity necessary for the calculation of the thermal conductivity.

Under the assumption that the thermal conductivity (κ) of the system is isotropic and independent on position, we can obtain κ from the ratio of $\dot{q}$ and the difference in the integrals over the two regions (internal and external) of the Laplacian of the temperature.

We note that, depending on the size of the chosen simulation cell and hence on the temperature gradient created in the cell, the temperature profile obtained during the simulation
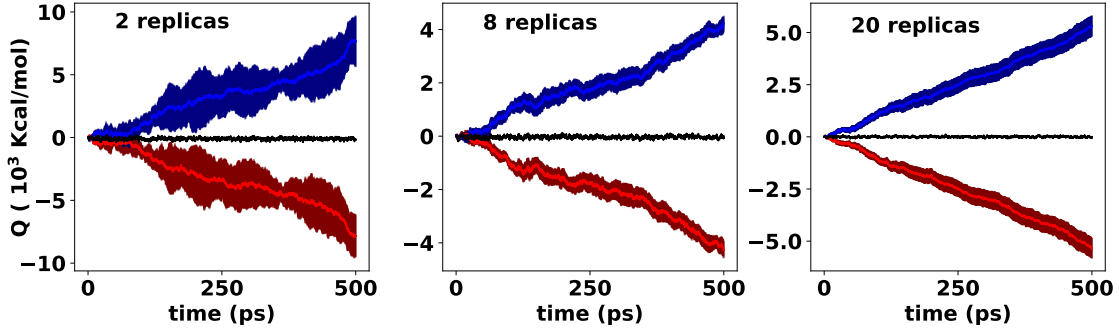
Figure 5.4: Energy ($Q(t)$) exchanged between the interior(blue) and exterior (red) partitions of a simulation cell as a function of time, in a close to equilibrium molecular dynamics simulation (SAEMD) of liquid water under pressure (see text). The three panels show results obtained by averaging over 2, 8 and 20 replicas. The shaded regions represent the uncertainty in the estimation of $Q(t)$. The black line is the total energy exchanged between the two regions.

may turn out not to be identical to the one specified by the perturbation imposed. Hence in order to correct for this behavior, in our calculations we multiplied the difference in the integrals of Eq. 5.18 by the ratio between the expected temperature difference in the two regions and the one observed during the simulation.

$$\dot{q} = \frac{\partial(q_{\text{int}} - q_{\text{ext}})}{\partial t} = \kappa \left(\int_{\text{int}} \nabla^2 T - \int_{\text{ext}} \nabla^2 T \right) \tag{5.18}$$

In order to obtain statistically meaningful data, in our simulations we averaged over results obtained from multiple independent replicas. We show the importance of using multiple replicas in figure 5.4, where we report q_{int}, q_{ext} and their estimated error as a function of the simulation time using 2, 8 and 20 replicas for the calculations of the thermal conductivity of water under pressure, using cells with 512 water molecules at P = 9.7 GPa and T=1000K.

5.7   Finite Size Effects

The thermal conductivity computed from MD simulations using periodic boundary conditions (pbc) suffers from finite size effects for two reasons: (i) the cell size (and hence number

of atoms) chosen to represent the heat propagation in the system is of course finite; this approximation is present in all methods and it is the only source of finite size effects in equilibrium simulations based on GK; (ii) the need to keep different parts of the system at different T, to monitor the flow of energy; this approximation affects the NEMD and SAEMD approaches, but clearly not GK.

Due to the presence of finite size effects, an extrapolation of simulation results obtained for different cell sizes is usually necessary to obtain a converged value of κ. In solids, the extrapolation of simulation results as a function of size is obtained using models for phonon mean free paths[147,148]. In liquids, simple models of vibrational modes and their mean free paths are not available. We derived approximate formulae to extrapolate the results of our simulations for water based on the phenomenological model of heat transport presented in reference[149], where the contribution of all pairs of molecules up to a distance r to the heat flux (J) is written as:

$$J(r) = C\rho_N^2 \int_0^r \dot{Q}(r')g(r')r'^3 r'^{-m} dr' \ . \tag{5.19}$$

Here g is the radial distribution function of the liquid, C is a constant, ρ_N is the number density; r^{-m} accounts for the fact that the interaction between molecules is a many-body interaction, rather than pairwise. For liquid water in the range 300-600K, using MD simulations Ohara[149] found that $\dot{Q}(r') = Q_0/r^3$ for $r > 0.7nm$ and that a value of $m = 2$ best describes the heat flux of water at ambient conditions. In the limit of large r, $g(r) = 1$ and we rewrite equation 5.19 as:

$$J(L) = J_\infty - C' \int_L^\infty Q_0 r^{-2} dr = J_\infty (1 - \lambda/L) \tag{5.20}$$

where J_∞ is the extrapolated value of the heat current for $L \to \infty$ and C and λ are constants. In our simulations we observed that the auto-correlation function $(A(\tau))$ of the current $J(t)$ can be expressed as a product of an oscillating function independent on size

$(f(\tau))$ multiplied by size dependent intensities and we approximate it as $A(\tau) \simeq (J_L)^2 \cdot f(\tau)$.
Hence the thermal conductivity is proportional to $(J_L)^2$ and using Eq. 5.20 we write κ as:

$$\kappa(L) = C'' J_\infty (1 - \lambda/L)^2 = \kappa_\infty (1 - \lambda/L)^2 \tag{5.21}$$

where κ_∞ is the extrapolated value of the thermal conductivity for $L \to \infty$ and C'' is a constant. As we will see below, using Eq. 5.21 we can accurately fit our simulation results at ambient conditions and thus determine the value of κ_∞. However, as expected Eq. 5.21 is not appropriate to fit our high T and P results, since the value $m = 2$ used in Eq. 5.20 and Eq. 5.21 was derived for water at ambient conditions. Hence, we rewrote Eq. 5.21 by treating m as a fitting parameter and we found that a value of $m = 4$ appeared to fit our simulation results relatively well. For $m = 4$ Eq. 5.21 becomes to leading order in $1/L$:

$$\kappa(L) = \kappa_\infty - (\lambda/L)^3 \tag{5.22}$$

and as shown below it fits accurately our high pressure results. We note that Eq. 5.21 is equal to leading order in L to an equation[150] derived from hydrodynamics arguments and used to describe finite size effects in the calculations of the diffusivity of fluids, including water.

CHAPTER 6

FIRST-PRINCIPLES SIMULATIONS OF HEAT TRANSPORT

Introduction

In this chapter we use the method discussed in Chapter 5 by computing the thermal conductivity of solids using classical and *ab initio* molecular dynamics at close to equilibrium conditions. We discuss results for a representative oxide, MgO, at different temperatures and for ordered and nanostructured morphologies, showing the performance of the method in different conditions.

6.1   Computational details

For MgO, we used the potential described in Ref.[92]; This potential is of the Buckingham-Coulomb type. The MgO potential was shown[92] to predict experimental lattice constant, thermal expansion and thermal conductivity reasonably well in the 300K-1500K range. First principles calculations were carried out using a 40 Rydberg cutoff, the pseudopotentials O_HSCV_PBE-1.0.xml for Oxygen and a modified version of 12-Mg.GGA.fhi for Magnesium.

6.2   Lateral section

We carried out a detailed study of our results as a function of the lateral section. Results are shown in Table 5.4 for both SAEMD and NEMD, using classical potentials. The 2x2 lateral section used in our first principles calculations turned out to be smaller than the one required to fully converge the value of the thermal conductivity, as indicated by the results obtained with classical potentials. Unfortunately carrying out simulations with a (4x4) lateral section is prohibitively expensive at present, hence we used a correction factor (α_c) for the (2x2) first principles results, namely we multiplied them by $\alpha_c = 32/43 \approx 0.744$; α_c equals the

ratio $[\kappa$ SAEMD (4x4)]/$[\kappa$ SAEMD (2x2)] of values of κ computed in SAEMD simulations with classical potentials.

6.3   Results

We now turn to the presentation of our results for a representative solid, MgO, chosen because of the availability of experimental data and of several results from other studies to compare with. We first describe classical and first principles simulations of bulk MgO and compare data obtained with discontinuous and sinusoidal temperature gradients, as well as using the GK method. We then show that the SAEMD approach is general and it can be used also for systems containing nano-grains, and not only for ordered bulk systems.

All classical simulations were carried out using LAMMPS[123], with a Buckingham Coulomb potential shown[92] to describe reasonably well density, thermal expansion and thermal conductivity of crystalline MgO. First principles MD simulations were carried out by coupling the LAMMPS and Qbox[151] codes within a client-server strategy. The former was used to integrate the equation of motion and to apply the local thermostats, and the latter to compute DFT forces on atoms at each time step and to carry out the NVE part of the simulation. Alternatively, a position dependent thermostat can be implemented directly in the first principles MD engine. The time needed to generate the temperature profile, the approximate time necessary to reach equilibrium and the number of replicas necessary to obtain a $\approx 10\%$ statistical error were the same for classical and first principles simulations. A timestep of 1 fs was adopted in our MD simulations and a constant lateral section of 2X2 elementary cells was chosen, as a reasonable compromise between computational cost and accuracy. However finite size scaling tests for the lateral sections conducted with classical potentials showed this cross section not to be fully converged. Unfortunately carrying out first principles simulations with a (4X4) lateral section is prohibitively expensive at present, hence we used a correction factor α_c for the first principles result, namely we multiplied them by $\alpha_c = 32/43 \approx 0.744$; α_c equals the ratio $[\kappa\_SAEMD(4X4)]/[\kappa\_SAEMD(2X2)]$ of

values of κ computed in SAEMD simulations with classical potentials. We realize this is an approximation, which could be eliminated using larger simulation cells in the future. Green Kubo simulations with classical potentials were performed with the same 1 fs timestep in the NVE ensemble and using a cubic supercell. We averaged the thermal conductivity over multiple replicas and tested convergence with respect to both time and number of atoms. We analyzed the differences in the extrapolation of AEMD results obtained with classical potentials, as a function of the maximum length (L_{MAX}) of the simulation cell in the direction of heat transport. The values of κ_∞ obtained with L_{MAX} larger than or equal to 13 nm are similar to each other, within reasonable error bars (between 1 and 2 W/mK). These results thus justify our extrapolation of the first principles results, which have been obtained by including cells with L_{MAX} up to 13 nm.

Results obtained with classical potentials are shown in Fig. 6.1 for bulk MgO at 500 and 1000K. We found very good agreement between AEMD and SAEMD calculations at both temperatures, as well as between different extrapolation methods. For the thermal conductivity of MgO at 500 K computed with SAEMD we obtained 32 ± 1.6 W/mK using Eq. 5.15 and a 4x4 lateral section, against a value of 32 ± 1 using GK and an experimental value of 34.1[2]. Note that, as pointed out in Ref.[148], Eq. 5.16 is appropriate to describe thermal conductivity extrapolations at large sizes, but not at short sample lengths. We thus used a minimal length of ≈ 20 nm when fitting Eq. 5.16. First principles MD results are presented in the top panel of Fig. 6.1. We carried out calculations for crystalline samples with 192, 256, 384, 512 and 960 atoms using gradient corrected exchange correlation functionals (the Perdew-Burke-Ernzerhof (PBE)[152] functional;). We averaged the temperature difference over 12, 8, 4, 4 and 1 replicas for 3, 4, 5, 7 and 15 ps, respectively, for the five chosen sizes, with a 10% target error. The results and their extrapolation using Eq. 5.15 (50 W/mK) turned out to be consistent with those of classical calculations using the same lateral section (43 W/mK for SAEMD simulations), giving a bulk thermal conductivity of 37 W/mK for MgO at 500K, when corrected to account for the difference between 4x4 and 2x2 results
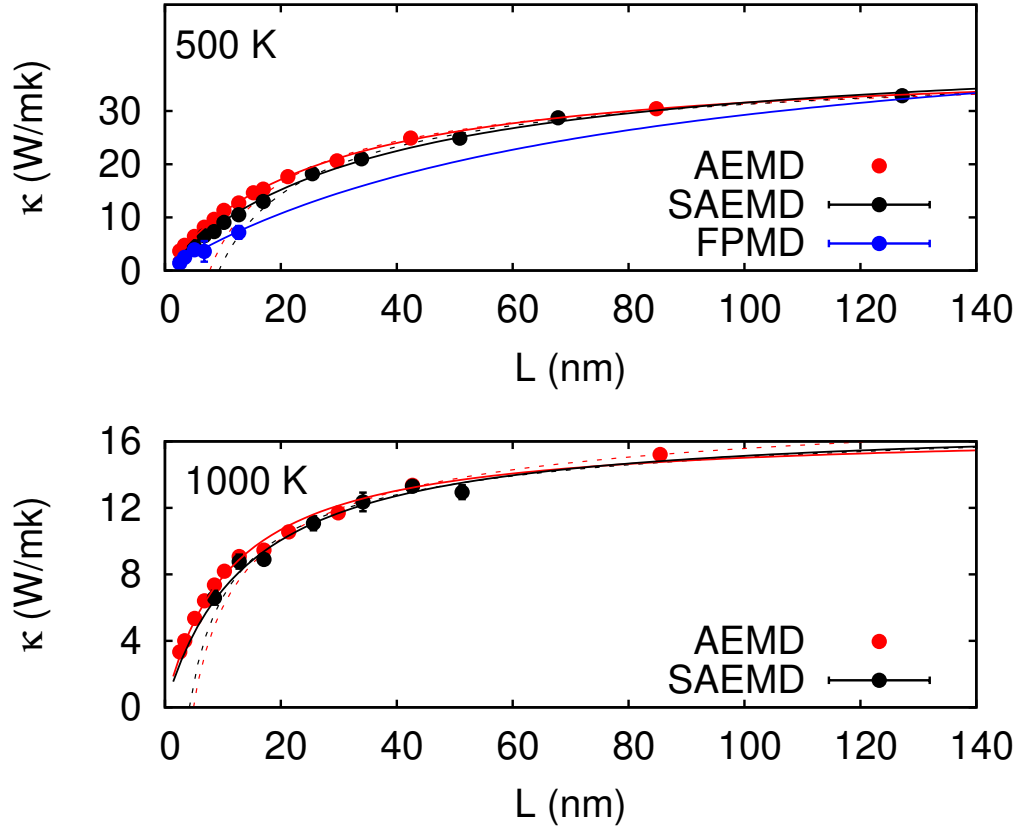
Figure 6.1: Thermal conductivity (κ) of crystalline MgO computed at 500 (top panel) and 1000K (lower panel), as a function of the length of the periodic slab (L), using approach to equilibrium molecular dynamics (AEMD, red curves), sinusoidal approach to equilibrium (SAEMD, black curves) and classical potentials. We compare results obtained with the two methods using classical potentials and we show (blue curve) first principles results obtained with the SAEMD method. Solid and dotted lines represent a fit to Eq. 5.15, and 5.16, respectively.

($\alpha_c = 0.744$). We emphasize that the main finding of our first principles MD simulations is the demonstration of their feasibility, opening the way to studying heat transport in complex and realistic systems, without the need to compute any heat current or energy densities. It is also reassuring to find good agreement with experiment and classical potentials and with previous simulations[1,2,92,140].
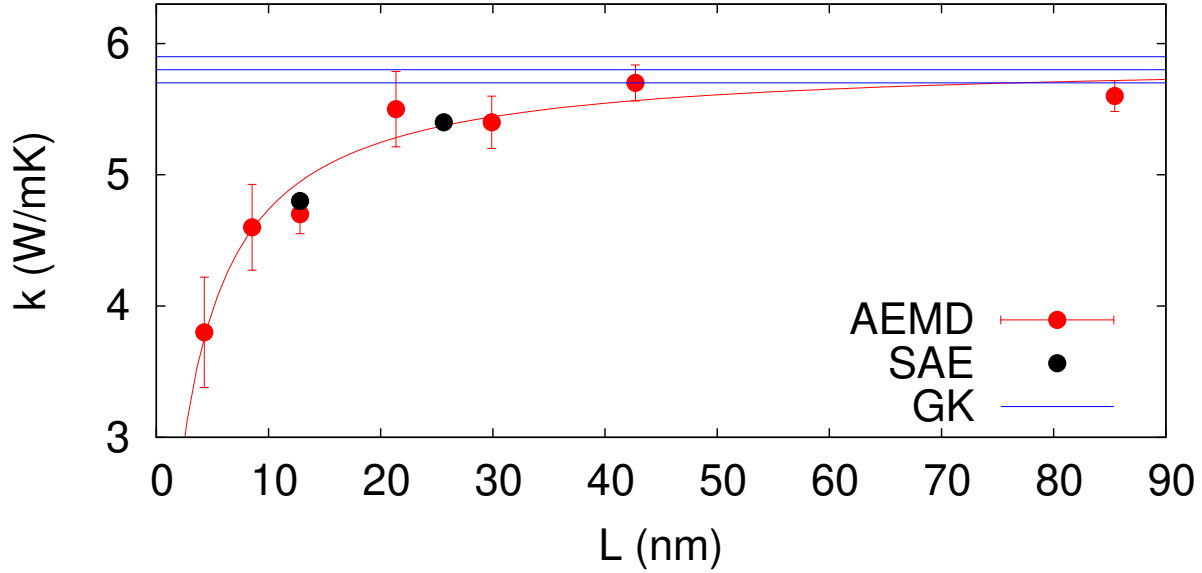
Figure 6.2: Thermal conductivity (κ) of a periodic slab representing nanocrystalline MgO, as a function of the slab length L, computed at 1000K using a classical potential. The average radius of nanocrystalline grains is 2 nm. We compare simulation results obtained with approach to equilibrium molecular dynamics (AEMD method, red dots), sinusoidal approach to equilibrium molecular dynamics (SAEMD, black dots) and equilibrium molecular dynamics using a Green Kubo (GK) formulation (blue lines). The blue lines represent the results of converged GK simulations as a function of size. Convergence was obtained for L ≈ 8nm with a cubic supercell; the top and bottom blue lines represent the population standard deviation of the samples used for GK calculations.

6.4   Nanocrystalline MgO

Finally, we tested the validity of the SAEMD approach for nanostructured MgO. In Fig. 6.2 we show the thermal conductivity of nanocrystalline MgO obtained using Green Kubo, AEMD and SAEMD methods. The grains were created by insertion of small crystalline seeds in random points of the molten phase, followed by grains growth. We averaged over multiple simulations in order to account for the random nature of grains in the samples, using classical potentials. We found again remarkable agreement between AEMD, SAEMD and GK calculations, indicating that the analytical solution of the heat equation is valid also at the nanoscale, at least for the 3D material investigated here. As expected, we also found a reduction of the thermal conductivity with respect to bulk MgO, by approximately

a factor of 3, for 2 nm grains at 1000K.

6.4.1 Data for nanocrystalline MgO

Temperature	radius NC	N_z	Atoms	Replicas	sim time	k
1000 K	2nm	30	≈ 36000	20	3 ns	6.1 ± 0.1
1000 K	2nm	60	143208	1	1 ns	5.8

Table 6.1: Green Kubo simulations for nanocrystalline (NC) MgO. In all tables simulation time only include the time used to calculate the thermal conductivity. The time taken to create the grains does not depend on the calculation method

Temperature	radius NC	Nz	Ny	Atoms	Replicas	sim time	k
1000K	2 nm	30	30	≈ 36000	20	200 ps	4.8
1000K	2 nm	60	30	≈ 72000	10	200 ps	5.4

Table 6.2: SAEMD simulations for NC MgO.

Temperature	NC radius	Nz	Ny	Atoms	Replicas	sim time	k
1000K	2 nm	10	20	≈ 8000	10	24 ps	3.8
1000K	2 nm	20	20	≈ 16000	10	34 ps	4.6
1000K	2 nm	30	20	≈ 24000	10	24 ps	4.7
1000K	2 nm	50	20	≈ 40000	5	44 ps	5.5
1000K	2 nm	70	20	≈ 56000	4	104 ps	5.4
1000K	2 nm	100	20	≈ 80000	4	154 ps	5.7
1000K	2 nm	200	20	≈ 160000	4	404 ps	5.6
1000	2 nm	∞					5.8 ± 0.1

Table 6.3: AEMD simulations for NC MgO.

6.5 Experimental data and results of previous simulations
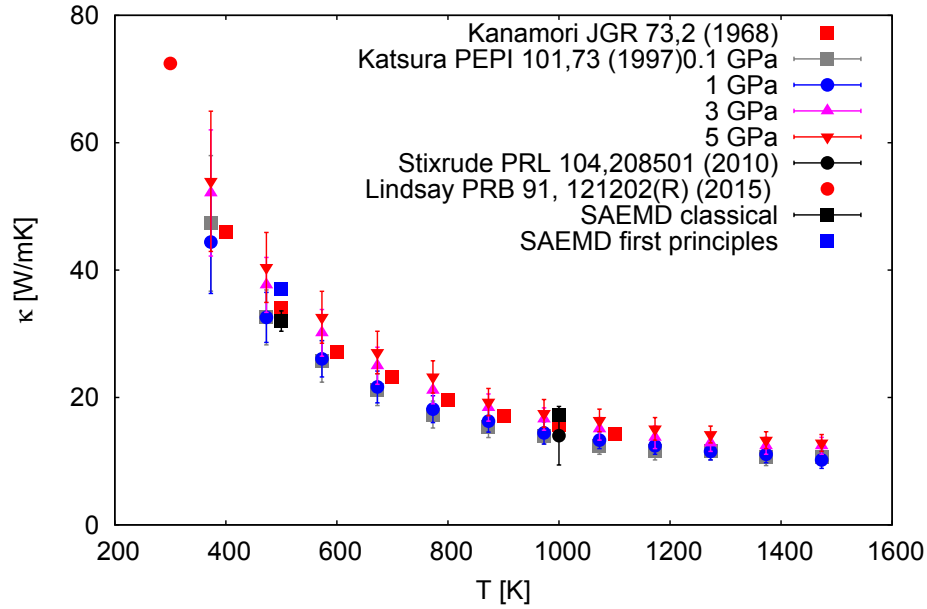
Figure 6.3: Experimental data and results of previous simulation. Results from SAEMD using classical MD are presented for the maximum lateral section available. Results from SAEMD using first principles MD use the correction factor α_c. Since Katsura[1] only published results for thermal diffusivity, we used the density and thermal capacity from Ref.[2] to calculate the thermal conductivity.

6.6 Green Kubo and Non-Equilibrium molecular dynamics simulations for bulk MgO

As a mean of validating our SAEMD results we also carried out GK and Non Equilibrium MD calculations of the thermal conductivity of crystalline MgO. In Figures 6.4, 6.5 and 6.6, and Tables 6.6, 6.6, 6.6 and 6.6 we show that there is almost a 2 orders of magnitude difference between SAEMD (or AEMD) simulation times and NEMD simulation times for the thermal conductivity of the same system (MgO at 500 K). We comment these results below, offering an explanation of why required NEMD simulation times are longer.

- In general, the time to reach a steady state in SAEMD and NEMD are similar, as suggested by the reviewer. In the NEMD method a heat current is induced inside the system, and the steady state is reached once the heat current has propagated through the entire system. The timescale of this process is roughly given by the length of the system squared divided by the heat diffusivity. Not unsurprisingly, this is the same timescale of the temperature profile evolution during the approach to equilibrium phase of SAEMD.

- When carrying out NEMD simulations, one computes the temperature gradient for each of the two sides of the slab (the hot and cold one). We found that, even when averaging over 4 replicas, 400 ps were needed to reach stable temperature gradients. The main reason why NEMD is much more disadvantageous than SAEMD in terms of simulation time is because calculations of temperature gradients are required, unlike in the SAEMD case. In order to have enough statistics to evaluate a reasonable gradient requires much longer simulation times than with SAEMD. This is also the reason why NEMD would not be applicable to first principles simulations at present. Time scales of the order of 500 ns are out of the questions even for rather small systems.

- For GK the comparison regarding first principles simulations is not straightforward as additional calculations of the energy density are required. One of the main points of

our work is to present a method to carry out calculations of the thermal conductivity by computing only positions and forces.
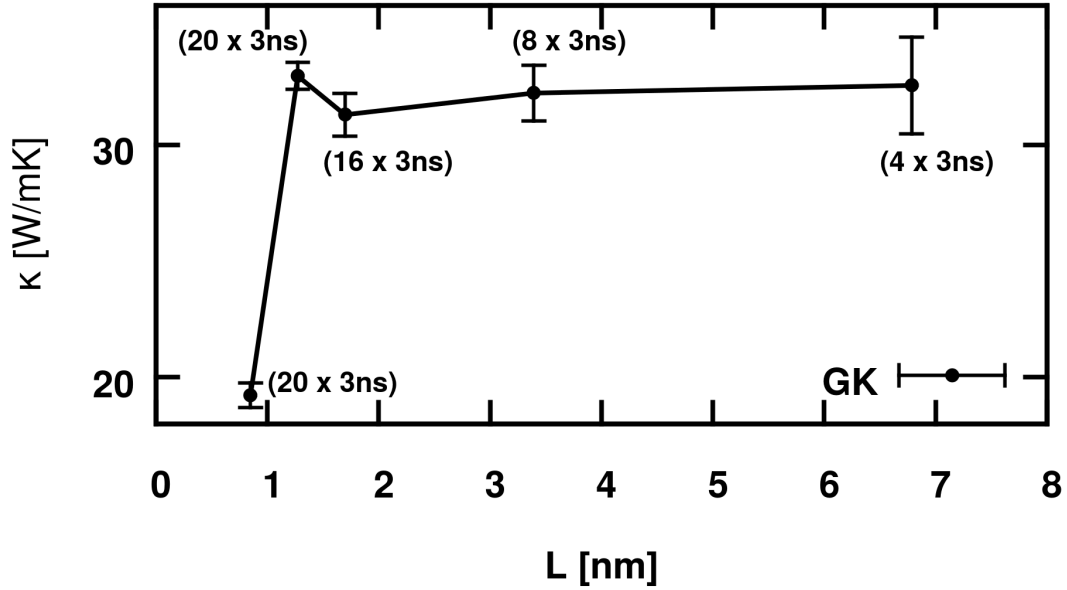
Figure 6.4: Green Kubo (GK) simulations of the thermal conductivity of MgO at 500 K; each of the simulations requires the calculation of an energy density and is performed on cubic cells of side L. The 5 points above correspond to 2^3, 3^3, 4^3, 8^3 and 16^3 cells (see table 6.1 for exact values of κ). *A posteriori* one can see that simulations with cells of size 4^3 (containing 512 atoms) appear to be converged. The simulation time required for that size cell was approximately 48 ns.
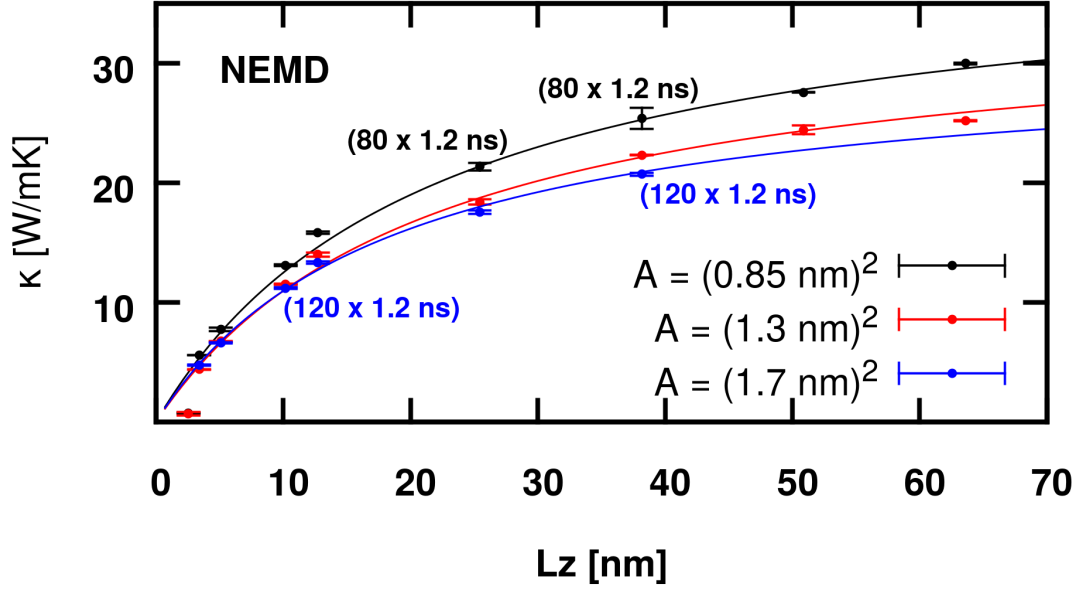
Figure 6.5: Non-equilibrium MD (NEMD) simulations of the thermal conductivity of MgO at 500 K; L_z denotes the direction of heat transport. Black, red and blue curves correspond to simulations carried out with lateral sections of (2x2), (3x3) and (4x4), respectively. The extrapolated values of κ considering all points in the figure are 40 ± 2.7, 34 ± 2.4 and 30 ± 1 W/mK, respectively. *A posteriori* we can determine that by omitting the last point from the fit (Lz = 63 nm), in (2x2) simulations we obtain a value of 40 ± 6. 0; in (3x3) simulations we obtain a value of 36.1 ± 5.5. In 4x4 simulations, we included only points up to Lz = 38. Note that the total time of the simulation of the largest size (similar to that of the smaller sizes) for 2x2 later sections is 96 ns. At least five points are necessary, hence the total time (encompassing different sizes) for the largest error bars shown in the figure is 480 ns.

Temperature	N_L	Atoms	Replicas	Sim time	k (W/mK)	total sim time (ns)
500 K	2	64	20	3 ns	19.2 ± 0.5	60
500 K	3	216	20	3 ns	33.0 ± 0.6	60
500 K	4	512	16	3 ns	31.3 ± 0.9	48
500 K	8	4096	8	3 ns	32.2 ± 1.2	24
500 K	16	32768	4	3 ns	32.6 ± 2.1	12
1000 K	4	512	8	3 ns	13.2 ± 0.7	
1000 K	8	4096	9	3 ns	14.1 ± 0.7	

Table 6.4: Simulation results for Green-Kubo calculations of the thermal conductivity of MgO. We used cubic systems for GK calculations. N_L is the number of elementary cells in each cartesian direction. There are 8 atoms for elementary cell. The error in the thermal conductivity, when available, is the standard deviation of the mean.

Classical NEMD simulations at 500K

2X2 cross section				
Nz	Atoms	Replicas	sim time [ns]	k [W/mK]
6	192	80	1.2	0.7
8	256	80	1.2	5.6
12	384	80	1.2	7.7
24	768	80	1.2	13.1
30	960	80	1.2	15.8
60	1920	80	1.2	21.4
90	2880	80	1.2	25.4
120	3840	80	1.2	27.6
150	4800	80	1.2	30

3X3 cross section				
Nz	Atoms	Replicas	sim time [ns]	k [W/mK]
6	432	100	1.2	0.7
8	576	100	1.2	4.4
12	864	100	1.2	6.7
24	1728	100	1.2	11.5
30	2160	100	1.2	14
60	4320	100	1.2	18.4
90	6480	100	1.2	22.3
120	8640	100	1.2	24.4
150	10800	100	1.2	25.2

4X4 cross section				
Nz	Atoms	Replicas	sim time [ns]	k [W/mK]
8	1024	120	1.2	4.8
12	1536	120	1.2	6.6
24	3072	120	1.2	11.2
30	3840	120	1.2	13.3
60	7680	120	1.2	17.6
90	11520	120	1.2	20.7

Table 6.5: Simulation results for NEMD calculations of the thermal conductivity of MgO at 500 K. The error in the asymptotic value of the thermal conductivity is the uncertainty in the fitting procedure. N_z denotes the number of elementary cells in the direction of heat transport. The extrapolated values of κ considering all points in the figure are 39.7 ± 2.7, 34.7 ± 1.1 and 30.9 ± 1.3 W/mK, respectively. A posteriori we can determine that by omitting the last point from the fit (Lz = 63 nm), in (2x2) simulations we obtain a value of 40 ± 6.0; in (3x3) simulations we obtain a value of 36.1 ± 5.5. In 4x4 simulations, we included only points up to Lz = 38. Note that the total time of the simulation of the largest size (similar to that of the smaller sizes) for 2x2 later sections is 96 ns. At least five points are necessary, hence the total time (encompassing different sizes) for the largest error bars shown in the figure is 480 ns.
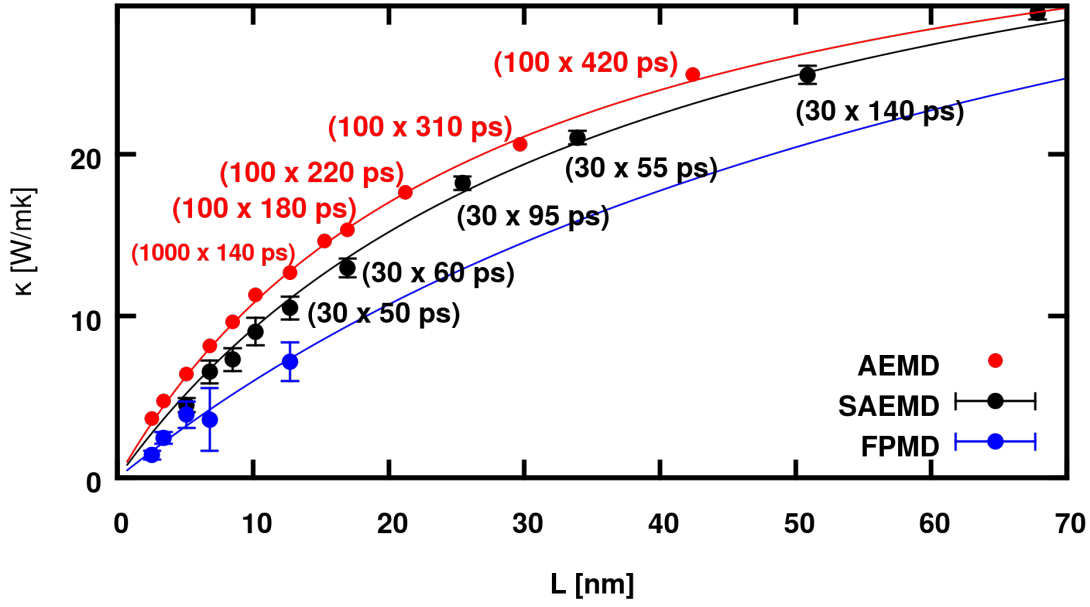
Figure 6.6: Close to equilibrium MD simulations of the thermal conductivity of MgO at 500 K; L_z denotes the direction of heat transport. We report SAEMD and AEMD results with classical potentials and first principles MD results using the SAEMD technique, labeled FPMD. The extrapolated values of κ considering all points in the figure are 40 ± 1.0 (AEMD), 43 ± 1.1 (SAEMD) and 50 (FPMD) W/mK, respectively. A posteriori we can determine that by omitting the last point from the fit in classical simulations we obtain values that differ by less than 5% with respect to the converged values. Note that the total time of the simulation to obtain error bars similar to the one considered in the NEMD simulations is 30X55X5 ps = 8250 ps = 8.25 ns to be compared with the 480 ns.

Classical SAEMD simulations for bulk MgO.

	2X2 cross section				
Temperature	Nz	Atoms	Replicas	sim time	k [W/mK]
500 K	12	384	300	10 ps	4.5
500 K	16	512	160	35 ps	6.5
500 K	20	640	64	30 ps	7.3
500 K	24	768	64	35 ps	9.0
500 K	30	960	30	50 ps	10.5
500 K	40	1280	30	60 ps	13.0
500 K	60	1920	30	95 ps	18.2
500 K	80	2560	30	55 ps	21.0
500 K	120	3840	30	140 ps	24.9
500 K	160	5120	30	140 ps	28.7
500 K	300	9600	5	420 ps	32.9
500 K	∞	eq. 5			43 $\pm$1.1
500 K	∞	eq. 6			45 $\pm$1
Temperature	Nz	Atoms	Replicas	sim time	k [W/mK]
1000 K	20	640	100	50 ps	6.5
1000 K	30	960	64	50 ps	8.8
1000 K	40	1280	30	80 ps	8.9
1000 K	60	1920	30	100 ps	11.1
1000 K	80	2560	100	140 ps	12.4
1000 K	100	3200	64	170 ps	13.3
1000 K	120	3840	24	220 ps	12.9
1000 K	∞	eq. 5			17.3 $\pm$0.9
1000 K	∞	eq. 6			19 $\pm$2

Table 6.6: Simulation results for SAEMD calculations of the thermal conductivity. We used a 2X2XN_z simulation cell. The error in the asymptotic value of the thermal conductivity is the uncertainty in the fitting procedure

Classical simulations
4X4 cross section

Temperature	Nz	Atoms	Replicas	sim time	k [W/mK]
500 K	6	768	60	60 ps	4.5
500 K	8	1024	60	60 ps	3.8
500 K	12	1536	60	60 ps	5.7
500 K	16	2048	60	60 ps	7.7
500 K	20	2560	60	60 ps	8.1
500 K	24	3072	60	60 ps	9.8
500 K	30	3840	60	60 ps	11.1
500 K	60	7680	60	60 ps	16.3
500 K	90	11520	60	60 ps	18.3
500 K	120	15360	60	60 ps	21.6
500 K	∞	eq. 5			32.2 ± 1.6

Table 6.7: Simulation results for SAEMD calculations of the thermal conductivity. We used a 4X4XN_z simulation cell. The error in the asymptotic value of the thermal conductivity is the uncertainty in the fitting procedure

First principles results

Temperature	Nz	Atoms	Replicas	sim time	k [W/mK]
500 K	6	192	12	3 ps	1.4
500 K	8	256	8	4 ps	2.5
500 K	12	384	4	5 ps	3.9
500 K	16	512	4	7 ps	3.6
500 K	30	960	1	15 ps	7.2
500 K	∞	eq. 5			50

Table 6.8: Simulation results for SAEMD calculations of the thermal conductivity for the first principles simulations. We used a 2X2XN_z simulation cell.

6.7 Conclusions

In summary, in this chapter we presented a first principles non equilibrium molecular dynamics approach for the calculations of the thermal conductivity of materials. The method is a variant of AEMD, utilizing simpler initial conditions and a fit to the analytic solution of the heat equation with just one Fourier coefficient. The method avoids the use of discontinuous temperature gradients, and it permits to employ noise reduction techniques, which in turn allow one to reduce the number of parallel replicas used in the calculation. Within SAEMD only atomic trajectories and forces are needed and no other calculation of energy densities, force constants or heat current are required, making the framework presented here amenable to calculations within density functional theory. Furthermore, slabs of different sizes may be equilibrated at the target temperature at the same time, thus allowing one to exploit the parallel architecture of modern high performance computers. All of these characteristics make the SAEMD method ideal to be used with first principles Hamiltonians, as demonstrated here for a representative oxide, MgO.

CHAPTER 7

ATOMISTIC SIMULATIONS OF THE THERMAL CONDUCTIVITY OF LIQUIDS

7.1   Introduction

Here we present an application of sinusoidal approach to equilibrium molecular dynamics (SAEMD) to compute the thermal conductivity of liquids. Similar to non-equilibrium molecular dynamics, and unlike equilibrium simulations based on the Green Kubo formalism, the method only requires the calculation of forces and total energies. The evaluation of heat fluxes and energy densities is not necessary, thus offering the promise of efficiently implementing first principles simulations based on density functional theory or deep molecular dynamics. As mentioned earlier, our approach is a generalization of SAEMD for solids, where the thermal conductivity is computed in the steady state, instead of a transient regime, thus properly taking into account diffusive terms in the heat equation.

As an example, we present results for liquid water at ambient conditions and under pressure, at conditions (1000K and 10 GPa) for which ab-initio simulations of the structural properties of the liquid have been recently reported[153]. We present results for liquid water at ambient conditions and under pressure and discuss simulation requirements to obtain converged values of the thermal conductivity as a function of size and simulation time.

Water is responsible for heat transfer in many physical, chemical and biological processes. It exhibits a number of anomalous properties, including high specific heat and, with the exception of liquid metals, the highest thermal conductivity of pure liquids at standard conditions[154]. While measurements of heat transport in water are available at room T and P, very few experiments[155] have been reported under extreme conditions, where the ability to predict thermal conductivity is thus particularly important.

7.2 Results

In this section we present our results for the thermal conductivity of water at ambient conditions (T = 300K, ρ = 1 g/cm^3) and under pressure (T= 1000K, ρ = 1.57 g/cm^3). Structural properties under pressure were recently investigated[153] with ab initio MD using the PBE functional[152], and we chose one snapshot from the trajectories reported in the ab initio study to start our simulations. Water at ambient conditions was described with the TIP4P-2005f force field[156]. This empirical potential turned out to be numerically unstable at high T and P; in particular, we found non physical dissociation events in our simulations. At high P we then used the SPCE-Fl force field[157], which describes the OH bonded interaction with a harmonic potential and by construction cannot lead to any dissociation. Note that we used flexible potentials to avoid spurious effects in the calculations of heat transfer brought about by the presence of constraints in MD simulations with rigid water molecules[158]. As discussed in the conclusions, it would be desirable to use more realistic force fields and ultimately conduct ab initio simulations; however as reported below, the time scales required for the simulations of heat transport in water make the use of ab initio MD prohibitive and point at the future use of machine-learned first principle potentials as a viable alternative. In our work we chose to use empirical potentials to demonstrate the accuracy and robustness of the method proposed here, as compared to GK simulations, and to test finite size scaling and the required simulation times.

We compare below (Fig. 7.1 and Fig. 7.2) results obtained with GK and SAEMD simulations. In the former case, for each replica we carried out simulations for 800000 steps (200 ps) under NVT conditions (initializing the calculation with different initial velocities in different replicas), followed by NVE simulations to collect data to compute the thermal conductivity. When discussing simulation time we only refer to this part of the simulation. For each cell size we used 8 replicas and 600 ps long simulations, except for the 13824 molecules cell, where we run 4 replicas.

The SAEMD simulations included 3 steps: (i) equilibration of the system at constant

temperature; (ii) application of a temperature perturbation; we carried out relatively long simulations of about 100 ps in this transient regime but several tests indicated that if needed, this time may be decreased by up to one order of magnitude, the exact simulation time depending on the system; (iii) collection of results to compute κ. As in the case of Green-Kubo simulations, we averaged over multiple independent replicas and when discussing simulation time we only refer to the final part of the simulation.
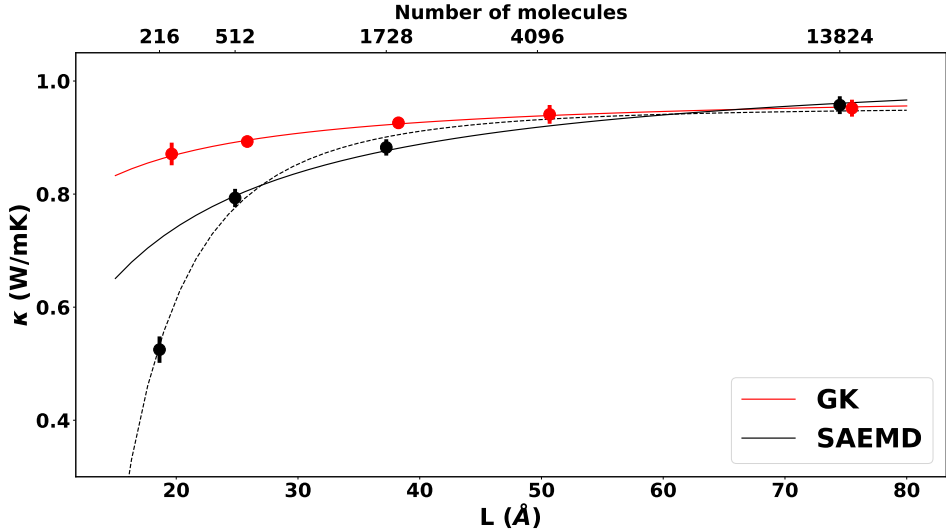
Figure 7.1: Thermal conductivity (κ) of water at 300K as a function of the linear size (L) of the cubic simulation cell and the number of water molecules. Results obtained with Green Kubo (GK) and close to equilibrium molecular dynamics simulations (SAEMD) are represented by red and black dots, respectively. Solid lines were obtained by fitting the data with Eq.5.21. We also show a fit of SAEMD results using Eq.5.22 (dotted black line). All simulations were performed with the TIP4P-2005f force field. GK results are slightly offset on the x axis to avoid overlap with SAEMD results.

Figure 7.1 shows our results for the thermal conductivity of water at 300K, 1 g/cm^3 using the TIP4P-20005f potential, computed using Green-Kubo and SAEMD simulations. Both methods yield almost identical extrapolated values of the thermal conductivity, within error bars: we obtained 0.98 ± 0.01 for GK and 0.95 ± 0.02 for SAEMD when using Eq.6 to fit the data and 1.04 ± 0.01 when using Eq. 5 to fit only 3 points. GK results were extrapolated using Eq. 5. We note that GK simulation results exhibit a weaker dependence on size: for example, in simulations with 512 water molecules, the GK value of κ is about 10% lower than
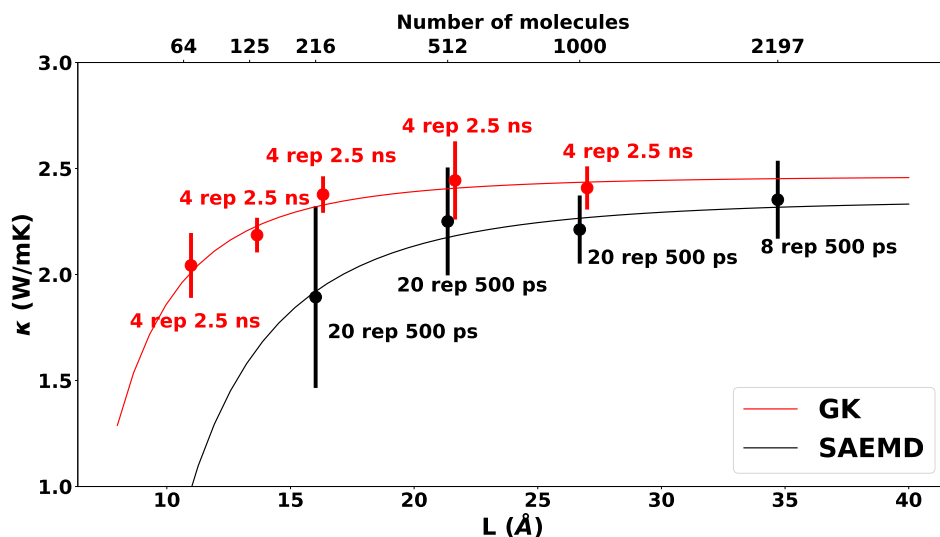
Figure 7.2: Thermal conductivity (κ) of water at 1000K and a density of 1.57 g/cm^3 as a function of the linear size (L) of the cubic simulation cell and the number of water molecules. Results obtained with Green Kubo (GK) and close to equilibrium molecular dynamics simulations (SAEMD) are represented by red and black dots, respectively. Solid lines were obtained by fitting the data with Eq. 5.22. All simulations were performed with the SPCE-Fl force field. GK results are slightly offset on the x axis to avoid overlap with SAEMD results.
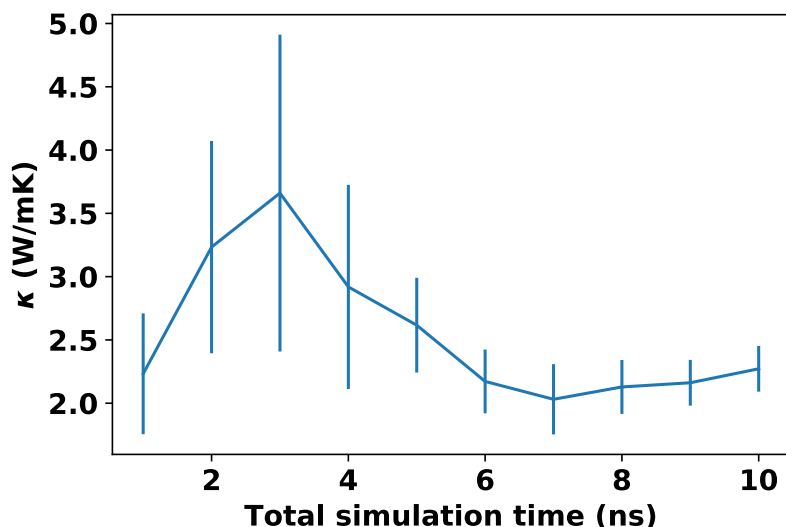
Figure 7.3: Thermal conductivity (κ) of water at 1000K and a density of 1.57 g/cm^3 computed with a 512 molecules cell by close to equilibrium molecular dynamics simulations, as a function of the total simulation time. All simulations were performed with the SPCE-Fl force field.
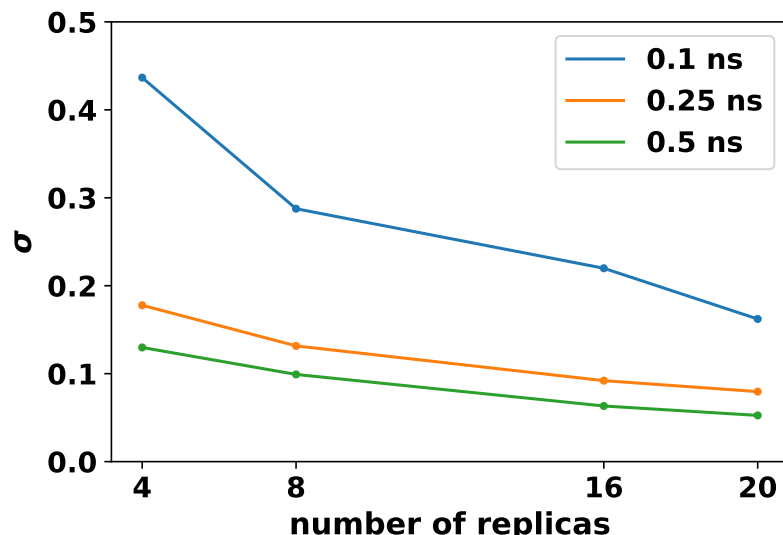
Figure 7.4: Average relative error (σ) in the computed thermal conductivity of water at 1000K and density of 1.57 g/cm^3, as a function of the number of replicas. Simulations were carried out with 512 molecules cells and the close to equilibrium approach, using the SPCE-Fl force field.

κ_∞, while that obtained with SAEMD is about 16% lower. We emphasize that while GK appears to be the method of choice when using empirical potentials, due to its weaker size dependence, the SAEMD approach offers the promise of efficiently performing simulations with neural-network-derived potentials and possibly using forces derived from DFT, since it does not require any calculation of the heat flux or of energy densities, but only of energies and forces.

In figure 7.2 we present our results for water at 1000K, and 9.7 GPa using the SPCE-Fl force field. The values of the thermal conductivity extrapolated using equation 5.22 are 2.47 ± 0.04 and 2.36 ± 0.06 for GK and SAEMD, respectively. As in the case of water at ambient conditions, size effects are more severe when using SAEMD, although in this case the two methods give the same results within statistical error bars for 512 molecules simulations. The increase of more than a factor of 2 of the thermal conductivity found here at extreme conditions is consistent with the observed increase of thermal conductivity of water with respect to pressure[159].

In figure 7.3 we show the thermal conductivity as a function of the total simulation time in a SAEMD simulation, when using 512 water molecules cells at 1000K, computed by averaging over 20 replicas, each simulated for 500 ps. We found that for a total simulation time equal to or larger than 5 ns, the results are approximately converged. In figure 7.4 we show the relative error in the thermal conductivity of water at 1000K using 512 molecules as a function of the number of replicas used and of the simulation time. The figure shows that, after a short simulation time of 100 ps, the error can be reduced by either increasing the simulation time or the number of replicas. While the total simulation time is the same for the same relative error, the option of increasing the number of replicas allows for independent parallel runs and shorter sequential times.

In table 7.1 we summarize available results for the thermal conductivity of water at $\approx$ 300K and 1 atm. None of the values reported in the table, except those obtained here for EIP, were extrapolated to obtain κ_∞ although some studies did increase the number of molecules in the cell in the direction of heat transport to test finite size effects. Overall we expect the values obtained with small cell sizes to be an underestimate of the extrapolated value for a given force-field; hence the apparent agreement with experiments is not necessarily representative of the accuracy of the force field or in general of the description of the interaction chosen in the simulations.

7.3   Water at extreme conditions using deepMD

An interesting direction to explore is the use of the approach in conjunction with deepMD potentials based on first principles forces[174]. In fact, we have successfully conducted a series of simulations of a 512 molecules cell of water molecules at high pressure and temperature using the deep-MD potential developed with the method of Ref.[174] and the close to equilibrium approach. The NN was trained on simulations performed with the SCAN exchange-correlation potential. The neural network was trained on thousands of simulations performed between 0 and 2500K, at pressure ranging from $\approx$ 0 to 100 GPa. We used the vast

Force Field	Method	T	κ	N_{mol}	t_s	N_{rep}	Ref.
TIP4P-2005f[156]	GK	300K	0.98(1)	13824	600 ps	4	this work
TIP4P-2005f	SAEMD	300K	0.95(2)	13824	500 ps	20	this work
deepMD	SAEMD	300K	0.85(3)	512	250 ps	20	this work
SPC[160]	NEMD	298K	0.88(2)	900	2 ns	1	[161]
SPC	NEMD	298K	0.776(19)	2180	1 ns	1	[162]
SPC	GK	298K	0.802(16)	2180	1 ns	1	[162]
SPCE[163]	NEMD	298K	0.930(16)	900	2 ns	1	[161]
SPC f[160][135]	NEMD	300K	0.7(1)	27036	300 ps	1	[135]
SPCE-F[164]	GK	300K	0.970(9)	180	40 ns	1	[54]
SPC-Fw[165]	GK	300K	0.854(104)	2180	1 ns	1	[162]
SPC-Fw	NEMD	300K	1.011(6)	2180	1 ns	1	[162]
SPC-Fd[166]	GK	300K	0.793(105)	2180	1 ns	1	[162]
SPC-Fd	NEMD	300K	0.977(12)	2180	1 ns	1	[162]
TIP3P[35]	NEMD	298K	0.880(19)	900	2 ns	1	[161]
TIP4P-2005[167]	NEMD	298K	0.910(14)	900	2 ns	1	[161]
TIP5P[168]	GK	298K	0.668(31)	2048	15-20 ns	6	[169]
TIP5P	NEMD	298K	0.680(7)	900	2 ns	1	[161]
TIP5P-Ew[170]	NEMD	298K	0.620(7)	900	2 ns	1	[161]
PBE[152]	GK	385K	0.74(12)	64	90 ps	1	[22]
PBE[152]	NEMD	353K	0.79	480	150 ps	1	[171]
Exp		300K	0.609				[172]
Exp		300K	0.6096				[173]

Table 7.1: Measured (Exp) and computed values of the thermal conductivity (κ (W/mK)) of water at density of $\simeq 1$ g/cm^3, obtained using different force fields (first column). All computed values were obtained using molecular dynamics with the Green Kubo (GK), non-equilibrium (NEMD) or close to equilibrium (SAEMD) approach (see second column) at a temperature (T (K)) given in the third column. The maximum number of molecules (N_{mol}) in the unit cell, the simulation time per replica (t_s) and the number of replicas (N_{rep} are given in column 5, 6 and 7, respectively.
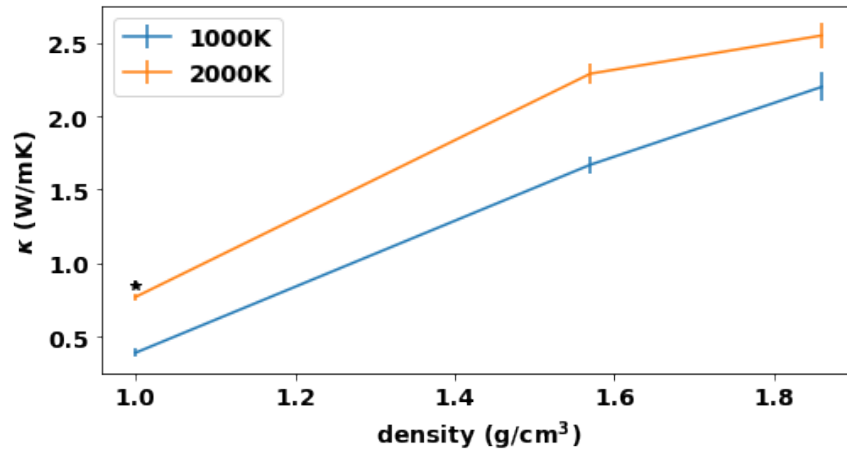
Figure 7.5: Thermal conductivity of water computed with SAEMD and deepMD as a function of temperature and density. Blue is 1000K, orange is 2000K. The black dot is the thermal conductivity at STP (300K, 1atm).
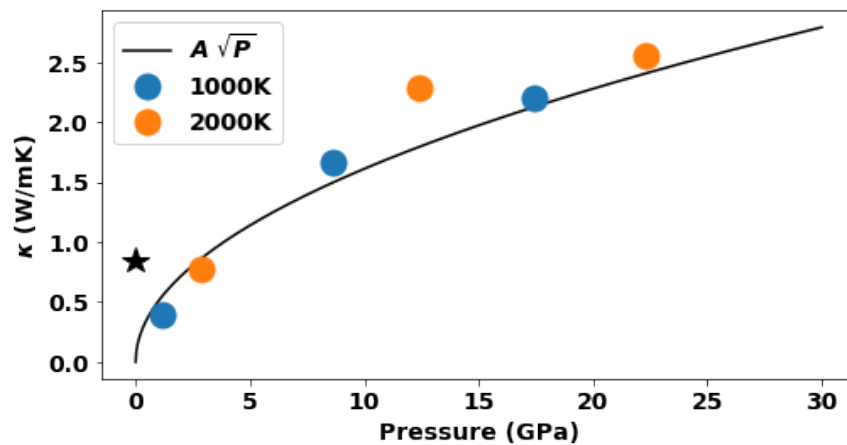
Figure 7.6: Thermal conductivity of water computed with SAEMD and deepMD as a function of pressure. Blue is 1000K, orange is 2000K. The black dot is the thermal conductivity at STP (300K, 1atm). Solid line is a fit with $A\sqrt{P}$

Temperature (K)	Density (g/cm^3)	Pressure (GPa)	κ (W/mK)
1000	1	1.2	0.39 ± 0.03
1000	1.57	8.6	1.67 ± 0.06
1000	1.86	17.4	2.2 ± 0.1
2000	1	2.9	0.77 ± 0.02
2000	1.57	12.4	2.29 ± 0.07
2000	1.86	22.3	2.55 ± 0.09

Table 7.2: Thermal conductivity of water at extreme temperature and pressure computed using SAEMD and deepMD

range of temperature and pressure over which the NN was trained to calculate the thermal conductivity of water at 1000K and 2000K, at densities between 1 g/cm^3 and 1.86 g/cm^3. We present our results in Fig. 7.5. We observed a large reduction in the thermal conductivity, at constant density, when going from 300K to 1000K, and an almost equal increase from 1000K to 2000K. This last trend continues as we study increasing density, and we see the thermal conductivity increase when going from 1000K to 2000K.

The reason for this behavior is not yet clear. We suspect this is due to two opposing trends: the increase in temperature disrupts the network of hydrogen-bond, and at the same time also causes dissociation. Further studies are necessary, but it is reasonable to speculate that the decrease in thermal conductivity we observed between 300 and 1000K is due to the breaking of the hydrogen-bond network. This trend is then reversed once water can dissociate, and the thermal conductivity again increases.

In Fig. 7.6 we show the same data as a function of pressure. There is still a dependence on the temperature, but the data show that pressure, rather than temperature, plays a dominant role in determining the thermal conductivity. We also included a simple fit with the square root of the pressure. There is no particular reason for the choice of this functional form, to our knowledge no model exist for the thermal conductivity of water in this pressure range and other functions are certainly possible.

7.4   Conclusions

In this chapter, we presented a method for the calculation of the thermal conductivity of liquids which relies on molecular dynamics simulations conducted close to equilibrium conditions, in the steady state. Similar to non-equilibrium molecular dynamics, and unlike equilibrium simulations based on GK, the method only requires the calculation of forces and total energies and the evaluation of heat fluxes and energy densities is not necessary. The close to equilibrium approach requires in general shorter simulation times than NEMD and thus allows one to take better advantage of parallel computing architectures. However, the cell size dependence found in the present work is still less favorable than that observed with GK simulations. Hence when using empirical force fields, for which the calculation of energy densities is straightforward and does not add any computational complexity, GK simulations should be the method of choice for homogeneous systems, from the standpoint of efficiency. Instead, in cases when computing energy densities and heat fluxes amount to additional, expensive calculations (as, e.g. in the case of first-principles simulations), SAEMD is expected to be the most efficient method for solid and the method presented here the most efficient one for liquids. We note however that, at least in the case of liquid water and ambient and extreme conditions studied here, the cell sizes and especially simulation times required for convergence still rule out the possibility of carrying out converged first principles simulations (and the same is true for GK). The results obtained here with empirical potentials and deepMD show an almost three-fold increase of the thermal conductivity of water when going standard conditions to high pressure and temperature conditions (P $\simeq$ 22 GPa and T$\simeq$ 2,000 K). Using the SAEMD and deepMD together allowed us to explore the thermal conductivity of water at extreme conditions, where dissociation plays a key factor in the structural and transport properties of water. Finally, we note that in the case of water, especially at ambient conditions, proton quantum effects are likely to play a significant role in determining the value of the thermal conductivity and that close to equilibrium simulations are expected to be more straightforward to couple to a path integral formulation than simulations based on the Green-

Kubo formalism. Data and workflows, with the exception of the deepMD data, are available online at https://paperstack.uchicago.edu/paperdetails/5eb086e8e092384bb26754dc

CHAPTER 8

SUMMARY AND CONCLUSIONS

Thermal transport concerns a variety of different disciplines and technological applications, for example thermal management in battery and microchip and efficiency in thermoelectric conversion devices. The accurate prediction of thermal transport coefficients is critical in helping the design of such devices. We described two of the more popular methods, Green-Kubo and Boltzmann Transport Equation. We also discussed at length their strengths and limitations, both in general and especially regarding *ab initio* simulations. We showed the applications of these methods in the study of thermal transport in MgO and PbTe. We carried a detailed comparison of several properties related to thermal transport and highlighted the role of each of these properties in the final value of the thermal conductivity.

Next, we presented the results of our study of the thermal conductivity of nano-porous silicon bridge, bridging the size gap between experiments and previous simulations, and discussed the role of the size and surface details of nanostructures in the reduction of thermal conductivity. We explored the effect of both the size of the pores and of porosity, showing how both affect the thermal conductivity. We also briefly discussed the role of surface oxidation on the thermal conductivity, and its relevance when the size of the pore is down to a few nm.

In the second section of this thesis, we presented a new method that we developed for the calculation of thermal conductivity in homogeneous solids and fluids. With this method, one can efficiently compute the thermal conductivity using either classical, first principle or neural-network Molecular Dynamics. We presented the application of this method to the calculation of the thermal conductivity of solid crystalline and nanocrystalline MgO and liquid water. To show the performance of our approach we computed the thermal conductivity of MgO from first principle and the thermal conductivity of water at extreme

temperature and pressure using a Neural Network potential trained on first principle data.

REFERENCES

[1] Tomoo Katsura. Thermal diffusivity of periclase at high temperatures and high pressures. *Physics of the Earth and Planetary Interiors*, 101(1):73 – 77, 1997. ISSN 0031-9201. doi: http://dx.doi.org/10.1016/S0031-9201(96)03223-2. URL `http://www.sciencedirect.com/science/article/pii/S0031920196032232`.

[2] Hiroo Kanamori, Naoyuki Fujii, and Hitoshi Mizutani. Thermal diffusivity measurement of rock-forming minerals from 300 to 1100 k. *Journal of Geophysical Research*, 73(2):595–605, 1968. ISSN 2156-2202. doi: 10.1029/JB073i002p00595. URL `http://dx.doi.org/10.1029/JB073i002p00595`.

[3] S. V. Garimella, T. Persoons, J. A. Weibel, and V. Gektin. Electronics thermal management in information and communications technologies: Challenges and future directions. *IEEE Transactions on Components, Packaging and Manufacturing Technology*, 7(8):1191–1205, Aug 2017. doi: 10.1109/TCPMT.2016.2603600.

[4] Saurabh Tembhurne, Fredy Nandjou, and Sophia Haussener. A thermally synergistic photo-electrochemical hydrogen generator operating under concentrated solar irradiation. *Nature Energy*, 4(5):399–407, 2019. ISSN 2058-7546. doi: 10.1038/s41560-019-0373-7. URL `https://doi.org/10.1038/s41560-019-0373-7`.

[5] Alan G. Whittington, Anne M. Hofmeister, and Peter I. Nabelek. Temperature-dependent thermal diffusivity of the earth's crust and implications for magmatism. *Nature*, 458(7236):319–321, 2009. ISSN 1476-4687. doi: 10.1038/nature07818. URL `https://doi.org/10.1038/nature07818`.

[6] Yangying Zhu, Jin Xie, Allen Pei, Bofei Liu, Yecun Wu, Dingchang Lin, Jun Li, Hansen Wang, Hao Chen, Jinwei Xu, Ankun Yang, Chun-Lan Wu, Hongxia Wang, Wei Chen, and Yi Cui. Fast lithium growth and short circuit induced by localized-temperature hotspots in lithium batteries. *Nature Communications*, 10(1):2067, 2019. ISSN 2041-1723. doi: 10.1038/s41467-019-09924-1. URL `https://doi.org/10.1038/s41467-019-09924-1`.

[7] M.S. Dresselhaus, G. Chen, M.Y. Tang, R.G. Yang, H. Lee, D.Z. Wang, Z.F. Ren, J.-P. Fleurial, and P. Gogna. New directions for low-dimensional thermoelectric materials. *Advanced Materials*, 19(8):1043–1053, 2007. ISSN 1521-4095. doi: 10.1002/adma.200600527. URL `http://dx.doi.org/10.1002/adma.200600527`.

[8] Fitriani, R. Ovik, B.D. Long, M.C. Barma, M. Riaz, M.F.M. Sabri, S.M. Said, and R. Saidur. A review on nanostructures of high-temperature thermoelectric materials for waste heat recovery. *Renewable and Sustainable Energy Reviews*, 64:635 – 659, 2016. ISSN 1364-0321. doi: http://dx.doi.org/10.1016/j.rser.2016.06.035. URL `http://www.sciencedirect.com/science/article/pii/S1364032116302581`.

[9] M. Zebarjadi. Heat management in thermoelectric power generators. *Sci Rep*, 6:20951, Apr 2016. ISSN 2045-2322. doi: 10.1038/srep20951. URL `http://www.ncbi.nlm.nih.gov/pmc/articles/PMC4817038/`.

[10] Ababacar Ndiaye, Abdérafi Charki, Abdessamad Kobi, Cheikh M.F. Kébé, Pape A. Ndiaye, and Vincent Sambou. Degradations of silicon photovoltaic modules: A literature review. *Solar Energy*, 96:140 – 151, 2013. ISSN 0038-092X. doi: https://doi.org/10.1016/j.solener.2013.07.005. URL `http://www.sciencedirect.com/science/article/pii/S0038092X13002703`.

[11] Xiaodong Lu, Yang Zhao, Zelai Wang, Jinjing Zhang, and Yang Song. Influence of environmental temperature and device temperature difference on output parameters of c-si solar cells. *Solar Energy*, 136:333 – 341, 2016. ISSN 0038-092X. doi: http://dx.doi.org/10.1016/j.solener.2016.07.013. URL `http://www.sciencedirect.com/science/article/pii/S0038092X16302717`.

[12] Miguel A. Modestino and Sophia Haussener. An integrated device view on photoelectrochemical solar-hydrogen generation. *Annual Review of Chemical and Biomolecular Engineering*, 6(1):13–34, 2015. doi: 10.1146/annurev-chembioeng-061114-123357. URL `http://dx.doi.org/10.1146/annurev-chembioeng-061114-123357`.

[13] Jayant Gopal Thakare, Chandan Pandey, M. M. Mahapatra, and R. S. Mulik. Thermal barrier coatings—a state of the art review. *Metals and Materials International*, Apr 2020. ISSN 2005-4149. doi: 10.1007/s12540-020-00705-w. URL `https://doi.org/10.1007/s12540-020-00705-w`.

[14] Eric Pop. Energy dissipation and transport in nanoscale devices. *Nano Research*, 3(3):147–169, Mar 2010. ISSN 1998-0000. doi: 10.1007/s12274-010-1019-z. URL `https://doi.org/10.1007/s12274-010-1019-z`.

[15] Ssennoga Twaha, Jie Zhu, Yuying Yan, and Bo Li. A comprehensive review of thermoelectric technology: Materials, applications, modelling and performance improvement. *Renewable and Sustainable Energy Reviews*, 65:698 – 726, 2016. ISSN 1364-0321. doi: https://doi.org/10.1016/j.rser.2016.07.034. URL `http://www.sciencedirect.com/science/article/pii/S1364032116303653`.

[16] G. S. Nolas, D. T. Morelli, and Terry M. Tritt. Skutterudites: A phonon-glass-electron crystal approach to advanced thermoelectric energy conversion applications. *Annual Review of Materials Science*, 29(1):89–116, 1999. doi: 10.1146/annurev.matsci.29.1.89. URL `https://doi.org/10.1146/annurev.matsci.29.1.89`.

[17] Toshiro Takabatake, Koichiro Suekuni, Tsuneyoshi Nakayama, and Eiji Kaneshita. Phonon-glass electron-crystal thermoelectric clathrates: Experiments and theory. *Rev. Mod. Phys.*, 86:669–716, Jun 2014. doi: 10.1103/RevModPhys.86.669. URL `https://link.aps.org/doi/10.1103/RevModPhys.86.669`.

[18] Xiaoliang Zeng, Jiajia Sun, Yimin Yao, Rong Sun, Jian-Bin Xu, and Ching-Ping Wong. A combination of boron nitride nanotubes and cellulose nanofibers for the preparation of a nanocomposite with high thermal conductivity. *ACS Nano*, 11(5):5167–5178, 2017. doi: 10.1021/acsnano.7b02359. URL `https://doi.org/10.1021/acsnano.7b02359`. PMID: 28402626.

[19] Chandramouli Subramaniam, Yuzuri Yasuda, Satoshi Takeya, Seisuke Ata, Ayumi Nishizawa, Don Futaba, Takeo Yamada, and Kenji Hata. Carbon nanotube-copper exhibiting metal-like thermal conductivity and silicon-like thermal expansion for efficient cooling of electronics. *Nanoscale*, 6:2669–2674, 2014. doi: 10.1039/C3NR05290G. URL http://dx.doi.org/10.1039/C3NR05290G.

[20] Freddy DeAngelis, Murali Gopal Muraleedharan, Jaeyun Moon, Hamid Reza Seyf, Austin J. Minnich, Alan J. H. McGaughey, and Asegun Henry. Thermal transport in disordered materials. *Nanoscale and Microscale Thermophysical Engineering*, 23(2):81–116, 2019. doi: 10.1080/15567265.2018.1519004. URL https://doi.org/10.1080/15567265.2018.1519004.

[21] Zhiwei Chen, Xinyue Zhang, Siqi Lin, Lidong Chen, and Yanzhong Pei. Rationalizing phonon dispersion for lattice thermal conductivity of solids. *National Science Review*, 5(6):888–894, 09 2018. ISSN 2095-5138. doi: 10.1093/nsr/nwy097. URL https://doi.org/10.1093/nsr/nwy097.

[22] Aris Marcolongo, Paolo Umari, and Stefano Baroni. Microscopic theory and quantum simulation of atomic heat transport. *Nature Physics*, 12(1):80–84, 2016. ISSN 1745-2473. doi: 10.1038/nphys3509. URL http://dx.doi.org/10.1038/nphys3509.

[23] Pavlo O. Dral. Quantum chemistry in the age of machine learning. *The Journal of Physical Chemistry Letters*, 11(6):2336–2347, 2020. doi: 10.1021/acs.jpclett.9b03664. URL https://doi.org/10.1021/acs.jpclett.9b03664. PMID: 32125858.

[24] David G. Cahill. Thermal conductivity measurement from 30 to 750 k: the 3ω method. *Review of Scientific Instruments*, 61(2): 802–808, 1990. doi: http://dx.doi.org/10.1063/1.1141498. URL http://scitation.aip.org/content/aip/journal/rsi/61/2/10.1063/1.1141498.

[25] Carolyn A. Paddock and Gary L. Eesley. Transient thermoreflectance from thin metal films. *Journal of Applied Physics*, 60(1):285–290, 1986. doi: 10.1063/1.337642. URL https://doi.org/10.1063/1.337642.

[26] Aaron J. Schmidt, Ramez Cheaito, and Matteo Chiesa. A frequency-domain thermoreflectance method for the characterization of thermal properties. *Review of Scientific Instruments*, 80(9):094901, 2009. doi: 10.1063/1.3212673. URL https://doi.org/10.1063/1.3212673.

[27] Marcello Puligheddu, Francois Gygi, and Giulia Galli. First-principles simulations of heat transport. *Phys. Rev. Materials*, 1: 060802, Nov 2017. doi: 10.1103/PhysRevMaterials.1.060802. URL https://link.aps.org/doi/10.1103/PhysRevMaterials.1.060802.

[28] Marcello Puligheddu and Giulia Galli. Atomistic simulations of the thermal conductivity of liquids. *Phys. Rev. Materials*, 4: 053801, May 2020. doi: 10.1103/PhysRevMaterials.4.053801. URL https://link.aps.org/doi/10.1103/PhysRevMaterials.4.053801.

[29] B. J. Alder and T. E. Wainwright. Studies in molecular dynamics. i. general method. *The Journal of Chemical Physics*, 31(2):459–466, 1959. doi: 10.1063/1.1730376. URL `https://doi.org/10.1063/1.1730376`.

[30] A. Rahman. Correlations in the motion of atoms in liquid argon. *Phys. Rev.*, 136:A405–A411, Oct 1964. doi: 10.1103/PhysRev.136.A405. URL `https://link.aps.org/doi/10.1103/PhysRev.136.A405`.

[31] Daan Frenkel and Berend Smit. Understanding molecular simulation: From algorithms to applications, 2002.

[32] C. Runge. Ueber die numerische auflösung von differentialgleichungen. *Mathematische Annalen*, 46(2):167–178, Jun 1895. ISSN 1432-1807. doi: 10.1007/BF01446807. URL `https://doi.org/10.1007/BF01446807`.

[33] D. Beeman. Some multistep methods for use in molecular dynamics calculations. *Journal of Computational Physics*, 20(2):130 – 139, 1976. ISSN 0021-9991. doi: https://doi.org/10.1016/0021-9991(76)90059-0. URL `http://www.sciencedirect.com/science/article/pii/0021999176900590`.

[34] M. Tuckerman, B. J. Berne, and G. J. Martyna. Reversible multiple time scale molecular dynamics. *The Journal of Chemical Physics*, 97(3):1990–2001, 1992. doi: 10.1063/1.463137. URL `https://doi.org/10.1063/1.463137`.

[35] William L. Jorgensen, Jayaraman Chandrasekhar, Jeffry D. Madura, Roger W. Impey, and Michael L. Klein. Comparison of simple potential functions for simulating liquid water. *The Journal of Chemical Physics*, 79(2):926–935, 1983. doi: 10.1063/1.445869. URL `https://doi.org/10.1063/1.445869`.

[36] Hiroki Nada and Jan P. J. M. van der Eerden. An intermolecular potential model for the simulation of ice and water near the melting point: A six-site model of H_2O. *The Journal of Chemical Physics*, 118(16):7401–7413, April 2003. doi: 10.1063/1.1562610. URL `https://ui.adsabs.harvard.edu/abs/2003JChPh.118.7401N`.

[37] P. Hohenberg and W. Kohn. Inhomogeneous electron gas. *Phys. Rev.*, 136:B864–B871, Nov 1964. doi: 10.1103/PhysRev.136.B864. URL `https://link.aps.org/doi/10.1103/PhysRev.136.B864`.

[38] R. Car and M. Parrinello. Unified approach for molecular dynamics and density-functional theory. *Phys. Rev. Lett.*, 55(22):2471–2474, November 1985. doi: 10.1103/PhysRevLett.55.2471. URL `https://ui.adsabs.harvard.edu/abs/1985PhRvL..55.2471C`.

[39] P. Güttinger. Das verhalten von atomen im magnetischen drehfeld. *Zeitschrift für Physik*, 73(3):169–184, Mar 1932. ISSN 1434-601X. doi: 10.1007/BF01351211. URL `https://doi.org/10.1007/BF01351211`.

[40] W. Kohn and L. J. Sham. Self-consistent equations including exchange and correlation effects. *Phys. Rev.*, 140:A1133–A1138, Nov 1965. doi: 10.1103/PhysRev.140.A1133. URL `https://link.aps.org/doi/10.1103/PhysRev.140.A1133`.

[41] Narbe Mardirossian and Martin Head-Gordon. Thirty years of density functional theory in computational chemistry: an overview and extensive assessment of 200 density functionals. *Molecular Physics*, 115 (19):2315–2372, 2017. doi: 10.1080/00268976.2017.1333644. URL `https://doi.org/10.1080/00268976.2017.1333644`.

[42] Stefan Chmiela, Alexandre Tkatchenko, Huziel E. Sauceda, Igor Poltavsky, Kristof T. Schütt, and Klaus-Robert Müller. Machine learning of accurate energy-conserving molecular force fields. *Science Advances*, 3(5), 2017. doi: 10.1126/sciadv.1603015. URL `https://advances.sciencemag.org/content/3/5/e1603015`.

[43] Venkatesh Botu and Rampi Ramprasad. Adaptive machine learning framework to accelerate ab initio molecular dynamics. *International Journal of Quantum Chemistry*, 115(16):1074–1083, 2015. doi: 10.1002/qua.24836. URL `https://onlinelibrary.wiley.com/doi/abs/10.1002/qua.24836`.

[44] Linfeng Zhang, Jiequn Han, Han Wang, Roberto Car, and Weinan E. Deep potential molecular dynamics: A scalable model with the accuracy of quantum mechanics. *Phys. Rev. Lett.*, 120:143001, Apr 2018. doi: 10.1103/PhysRevLett.120.143001. URL `https://link.aps.org/doi/10.1103/PhysRevLett.120.143001`.

[45] Jianwei Sun, Adrienn Ruzsinszky, and John P. Perdew. Strongly constrained and appropriately normed semilocal density functional. *Phys. Rev. Lett.*, 115:036402, Jul 2015. doi: 10.1103/PhysRevLett.115.036402. URL `https://link.aps.org/doi/10.1103/PhysRevLett.115.036402`.

[46] Melville S. Green. Markoff random processes and the statistical mechanics of time-dependent phenomena. *The Journal of Chemical Physics*, 20(8):1281–1295, 1952. doi: 10.1063/1.1700722. URL `https://doi.org/10.1063/1.1700722`.

[47] Melville S. Green. Markoff random processes and the statistical mechanics of time-dependent phenomena. ii. irreversible processes in fluids. *The Journal of Chemical Physics*, 22(3):398–413, 1954. doi: 10.1063/1.1740082. URL `https://doi.org/10.1063/1.1740082`.

[48] Ryogo Kubo, Mario Yokota, and Sadao Nakajima. Statistical-mechanical theory of irreversible processes. ii. response to thermal disturbance. *Journal of the Physical Society of Japan*, 12(11):1203–1211, 1957. doi: 10.1143/JPSJ.12.1203. URL `https://doi.org/10.1143/JPSJ.12.1203`.

[49] Ryogo Kubo. Statistical-mechanical theory of irreversible processes. i. general theory and simple applications to magnetic and conduction problems. *Journal of the Physical Society of Japan*, 12(6):570–586, 1957. doi: 10.1143/JPSJ.12.570. URL `https://doi.org/10.1143/JPSJ.12.570`.

[50] Leo P Kadanoff and Paul C Martin. Hydrodynamic equations and correlation functions. *Annals of Physics*, 24:419 – 469, 1963. ISSN 0003-4916. doi: https://doi.org/10.1016/0003-4916(63)90078-2. URL `http://www.sciencedirect.com/science/article/pii/0003491663900782`.

[51] von D . Forster. Hydrodynamic fluctuations, broken symmetry and correlation functions. *Physik in unserer Zeit*, 7(3):96–96, 1976. doi: 10.1002/piuz.19760070307. URL `https://onlinelibrary.wiley.com/doi/abs/10.1002/piuz.19760070307`.

[52] Stefano Baroni, Riccardo Bertossa, Loris Ercole, Federico Grasselli, and Aris Marcolongo. *Heat Transport in Insulators from Ab Initio Green-Kubo Theory*, pages 1–36. Springer International Publishing, Cham, 2018. ISBN 978-3-319-50257-1. doi: 10.1007/978-3-319-50257-1_12-1. URL `https://doi.org/10.1007/978-3-319-50257-1_12-1`.

[53] Loris Ercole, Aris Marcolongo, Paolo Umari, and Stefano Baroni. Gauge invariance of thermal transport coefficients. *Journal of Low Temperature Physics*, pages 1–8, 2016. ISSN 1573-7357. doi: 10.1007/s10909-016-1617-6. URL `http://dx.doi.org/10.1007/s10909-016-1617-6`.

[54] Loris Ercole, Aris Marcolongo, and Stefano Baroni. Accurate thermal conductivities from optimally short molecular dynamics simulations. *Scientific Reports*, 7(1):15835, 2017. ISSN 2045-2322. doi: 10.1038/s41598-017-15843-2. URL `https://doi.org/10.1038/s41598-017-15843-2`.

[55] Daichi Torii, Takeo Nakano, and Taku Ohara. Contribution of inter- and intramolecular energy transfers to heat conduction in liquids. *The Journal of Chemical Physics*, 128(4): 044504, 2008. doi: 10.1063/1.2821963. URL `https://doi.org/10.1063/1.2821963`.

[56] G.D. Mahan. *Many-Particle Physics*. Physics of Solids and Liquids. Springer, 2000. ISBN 9780306463389. URL `https://books.google.com/books?id=xzSgZ4-yyMEC`.

[57] Tianli Feng and Xiulin Ruan. Quantum mechanical prediction of four-phonon scattering rates and reduced thermal conductivity of solids. *Phys. Rev. B*, 93:045202, Jan 2016. doi: 10.1103/PhysRevB.93.045202. URL `https://link.aps.org/doi/10.1103/PhysRevB.93.045202`.

[58] Tianli Feng and Xiulin Ruan. Erratum: Quantum mechanical prediction of four-phonon scattering rates and reduced thermal conductivity of solids [phys. rev. b 93, 045202 (2016)]. *Phys. Rev. B*, 97:079901, Feb 2018. doi: 10.1103/PhysRevB.97.079901. URL `https://link.aps.org/doi/10.1103/PhysRevB.97.079901`.

[59] Tianli Feng, Lucas Lindsay, and Xiulin Ruan. Four-phonon scattering significantly reduces intrinsic thermal conductivity of solids. *Phys. Rev. B*, 96:161201, Oct 2017. doi: 10.1103/PhysRevB.96.161201. URL `https://link.aps.org/doi/10.1103/PhysRevB.96.161201`.

[60] A. A. Maradudin and A. E. Fein. Scattering of neutrons by an anharmonic crystal. *Phys. Rev.*, 128:2589–2608, Dec 1962. doi: 10.1103/PhysRev.128.2589. URL `https://link.aps.org/doi/10.1103/PhysRev.128.2589`.

[61] Wu Li, L. Lindsay, D. A. Broido, Derek A. Stewart, and Natalio Mingo. Thermal conductivity of bulk and nanowire $mg_2si_xsn_{1-x}$ alloys from first principles. *Phys. Rev. B*, 86:174307, Nov 2012. doi: 10.1103/PhysRevB.86.174307. URL `https://link.aps.org/doi/10.1103/PhysRevB.86.174307`.

[62] Wu Li, Jesús Carrete, Nebil A. Katcho, and Natalio Mingo. Shengbte: A solver of the boltzmann transport equation for phonons. *Computer Physics Communications*, 185(6):1747 – 1758, 2014. ISSN 0010-4655. doi: http://dx.doi.org/10.1016/j.cpc.2014.02.015. URL `http://www.sciencedirect.com/science/article/pii/S0010465514000484`.

[63] M Omini and A Sparavigna. An iterative approach to the phonon boltzmann equation in the theory of thermal conductivity. *Physica B: Condensed Matter*, 212(2):101 – 112, 1995. ISSN 0921-4526. doi: https://doi.org/10.1016/0921-4526(95)00016-3. URL `http://www.sciencedirect.com/science/article/pii/0921452695000163`.

[64] M. Omini and A. Sparavigna. Beyond the isotropic-model approximation in the theory of thermal conductivity. *Phys. Rev. B*, 53:9064–9073, Apr 1996. doi: 10.1103/PhysRevB.53.9064. URL `http://link.aps.org/doi/10.1103/PhysRevB.53.9064`.

[65] D. A. Broido, A. Ward, and N. Mingo. Lattice thermal conductivity of silicon from empirical interatomic potentials. *Phys. Rev. B*, 72:014308, Jul 2005. doi: 10.1103/PhysRevB.72.014308. URL `http://link.aps.org/doi/10.1103/PhysRevB.72.014308`.

[66] Yi Xia. Revisiting lattice thermal transport in pbte: The crucial role of quartic anharmonicity. *Applied Physics Letters*, 113(7):073901, 2018. doi: 10.1063/1.5040887. URL `https://doi.org/10.1063/1.5040887`.

[67] P. Souvatzis, O. Eriksson, M.I. Katsnelson, and S.P. Rudin. The self-consistent ab initio lattice dynamical method. *Computational Materials Science*, 44(3):888 – 894, 2009. ISSN 0927-0256. doi: https://doi.org/10.1016/j.commatsci.2008.06.016. URL `http://www.sciencedirect.com/science/article/pii/S0927025608003121`.

[68] Ion Errea, Matteo Calandra, and Francesco Mauri. Anharmonic free energies and phonon dispersions from the stochastic self-consistent harmonic approximation: Application to platinum and palladium hydrides. *Phys. Rev. B*, 89:064302, Feb 2014. doi: 10.1103/PhysRevB.89.064302. URL `https://link.aps.org/doi/10.1103/PhysRevB.89.064302`.

[69] O. Hellman, I. A. Abrikosov, and S. I. Simak. Lattice dynamics of anharmonic solids from first principles. *Phys. Rev. B*, 84:180301, Nov 2011. doi: 10.1103/PhysRevB.84.180301. URL `https://link.aps.org/doi/10.1103/PhysRevB.84.180301`.

[70] Terumasa Tadano and Shinji Tsuneyuki. Self-consistent phonon calculations of lattice dynamical properties in cubic srtio$_3$ with first-principles anharmonic force constants. *Phys. Rev. B*, 92:054301, Aug 2015. doi: 10.1103/PhysRevB.92.054301. URL `https://link.aps.org/doi/10.1103/PhysRevB.92.054301`.

[71] Ambroise van Roekeghem, Jesús Carrete, and Natalio Mingo. Anomalous thermal conductivity and suppression of negative thermal expansion in scf$_3$. *Phys. Rev. B*, 94:020303, Jul 2016. doi: 10.1103/PhysRevB.94.020303. URL `https://link.aps.org/doi/10.1103/PhysRevB.94.020303`.

[72] Fei Zhou, Weston Nielson, Yi Xia, and Vidvuds Ozoliņš. Lattice anharmonicity and thermal conductivity from compressive sensing of first-principles calculations. *Phys. Rev. Lett.*, 113:185501, Oct 2014. doi: 10.1103/PhysRevLett.113.185501. URL `http://link.aps.org/doi/10.1103/PhysRevLett.113.185501`.

[73] D.C. Wallace. *Thermodynamics of Crystals*. Dover books on physics. Dover Publications, 1998. ISBN 9780486402123. URL `https://books.google.com/books?id=qLzOmwSgMIsC`.

[74] Yi Xia and Maria K. Y. Chan. Anharmonic stabilization and lattice heat transport in rocksalt β-gete. *Applied Physics Letters*, 113(19):193902, 2018. doi: 10.1063/1.5048814.

[75] Fei Zhou, Weston Nielson, Yi Xia, and Vidvuds Ozoliņš. Lattice anharmonicity and thermal conductivity from compressive sensing of first-principles calculations. *Phys. Rev. Lett.*, 113:185501, Oct 2014. doi: 10.1103/PhysRevLett.113.185501. URL `http://link.aps.org/doi/10.1103/PhysRevLett.113.185501`.

[76] Shuichi Nosé. A unified formulation of the constant temperature molecular dynamics methods. *The Journal of Chemical Physics*, 81(1):511–519, 1984. doi: 10.1063/1.447334. URL `https://doi.org/10.1063/1.447334`.

[77] J. E. Turney, E. S. Landry, A. J. H. McGaughey, and C. H. Amon. Predicting phonon properties and thermal conductivity from anharmonic lattice dynamics calculations and molecular dynamics simulations. *Phys. Rev. B*, 79:064301, Feb 2009. doi: 10.1103/PhysRevB.79.064301. URL `https://link.aps.org/doi/10.1103/PhysRevB.79.064301`.

[78] Yuping He, Ivana Savic, Davide Donadio, and Giulia Galli. Lattice thermal conductivity of semiconducting bulk materials: atomistic simulations. *Phys. Chem. Chem. Phys.*, 14:16209–16222, 2012. doi: 10.1039/C2CP42394D. URL `http://dx.doi.org/10.1039/C2CP42394D`.

[79] Christian Carbogno, Rampi Ramprasad, and Matthias Scheffler. Ab initio green-kubo approach for the thermal conductivity of solids. *Phys. Rev. Lett.*, 118:175901, Apr 2017. doi: 10.1103/PhysRevLett.118.175901. URL `https://link.aps.org/doi/10.1103/PhysRevLett.118.175901`.

[80] C. Z. Wang, C. T. Chan, and K. M. Ho. Tight-binding molecular-dynamics study of phonon anharmonic effects in silicon and diamond. *Phys. Rev. B*, 42:11276–11283, Dec 1990. doi: 10.1103/PhysRevB.42.11276. URL `https://link.aps.org/doi/10.1103/PhysRevB.42.11276`.

[81] Young Hee Lee, R. Biswas, C. M. Soukoulis, C. Z. Wang, C. T. Chan, and K. M. Ho. Molecular-dynamics simulation of thermal conductivity in amorphous silicon. *Phys. Rev. B*, 43:6573–6580, Mar 1991. doi: 10.1103/PhysRevB.43.6573. URL `https://link.aps.org/doi/10.1103/PhysRevB.43.6573`.

[82] J.M. Ziman. *Electrons and Phonons: The Theory of Transport Phenomena in Solids*. International series of monographs on physics. OUP Oxford, 1960. ISBN 9780198507796. URL `https://books.google.com/books?id=UtEy63pjngsC`.

[83] G.P. Srivastava. *The Physics of Phonons*. Taylor & Francis, 1990. ISBN 9780852741535. URL `https://books.google.com/books?id=OE-bHd2gzVgC`.

[84] R.E. Peierls. *Quantum Theory of Solids*. International Series of Monographs on Physics. Clarendon Press, 1996. ISBN 9780192670175. URL `https://books.google.com/books?id=GIrsImJvMgMC`.

[85] Alberto Debernardi, Stefano Baroni, and Elisa Molinari. Anharmonic phonon lifetimes in semiconductors from density-functional perturbation theory. *Phys. Rev. Lett.*, 75:1819–1822, Aug 1995. doi: 10.1103/PhysRevLett.75.1819. URL `http://link.aps.org/doi/10.1103/PhysRevLett.75.1819`.

[86] G. Deinzer, G. Birner, and D. Strauch. Ab initio calculation of the linewidth of various phonon modes in germanium and silicon. *Phys. Rev. B*, 67:144304, Apr 2003. doi: 10.1103/PhysRevB.67.144304. URL `https://link.aps.org/doi/10.1103/PhysRevB.67.144304`.

[87] D. A. Broido, M. Malorny, G. Birner, Natalio Mingo, and D. A. Stewart. Intrinsic lattice thermal conductivity of semiconductors from first principles. *Appl. Phys. Lett.*, 91(23):231922, 2007. doi: http://dx.doi.org/10.1063/1.2822891. URL `http://scitation.aip.org/content/aip/journal/apl/91/23/10.1063/1.2822891`.

[88] Philip B. Allen, Joseph L. Feldman, Jaroslav Fabian, and Frederick Wooten. Diffusons, locons and propagons: Character of atomie vibrations in amorphous si. *Philosophical Magazine B*, 79(11-12):1715–1731, 1999. doi: 10.1080/13642819908223054. URL `https://doi.org/10.1080/13642819908223054`.

[89] Hamid Reza Seyf, Luke Yates, Thomas L. Bougher, Samuel Graham, Baratunde A. Cola, Theeradetch Detchprohm, Mi-Hee Ji, Jeomoh Kim, Russell Dupuis, Wei Lv, and Asegun Henry. Rethinking phonons: The issue of disorder. *npj Computational Materials*, 3(1):49, 2017. doi: 10.1038/s41524-017-0052-9. URL `https://doi.org/10.1038/s41524-017-0052-9`.

[90] Andrea Cepellotti and Nicola Marzari. Thermal transport in crystals as a kinetic theory of relaxons. *Phys. Rev. X*, 6:041013, Oct 2016. doi: 10.1103/PhysRevX.6.041013. URL `http://link.aps.org/doi/10.1103/PhysRevX.6.041013`.

[91] J. E. Turney, A. J. H. McGaughey, and C. H. Amon. Assessing the applicability of quantum corrections to classical thermal conductivity predictions. *Phys. Rev. B*, 79:224305, Jun 2009. doi: 10.1103/PhysRevB.79.224305. URL `https://link.aps.org/doi/10.1103/PhysRevB.79.224305`.

[92] P. Shukla, T. Watanabe, J.C. Nino, J.S. Tulenko, and S.R. Phillpot. Thermal transport properties of mgo and nd2zr2o7 pyrochlore by molecular dynamics simulation. *Journal of Nuclear Materials*, 380(1–3):1 – 7, 2008. ISSN 0022-3115. doi: http://dx.doi.org/10.1016/j.jnucmat.2008.06.043. URL `http://www.sciencedirect.com/science/article/pii/S0022311508003632`.

[93] Bo Qiu, Hua Bao, Gengqiang Zhang, Yue Wu, and Xiulin Ruan. Molecular dynamics simulations of lattice thermal conductivity and spectral phonon mean free path of pbte: Bulk and nanostructures. *Computational Materials Science*, 53(1):278 – 285, 2012. ISSN 0927-0256. doi: https://doi.org/10.1016/j.commatsci.2011.08.016. URL `http://www.sciencedirect.com/science/article/pii/S0927025611004770`.

[94] M. M. Beg. Debye temperature of MgO powder by elastic neutron scattering. *Acta Crystallographica Section A*, 32(1):154–156, Jan 1976. doi: 10.1107/S0567739476000296. URL `https://doi.org/10.1107/S0567739476000296`.

[95] Bland Houston, R. E. Strakna, and Henry S. Belson. Elastic constants, thermal expansion, and debye temperature of lead telluride. *Journal of Applied Physics*, 39(8):3913–3916, 1968. doi: 10.1063/1.1656874. URL `https://doi.org/10.1063/1.1656874`.

[96] Steve Plimpton. Fast parallel algorithms for short-range molecular dynamics. *Journal of Computational Physics*, 117(1):1 – 19, 1995. ISSN 0021-9991. doi: https://doi.org/10.1006/jcph.1995.1039. URL `http://www.sciencedirect.com/science/article/pii/S002199918571039X`.

[97] K. Parlinski, Z. Q. Li, and Y. Kawazoe. First-principles determination of the soft mode in cubic zro$_2$. *Phys. Rev. Lett.*, 78: 4063–4066, May 1997. doi: 10.1103/PhysRevLett.78.4063. URL `https://link.aps.org/doi/10.1103/PhysRevLett.78.4063`.

[98] Atsushi Togo and Isao Tanaka. First principles phonon calculations in materials science. *Scripta Materialia*, 108:1 – 5, 2015. ISSN 1359-6462. doi: https://doi.org/10.1016/j.scriptamat.2015.07.021. URL `http://www.sciencedirect.com/science/article/pii/S1359646215003127`.

[99] Lance J. Nelson, Gus L. W. Hart, Fei Zhou, and Vidvuds Ozoliņš. Compressive sensing as a paradigm for building physics models. *Phys. Rev. B*, 87:035125, Jan 2013. doi: 10.1103/PhysRevB.87.035125. URL `http://link.aps.org/doi/10.1103/PhysRevB.87.035125`.

[100] Lance J. Nelson, Vidvuds Ozoliņš, C. Shane Reese, Fei Zhou, and Gus L. W. Hart. Cluster expansion made easy with bayesian compressive sensing. *Phys. Rev. B*, 88:155105, Oct 2013. doi: 10.1103/PhysRevB.88.155105. URL `http://link.aps.org/doi/10.1103/PhysRevB.88.155105`.

[101] Ion Errea, Bruno Rousseau, and Aitor Bergara. Anharmonic stabilization of the high-pressure simple cubic phase of calcium. *Phys. Rev. Lett.*, 106:165501, Apr 2011. doi: 10.1103/PhysRevLett.106.165501. URL `https://link.aps.org/doi/10.1103/PhysRevLett.106.165501`.

[102] Hilaal Alam and Seeram Ramakrishna. A review on the enhancement of figure of merit from bulk to nano-thermoelectric materials. *Nano Energy*, 2(2):190 – 212, 2013. ISSN 2211-2855. doi: https://doi.org/10.1016/j.nanoen.2012.10.005. URL `http://www.sciencedirect.com/science/article/pii/S2211285512002078`.

[103] Maria N. Luckyanova, Jivtesh Garg, Keivan Esfarjani, Adam Jandl, Mayank T. Bulsara, Aaron J. Schmidt, Austin J. Minnich, Shuo Chen, Mildred S. Dresselhaus, Zhifeng Ren, Eugene A. Fitzgerald, and Gang Chen. Coherent phonon heat conduction in superlattices. *Science*, 338(6109):936–939, 2012. ISSN 0036-8075. doi: 10.1126/science.1225549. URL `https://science.sciencemag.org/content/338/6109/936`.

[104] Jayakanth Ravichandran, Ajay K. Yadav, Ramez Cheaito, Pim B. Rossen, Arsen Soukiassian, S. J. Suresha, John C. Duda, Brian M. Foley, Che-Hui Lee, Ye Zhu, Arthur W. Lichtenberger, Joel E. Moore, David A. Muller, Darrell G. Schlom, Patrick E. Hopkins, Arun Majumdar, Ramamoorthy Ramesh, and Mark A. Zurbuchen. Crossover from incoherent to coherent phonon scattering in epitaxial oxide superlattices. *Nature Materials*, 13(2):168–172, Feb 2014. ISSN 1476-4660. doi: 10.1038/nmat3826. URL `https://doi.org/10.1038/nmat3826`.

[105] Davide Donadio and Giulia Galli. Atomistic simulations of heat transport in silicon nanowires. *Phys. Rev. Lett.*, 102:195901, May 2009. doi: 10.1103/PhysRevLett.102.195901. URL `https://link.aps.org/doi/10.1103/PhysRevLett.102.195901`.

[106] Yunshan Zhao, Dan Liu, Jie Chen, Liyan Zhu, Alex Belianinov, Olga S. Ovchinnikova, Raymond R. Unocic, Matthew J. Burch, Songkil Kim, Hanfang Hao, Daniel S. Pickard, Baowen Li, and John T. L. Thong. Engineering the thermal conductivity along an individual silicon nanowire by selective helium ion irradiation. *Nature Communications*, 8(1):15919, Jun 2017. ISSN 2041-1723. doi: 10.1038/ncomms15919. URL `https://doi.org/10.1038/ncomms15919`.

[107] Allon I. Hochbaum, Renkun Chen, Raul Diaz Delgado, Wenjie Liang, Erik C. Garnett, Mark Najarian, Arun Majumdar, and Peidong Yang. Enhanced thermoelectric performance of rough silicon nanowires. *Nature*, 451(7175):163–167, Jan 2008. ISSN 1476-4687. doi: 10.1038/nature06381. URL `https://doi.org/10.1038/nature06381`.

[108] Martin Maldovan. Sound and heat revolutions in phononics. *Nature*, 503 (7475):209–217, Nov 2013. ISSN 1476-4687. doi: 10.1038/nature12608. URL `https://doi.org/10.1038/nature12608`.

[109] Jen-Kan Yu, Slobodan Mitrovic, Douglas Tham, Joseph Varghese, and James R. Heath. Reduction of thermal conductivity in phononic nanomesh structures. *Nature Nanotechnology*, 5(10):718–721, Oct 2010. ISSN 1748-3395. doi: 10.1038/nnano.2010.149. URL `https://doi.org/10.1038/nnano.2010.149`.

[110] Patrick E. Hopkins, Charles M. Reinke, Mehmet F. Su, Roy H. Olsson, Eric A. Shaner, Zayd C. Leseman, Justin R. Serrano, Leslie M. Phinney, and Ihab El-Kady. Reduction in the thermal conductivity of single crystalline silicon by phononic crystal patterning. *Nano Letters*, 11(1):107–112, 2011. doi: 10.1021/nl102918q. URL `https://doi.org/10.1021/nl102918q`. PMID: 21105717.

[111] Seyedhamidreza Alaie, Drew F. Goettler, Mehmet Su, Zayd C. Leseman, Charles M. Reinke, and Ihab El-Kady. Thermal transport in phononic crystals and the observation of coherent phonon scattering at room temperature. *Nature Communications*, 6(1):7228, Jun 2015. ISSN 2041-1723. doi: 10.1038/ncomms8228. URL `https://doi.org/10.1038/ncomms8228`.

[112] Masahiro Nomura, Junichiro Shiomi, Takuma Shiga, and Roman Anufriev. Thermal phonon engineering by tailored nanostructures. *Japanese Journal of Applied Physics*, 57(8):080101, jul 2018. doi: 10.7567/jjap.57.080101. URL `https://doi.org/10.7567%2Fjjap.57.080101`.

[113] Jongwoo Lim, Hung-Ta Wang, Jinyao Tang, Sean C. Andrews, Hongyun So, Jaeho Lee, Dong Hyun Lee, Thomas P. Russell, and Peidong Yang. Simultaneous thermoelectric property measurement and incoherent phonon transport in holey silicon. *ACS Nano*, 10(1):124–132, Jan 2016. ISSN 1936-0851. doi: 10.1021/acsnano.5b05385. URL `https://doi.org/10.1021/acsnano.5b05385`.

[114] Roman Anufriev, Jose Ordonez-Miranda, and Masahiro Nomura. Measurement of the phonon mean free path spectrum in silicon membranes at different temperatures using arrays of nanoslits. *Phys. Rev. B*, 101:115301, Mar 2020. doi: 10.1103/PhysRevB.101.115301. URL `https://link.aps.org/doi/10.1103/PhysRevB.101.115301`.

[115] Paul Franklin Nealey, Huiman Kang, Guoliang Liu, Hiroshi Yoshida, Yashuhiko Tada-Juan, Jose de Pablo, and Abelardo Ramirez-Hernandez. Directed assembly of block copolymer films between a chemically patterned surface and a second surface, 2017. URL `http://v3.espacenet.com/textdoc?IDX=EP1700367`.

[116] Yuping He, Davide Donadio, Joo-Hyoung Lee, Jeffrey C. Grossman, and Giulia Galli. Thermal transport in nanoporous silicon: Interplay between disorder at mesoscopic and atomic scales. *ACS Nano*, 5(3):1839–1844, 2011. doi: 10.1021/nn2003184. URL `https://doi.org/10.1021/nn2003184`.

[117] Joo-Hyoung Lee, Giulia A. Galli, and Jeffrey C. Grossman. Nanoporous si as an efficient thermoelectric material. *Nano Letters*, 8(11):3750–3754, 2008. doi: 10.1021/nl802045f. URL `https://doi.org/10.1021/nl802045f`.

[118] Roman Anufriev, Jeremie Maire, and Masahiro Nomura. Reduction of thermal conductivity by surface scattering of phonons in periodic silicon nanostructures. *Phys. Rev. B*, 93:045411, Jan 2016. doi: 10.1103/PhysRevB.93.045411. URL `https://link.aps.org/doi/10.1103/PhysRevB.93.045411`.

[119] Sooran Kim, Kyoo Kim, Chang-Jong Kang, and B. I. Min. Correlation-assisted phonon softening and the orbital-selective peierls transition in vo$_2$. *Phys. Rev. B*, 87:195106, May 2013. doi: 10.1103/PhysRevB.87.195106. URL `https://link.aps.org/doi/10.1103/PhysRevB.87.195106`.

[120] Roman Anufriev, Aymeric Ramiere, Jeremie Maire, and Masahiro Nomura. Heat guiding and focusing using ballistic phonon transport in phononic nanostructures. *Nature Communications*, 8(1):15505, May 2017. ISSN 2041-1723. doi: 10.1038/ncomms15505. URL `https://doi.org/10.1038/ncomms15505`.

[121] Jinyao Tang, Hung-Ta Wang, Dong Hyun Lee, Melissa Fardy, Ziyang Huo, Thomas P. Russell, and Peidong Yang. Holey silicon as an efficient thermoelectric material. *Nano Letters*, 10(10):4279–4283, 2010. doi: 10.1021/nl102931z. URL `https://doi.org/10.1021/nl102931z`. PMID: 20839780.

[122] Ricardo Ruiz, Huiman Kang, François A. Detcheverry, Elizabeth Dobisz, Dan S. Kercher, Thomas R. Albrecht, Juan J. de Pablo, and Paul F. Nealey. Density multiplication and improved lithography by directed block copolymer assembly. *Science*, 321(5891):936–939, 2008. ISSN 0036-8075. doi: 10.1126/science.1157626. URL `https://science.sciencemag.org/content/321/5891/936`.

[123] Steve Plimpton. Fast parallel algorithms for short-range molecular dynamics. *Journal of Computational Physics*, 117(1):1 – 19, 1995. ISSN 0021-9991. doi: http://dx.doi.org/10.1006/jcph.1995.1039. URL `http://www.sciencedirect.com/science/article/pii/S002199918571039X`.

[124] J. Tersoff. Modeling solid-state chemistry: Interatomic potentials for multicomponent systems. *Phys. Rev. B*, 39:5566–5568, Mar 1989. doi: 10.1103/PhysRevB.39.5566. URL `https://link.aps.org/doi/10.1103/PhysRevB.39.5566`.

[125] Shinji Munetoh, Teruaki Motooka, Koji Moriguchi, and Akira Shintani. Interatomic potential for si–o systems using tersoff parameterization. *Computational Materials Science*, 39(2):334 – 339, 2007. ISSN 0927-0256. doi: https://doi.org/10.1016/j.commatsci.2006.06.010. URL `http://www.sciencedirect.com/science/article/pii/S0927025606002023`.

[126] Elisabeth M. Ashley and Paul F. Nealey. Private Communication, 2020.

[127] Hossein Honarvar and Mahmoud I. Hussein. Two orders of magnitude reduction in silicon membrane thermal conductivity by resonance hybridizations. *Phys. Rev. B*, 97:195413, May 2018. doi: 10.1103/PhysRevB.97.195413. URL `https://link.aps.org/doi/10.1103/PhysRevB.97.195413`.

[128] Ming-Shan Jeng, Ronggui Yang, David Song, and Gang Chen. Modeling the Thermal Conductivity and Phonon Transport in Nanoparticle Composites Using Monte Carlo Simulation. *Journal of Heat Transfer*, 130(4), 03 2008. ISSN 0022-1481. doi: 10.1115/1.2818765. URL `https://doi.org/10.1115/1.2818765`. 042410.

[129] M. Verdier, K. Termentzidis, and D. Lacroix. Crystalline-amorphous silicon nano-composites: Nano-pores and nano-inclusions impact on the thermal conductivity. *Journal of Applied Physics*, 119(17):175104, 2016. doi: 10.1063/1.4948337. URL `https://doi.org/10.1063/1.4948337`.

[130] Takuma Hori, Junichiro Shiomi, and Chris Dames. Effective phonon mean free path in polycrystalline nanostructures. *Applied Physics Letters*, 106(17):171901, 2015. doi: 10.1063/1.4918703. URL `https://doi.org/10.1063/1.4918703`.

[131] Kouhei Takahashi, Masaki Fujikane, Yuxuan Liao, Makoto Kashiwagi, Takashi Kawasaki, Naoki Tambo, Shenghong Ju, Yasuyuki Naito, and Junichiro Shiomi. Elastic inhomogeneity and anomalous thermal transport in ultrafine si phononic crystals. *Nano Energy*, 71:104581, 2020. ISSN 2211-2855. doi: https://doi.org/10.1016/j.nanoen.2020.104581. URL `http://www.sciencedirect.com/science/article/pii/S2211285520301397`.

[132] Ravi Prasher. Transverse thermal conductivity of porous materials made from aligned nano- and microcylindrical pores. *Journal of Applied Physics*, 100(6):064302, 2006. doi: 10.1063/1.2337786. URL `https://doi.org/10.1063/1.2337786`.

[133] Congliang Huang, Xinpeng Zhao, Keith Regner, and Ronggui Yang. Thermal conductivity model for nanoporous thin films. *Physica E: Low-dimensional Systems and Nanostructures*, 97:277 – 281, 2018. ISSN 1386-9477. doi: https://doi.org/10.1016/j.physe.2017.11.014. URL `http://www.sciencedirect.com/science/article/pii/S1386947717316260`.

[134] C. Massobrio and G. Ciccotti. Lennard-jones triple-point conductivity via weak external fields. *Phys. Rev. A*, 30:3191–3197, Dec 1984. doi: 10.1103/PhysRevA.30.3191. URL `https://link.aps.org/doi/10.1103/PhysRevA.30.3191`.

[135] William Evans, Jacob Fish, and Pawel Keblinski. Thermal conductivity of ordered molecular water. *The Journal of Chemical Physics*, 126(15):154504, 2007. doi: 10.1063/1.2723071. URL `https://doi.org/10.1063/1.2723071`.

[136] Florian Müller-Plathe. A simple nonequilibrium molecular dynamics method for calculating the thermal conductivity. *The Journal of Chemical Physics*, 106(14):6082–6085, 1997. doi: 10.1063/1.473271. URL `https://doi.org/10.1063/1.473271`.

[137] E. Lampin, P. L. Palla, P.-A. Francioso, and F. Cleri. Thermal conductivity from approach-to-equilibrium molecular dynamics. *Journal of Applied Physics*, 114(3):033525, 2013. URL `http://scitation.aip.org/content/aip/journal/jap/114/3/10.1063/1.4815945`.

[138] Claudio Melis, Riccardo Dettori, Simon Vandermeulen, and Luciano Colombo. Calculating thermal conductivity in a transient conduction regime: theory and implementation. *Eur. Phys. J. B*, 87(4):96, 2014. doi: 10.1140/epjb/e2014-50119-0. URL `http://dx.doi.org/10.1140/epjb/e2014-50119-0`.

[139] Florian Müller-Plathe. A simple nonequilibrium molecular dynamics method for calculating the thermal conductivity. *The Journal of Chemical Physics*, 106(14):6082–6085, 1997. doi: http://dx.doi.org/10.1063/1.473271. URL `http://scitation.aip.org/content/aip/journal/jcp/106/14/10.1063/1.473271`.

[140] Stephen Stackhouse, Lars Stixrude, and Bijaya B. Karki. Thermal conductivity of periclase (mgo) from first principles. *Phys. Rev. Lett.*, 104:208501, May 2010. doi: 10.1103/PhysRevLett.104.208501. URL `http://link.aps.org/doi/10.1103/PhysRevLett.104.208501`.

[141] Claudio Melis and Luciano Colombo. Lattice thermal conductivity of $si_{1-x}ge_x$ nanocomposites. *Phys. Rev. Lett.*, 112:065901, Feb 2014. doi: 10.1103/PhysRevLett.112.065901. URL `http://link.aps.org/doi/10.1103/PhysRevLett.112.065901`.

[142] Giuliana Barbarino, Claudio Melis, and Luciano Colombo. Effect of hydrogenation on graphene thermal transport. *Carbon*, 80:167 – 173, 2014. ISSN 0008-6223. doi: http://dx.doi.org/10.1016/j.carbon.2014.08.052. URL `http://www.sciencedirect.com/science/article/pii/S0008622314007921`.

[143] Konstanze R. Hahn, Claudio Melis, and Luciano Colombo. Thermal transport in nanocrystalline graphene investigated by approach-to-equilibrium molecular dynamics simulations. *Carbon*, 96:429 – 438, 2016. ISSN 0008-6223. doi: http://dx.doi.org/10.1016/j.carbon.2015.09.070. URL `http://www.sciencedirect.com/science/article/pii/S0008622315302888`.

[144] Giuliana Barbarino, Claudio Melis, and Luciano Colombo. Intrinsic thermal conductivity in monolayer graphene is ultimately upper limited: A direct estimation by atomistic simulations. *Phys. Rev. B*, 91:035416, Jan 2015. doi: 10.1103/PhysRevB.91.035416. URL `http://link.aps.org/doi/10.1103/PhysRevB.91.035416`.

[145] Xavier Cartoixà, Riccardo Dettori, Claudio Melis, Luciano Colombo, and Riccardo Rurali. Thermal transport in porous si nanowires from approach-to-equilibrium molecular dynamics calculations. *Applied Physics Letters*, 109(1):013107, 2016. URL `http://scitation.aip.org/content/aip/journal/apl/109/1/10.1063/1.4955038`.

[146] Chaofeng Hou, Ji Xu, Wei Ge, and Jinghai Li. Molecular dynamics simulation overcoming the finite size effects of thermal conductivity of bulk silicon and silicon nanowires.

Modelling and Simulation in Materials Science and Engineering, 24(4):045005, 2016. URL http://stacks.iop.org/0965-0393/24/i=4/a=045005.

[147] Patrick K. Schelling, Simon R. Phillpot, and Pawel Keblinski. Comparison of atomic-level simulation methods for computing thermal conductivity. *Phys. Rev. B*, 65:144306, Apr 2002. doi: 10.1103/PhysRevB.65.144306. URL https://link.aps.org/doi/10.1103/PhysRevB.65.144306.

[148] Hayat Zaoui, Pier Luca Palla, Fabrizio Cleri, and Evelyne Lampin. Length dependence of thermal conductivity by approach-to-equilibrium molecular dynamics. *Phys. Rev. B*, 94:054304, Aug 2016. doi: 10.1103/PhysRevB.94.054304. URL https://link.aps.org/doi/10.1103/PhysRevB.94.054304.

[149] Taku Ohara. Intermolecular energy transfer in liquid water and its contribution to heat conduction: A molecular dynamics study. *The Journal of Chemical Physics*, 111(14): 6492–6500, 1999. doi: 10.1063/1.480025. URL https://doi.org/10.1063/1.480025.

[150] In-Chul Yeh and Gerhard Hummer. System-size dependence of diffusion coefficients and viscosities from molecular dynamics simulations with periodic boundary conditions. *The Journal of Physical Chemistry B*, 108(40):15873–15879, 2004. doi: 10.1021/jp0477147. URL https://doi.org/10.1021/jp0477147.

[151] F. Gygi. Architecture of qbox: A scalable first-principles molecular dynamics code. *IBM Journal of Research and Development*, 52(1.2):137–144, Jan 2008. ISSN 0018-8646. doi: 10.1147/rd.521.0137.

[152] John P. Perdew, Kieron Burke, and Matthias Ernzerhof. Generalized gradient approximation made simple. *Phys. Rev. Lett.*, 77: 3865–3868, Oct 1996. doi: 10.1103/PhysRevLett.77.3865. URL https://link.aps.org/doi/10.1103/PhysRevLett.77.3865.

[153] Viktor Rozsa, Ding Pan, Federico Giberti, and Giulia Galli. Ab initio spectroscopy and ionic conductivity of water under earth mantle conditions. *Proceedings of the National Academy of Sciences*, 115(27):6952–6957, 2018. ISSN 0027-8424. doi: 10.1073/pnas.1800123115. URL https://www.pnas.org/content/115/27/6952.

[154] R. C. Reid, J. M. Prausnitz, and B. E. Poling. *The properties of gases and liquids*. McGraw Hill Book Co.,New York, NY, United States, 1987. URL https://www.osti.gov/servlets/purl/6504847.

[155] Zachary M. Geballe and Viktor V. Struzhkin. Ac calorimetry of h2o at pressures up to 9 gpa in diamond anvil cells. *Journal of Applied Physics*, 121(24):245901, 2017. doi: 10.1063/1.4989849. URL https://doi.org/10.1063/1.4989849.

[156] Miguel A. González and José L. F. Abascal. A flexible model for water based on tip4p/2005. *The Journal of Chemical Physics*, 135(22):224516, 2011. doi: 10.1063/1.3663219. URL https://doi.org/10.1063/1.3663219.

[157] Jorge López-Lemus, Gustavo A. Chapela, and José Alejandre. Effect of flexibility on surface tension and coexisting densities of water. *The Journal of Chemical Physics*, 128(17):174703, 2008. doi: 10.1063/1.2907845. URL https://doi.org/10.1063/1.2907845.

[158] Tesfaye M. Yigzawe and Richard J. Sadus. Thermodynamic properties of liquid water from a polarizable intermolecular potential. *The Journal of Chemical Physics*, 138(4): 044503, 2013. doi: 10.1063/1.4779295. URL https://doi.org/10.1063/1.4779295.

[159] Bin Chen, Wen-Pin Hsieh, David G. Cahill, Dallas R. Trinkle, and Jie Li. Thermal conductivity of compressed h2o to 22 gpa: A test of the leibfried-schlömann equation. *Phys. Rev. B*, 83:132301, Apr 2011. doi: 10.1103/PhysRevB.83.132301. URL https://link.aps.org/doi/10.1103/PhysRevB.83.132301.

[160] Berendsen H. J. C., Postma J. P. M., W. F. van Gunsteren, and J Hermans. Interaction models for water in relation to protein hydration. In B. Pullman and Dordrecht Reidel, editors, *Intermolecular Forces*. D. Reidel Publishing Company, 1981.

[161] Yijin Mao and Yuwen Zhang. Thermal conductivity, shear viscosity and specific heat of rigid water models. *Chemical Physics Letters*, 542:37 – 41, 2012. ISSN 0009-2614. doi: https://doi.org/10.1016/j.cplett.2012.05.044. URL http://www.sciencedirect.com/science/article/pii/S0009261412006367.

[162] Timothy W. Sirk, Stan Moore, and Eugene F. Brown. Characteristics of thermal conductivity in classical water models. *The Journal of Chemical Physics*, 138(6):064505, 2013. doi: 10.1063/1.4789961. URL https://doi.org/10.1063/1.4789961.

[163] H. J. C. Berendsen, J. R. Grigera, and T. P. Straatsma. The missing term in effective pair potentials. *The Journal of Physical Chemistry*, 91(24): 6269–6271, Nov 1987. ISSN 0022-3654. doi: 10.1021/j100308a038. URL https://doi.org/10.1021/j100308a038.

[164] José Alejandre, Gustavo A. Chapela, Fernando Bresme, and Jean-Pierre Hansen. The short range anion-h interaction is the driving force for crystal formation of ions in water. *The Journal of Chemical Physics*, 130(17):174505, 2009. doi: 10.1063/1.3124184. URL https://doi.org/10.1063/1.3124184.

[165] Yujie Wu, Harald L. Tepper, and Gregory A. Voth. Flexible simple point-charge water model with improved liquid-state properties. *The Journal of Chemical Physics*, 124(2): 024503, 2006. doi: 10.1063/1.2136877. URL https://doi.org/10.1063/1.2136877.

[166] Liem X. Dang and B. Montgomery. Pettitt. Simple intramolecular model potentials for water. *The Journal of Physical Chemistry*, 91(12):3349–3354, 1987. doi: 10.1021/j100296a048. URL https://doi.org/10.1021/j100296a048.

[167] J. L. F. Abascal and C. Vega. A general purpose model for the condensed phases of water: Tip4p/2005. *The Journal of Chemical Physics*, 123(23):234505, 2005. doi: 10.1063/1.2121687. URL https://doi.org/10.1063/1.2121687.

[168] Michael W. Mahoney and William L. Jorgensen. A five-site model for liquid water and the reproduction of the density anomaly by rigid, nonpolarizable potential functions. *The Journal of Chemical Physics*, 112(20):8910–8922, 2000. doi: 10.1063/1.481505. URL https://doi.org/10.1063/1.481505.

[169] Niall J. English and John S. Tse. Thermal conductivity of supercooled water: An equilibrium molecular dynamics exploration. *The Journal of Physical Chemistry Letters*, 5(21):3819–3824, 2014. doi: 10.1021/jz5016179. URL https://doi.org/10.1021/jz5016179. PMID: 26278754.

[170] Steven W. Rick. A reoptimization of the five-site water potential (tip5p) for use with ewald sums. *The Journal of Chemical Physics*, 120(13):6085–6093, 2004. doi: 10.1063/1.1652434. URL https://doi.org/10.1063/1.1652434.

[171] Eiji Tsuchida. Thermal conductivity of liquid water from reverse nonequilibrium ab initio molecular dynamics. *Journal of the Physical Society of Japan*, 87(2):025001, 2018. doi: 10.7566/JPSJ.87.025001. URL https://doi.org/10.7566/JPSJ.87.025001.

[172] R. W. Powell, C. Y. Ho, and P. E. Liley. Thermal conductivity of selected materials. *NIST reference data*, 1966. URL https://nvlpubs.nist.gov/nistpubs/Legacy/NSRDS/nbsnsrds8.pdf. page 130.

[173] Maria L. V. Ramires, Carlos A. Nieto de Castro, Yuchi Nagasaka, Akira Nagashima, Marc J. Assael, and William A. Wakeham. Standard reference data for the thermal conductivity of water. *Journal of Physical and Chemical Reference Data*, 24(3):1377–1381, 1995. doi: 10.1063/1.555963. URL https://doi.org/10.1063/1.555963.

[174] Linfeng Zhang, Jiequn Han, Han Wang, Roberto Car, and Weinan E. Deep potential molecular dynamics: A scalable model with the accuracy of quantum mechanics. *Phys. Rev. Lett.*, 120:143001, Apr 2018. doi: 10.1103/PhysRevLett.120.143001. URL https://link.aps.org/doi/10.1103/PhysRevLett.120.143001.